Nonlinear optics with ultrashort mid-infrared laser pulses

Gonçalo Alexandre Luís Vaz

Thesis to obtain the Master of Science Degree in

Engineering Physics

Supervisors: Prof. Hugo Filipe de Almeida Pires
Prof. Gonçalo Nuno Marmelo Foito Figueira

Examination Committee

Chairperson: Prof. João Alberto dos Santos Mendanha Dias
Supervisor: Prof. Gonçalo Nuno Marmelo Foito Figueira
Members of the Committee: Prof. Ana Cristina Gomes Silva
Dr. Gareth Oisin Williams

December 2021

Declaration:

I declare that this document is an original work of my own authorship and that it fulfills all the requirements of the Code of Conduct and Good Practices of the Universidade de Lisboa.

This work was created using LaTeX typesetting language
in the Overleaf environment (www.overleaf.com).

Acknowledgments

I would like to thank the many people who have contributed to the work described in this thesis. First, my dissertation supervisors, Prof. Gonçalo Figueira and Prof. Hugo Pires for their guidance and continuous support not only during this thesis but also the previous courses of my Master's degree. Second, my seniors, Joana Alves and Victor Hariton for spending some of their time showing me the ropes and for all of their insight and support. Third, to Gareth Williams and Mukhtar Hussain for their invaluable insight on high-harmonic generation. Fourth, to the Instituto de Plasmas e Fusão Nuclear (IPFN)/Group of Lasers and Plasmas (GoLP) group that made this thesis possible.

I would also like to thank all of my friends, colleagues, and teachers, that I met over the years, that in some way or another helped me grow, not only in terms of knowledge but also as a person and an individual.

Finally, my family deserves a special thanks. My parents and brother, for their unconditional support. My maternal grandparents, uncle, and cousins, who took me in when I started college. And my paternal grandparents, who are no longer with us.

Resumo

Nos últimos anos, temos assistido ao nascimento da primeira geração de fontes laser de alta energia e eficiência no infravermelho médio (MIR), região espectral dos 2 – 12 µm. Esta tese reporta o primeiro conjunto de experiências com o novo sistema laser de MIR localizado no Laboratório de Lasers Intensos (L2I) no Instituto Superior Técnico de Lisboa (IST), sob a alçada do Grupo de Lasers e Plasmas (GoLP), afiliado ao Instituto de Plasmas e Fusão Nuclear (IPFN). Este é o primeiro laser ultracurto e de alta energia no MIR em Portugal,e um dos poucos em existência nos 3 µm.

O sistema é baseado em Amplificação Óptica Paramétrica de Pulsos Chirpados (OPCPA) usando um laser de bombeamento de 1.03 µm que gera impulsos com uma taxa de repetição de 100 kHz, cada um com uma duração de 1 ps. O resultado final são pulsos de 40 fs emitidos a 100 kHz nos 3 µm. Estes pulsos são emitidos com uma potência média de 6.5 W, energia de 65 µJ, uma intensidade focal de 2×10^{15} W/cm^2, potência de pico de 1.7 GW, e um rácio de Strehl > 0.7. Infelizmente, devido à actual situação pandémica, as condições de funcionamento foram sub-óptimas durante as nossas experiências, estando o sistema a ser realinhado pelos fornecedores.

As nossas experiências consistiram em alargamento espectral não linear a 1.03 µm, Geração de Supercontínuo (SCG) a 3 µm, e geração de harmónicos a 3 µm. Aqui são descritas as montagens experimentais juntamente com os dados experimentais das interacções laser-sólido. Finalmente, os resultados são comparados com dados publicados com a identificação dos parâmetros para interacções de óptica não linear de alta eficiência.

Palavras chave

Alargamento Espectral; Geração de harmónicos; Geração de altos harmónicos; Infravermelho médio; Óptica não linear; Supercontínuo

Abstract

During the last few years, we have witnessed the birth of the first generation of high-energy and high-efficiency laser sources in the Mid-Infrared (MIR) spectral region, $2-12$ µm. This thesis reports the first set of experiments with the new MIR laser system at the Laboratory of Intense Lasers (L2I) in Instituto Superior Técnico de Lisboa (IST), under the management of the Group of Lasers and Plasmas (GoLP), affiliated with the Instituto de Plasmas e Fusão Nuclear (IPFN). This is the very first ultrashort, high-energy MIR laser system in Portugal, and one of the few in existence at 3 µm.

The system is based on Optical Parametric Chirped-Pulse Amplification (OPCPA) using a laser pump of 1.03 µm generating pulses at a repetition rate of 100 kHz, each with a duration of 1 ps. The final output are 40 fs pulses delivered at 100 kHz in the 3 µm. These pulses are emitted with: an average power of 6.5 W, energy of 65 µJ, focused intensity of 2×10^{15} W/cm^2, 1.7 GW of peak power, and a Strehl ratio > 0.7. Unfortunately, due to the current pandemic, the condition of the system was sub-optimal during our experiments, and is currently being realigned by the suppliers.

Our experiments consisted of nonlinear spectral broadening at 1.03 µm, Supercontinuum Generation (SCG) at 3 µm, and harmonic-generation at 3 µm. Here we describe the experimental setups together with data from the laser-solid interactions. Finally, the results are compared with published data with identification of the critical parameters for high efficiency nonlinear optical interactions.

Keywords

Harmonic generation; High-Harmonic Generation; Mid-infrared; Nonlinear optics; Spectral broadening; Supercontinuum

Contents

1 Introduction 1

1.1 Mid-Infrared laser systems . . . 4
1.2 Supercontinuum Generation . . . 5
1.3 High-Harmonic Generation . . . 6

2 Laser System 7

2.1 Pumping . . . 10
2.2 Optical Parametric Chirped-Pulse Amplification . . . 10

3 Nonlinear spectral broadening 13

3.1 Physical principles in solid materials . . . 15
3.1.1 Self-Phase Modulation . . . 15
3.1.2 Self-steepening . . . 16
3.1.3 Self-focusing, filamentation and conical emission . . . 18
3.1.4 Effects of dispersion on Supercontinuum Generation . . . 19
3.1.5 Stimulated Raman Scattering . . . 19
3.2 Experimental Work . . . 21
3.2.1 Setup . . . 21
3.2.2 Methods and Results . . . 23
3.2.2.1 Supercontinuum Generation at 3 μm . . . 23
3.2.2.2 Spectral broadening at 1.03 μm . . . 24
3.3 Numerical simulation of spectral broadening . . . 28
3.3.1 Theoretical approach . . . 28
3.3.2 Numerical values and results . . . 30
3.3.2.1 Numerical values . . . 30
3.3.2.2 Results . . . 32

4 High-Harmonic Generation 37

4.1 Physical Principles . . . 39
4.1.1 Perturbative Harmonic generation . . . 39

4.1.2 High-Harmonic Generation in gases (atomic) . . . 41
4.1.3 High-Harmonic Generation in solids . . . 44
4.2 Experimental Work . . . 46
4.2.1 Setup . . . 47
4.2.2 Methods and Results . . . 48
4.2.2.1 Calcium fluoride samples . . . 49
4.2.2.2 Fused Silica sample . . . 53
4.2.2.3 Lithium fluoride sample . . . 54
4.2.2.4 Sapphire samples . . . 55
4.2.2.5 Fourier analysis . . . 57
4.2.2.6 Final remarks . . . 60
4.3 Simulation in literature . . . 63

5 Conclusion **65**
5.1 Review . . . 67
5.1.1 Chapter 3 . . . 67
5.1.2 Chapter 4 . . . 67
5.2 Future work . . . 68
5.2.1 Spectral broadening . . . 68
5.2.2 Harmonic Generation . . . 68

Bibliography **69**

A Full spectra **77**

B Simulations and calculations with pyNLO **81**

List of Figures

1.1 Laser systems (~ 3 μm, $<$ mJ) around the world. 5

2.1 MIR laser system installed at L2I. The white device on the left corresponds to the 1.03 μm pump. while the blue device at the right performs the OPCPA to generate the 3 μm laser pulses. 9

2.2 Schematics of OPA or DFG. On the left there is a macroscopic view in which the pump (blue; ω_p) and the signal (green; ω_s) interact inside a nonlinear media, resulting in energy loss by the pump, energy gain by the signal, and the emission of a third frequency commonly known as idler (red; ω_i). On the right, the band structure of this process where a pump photon excites the material to a virtual level, which leads to the emission of a signal photon by stimulated emission followed by emission of one idler photon by spontaneous emission. 11

2.3 Schematic of the 3 μm laser system. 12

3.1 Instantaneous frequency of an initially unchirped pulse which has experienced self-phase modulation. The central part of the pulse exhibits an up-chirp. 17

3.2 Simulation of the formation of a light bullet and consequent self-steepening during propagation in fused silica. z is the propagation distance. 17

3.3 Plasma fluorescence traces in a YAG crystal induced by self-focusing of 100 fs, 800 nm input pulses with energies of **(a)** 310 nJ, **(b)** 560 nJ, that induce a single self-focusing event and refocusing of the filament, respectively. **(c)** and **(d)** show the corresponding far-field patterns of supercontinuum emission. Note the conical emission pattern surrounding the white-light (supercontinuum). 18

3.4 Top row: numerically simulated temporal dynamics of 100 fs laser pulses propagating in sapphire crystal with the input wavelengths of **(a)** 800 nm, **(b)** 1.3 μm, **(c)** 2.0 μm, representing the filamentation regimes of normal, zero and anomalous Group Velocity Dispersion (GVD), respectively. Bottom row shows the corresponding spectral dynamics. Notice, how the spectral broadening in the regimes of normal and zero GVD is associated with the pulse splitting, and the spectral broadening in the regime of anomalous GVD is associated with pulse self-compression. 20

3.5 Schematic of SRS. Left: macroscopic view in which the pump (blue; ω_p) and the signal (green; ω_s) interact inside a nonlinear medium where there is an excitation of vibrational modes. Right: band structure of this process, where a pump photon excites the material to a virtual level, which leads to the emission of a signal photon by stimulated emission, while the excess energy is transferred to a vibrational mode of the medium, (black dashed; $\hbar\omega_r$). The medium has a gain curve with a certain bandwidth, (red; $\Delta\hbar\omega$), which goes to zero as $\hbar\omega_r \approx 0$. 21

3.6 Experimental setup for the acquisition of SCG at 3 μm. Top: setup with 10% of the output power using a wedge. Bottom: setup with the full power. 22

3.7 Experimental setup for the acquisition of spectral broadening at 1.03 μm. 23

3.8 Group Velocity Dispersion for the four samples used in the spectral broadening at 1.03 μm. Calculated with the code in listing B.2. 24

3.9 Supercontinuum Generation at 3 μm. 25

3.10 Conical emission with a 3 μm laser. In the left with a 5 mm fused silica sample and in the right with a 4mm YAG sample. Note the white-light at the center of the beam (supercontinuum). 25

3.11 Interpolation of the multiplied data from all seven filters. In the inset the region of interest for Fig.3.12. 26

3.12 Spectral broadening at 1.03 μm. The captions are the percentage of the full power (82 W) sent to the sample. The insets depict the variation of FWHM with the power. 27

3.13 Reconstruction of the beam radius variation. On the right, we have a zoom in to the experimental data, together with the fit (dashed lines) to equation 3.15 and the resulting parameters w_0 and z_{ref}. These parameters were then used as an input to a propagation software to make the backward propagation of the beam through the lenses until the output of the *AMPHOS* laser, z = 0, which correspond to the continuous lines on the left side. The dashed lines in the left figure represent the position of the two lenses of focal length: f = 350 mm (black) and f = –200mm (red). 31

3.14 Variation of the beam radius until the sample, obtained with a propagation software. Here the values of w_0 and z_{ref} correspond to the laser's propagation parameters, obtained from the study presented in Fig.3.13. The dashed black line corresponds to the position of the f = 400 mm lens, while the red one marks the position of the focus, 400 mm away from the lens. The upper axes depicts the distance to the lens. 31

3.15 Simulation of spectral broadening at 1.03μm. Each experimental spectrum corresponds to the highest energy for each sub-figure in Fig.3.12, with the exception of Fig.3.12c where we took the 20% spectrum (before damage). On the left is the comparison of the numerical input and output pulse together with the experimental data. On the right is the numerical spectral variation with propagation. The curves were truncated at –20 dB. . . . 34

4.1 Schematic of SHG. Left: macroscopic view in which the input beam (red; ω) interact with a nonlinear media, resulting in the formation of a new beam with twice the frequency of the input known as the Second Harmonic (blue; 2ω). Right: band structure of this process where two input photons excite in quick succession the material to a virtual level which then leads to the emission of a single Second Harmonic photon by spontaneous emission. 40

4.2 Three-step recolisional model. **(a)** A gas atom is modeled as a single electron in the ground state of a potential well with ionization potential I_p. **(b)** An applied optical field E(t) from an exciting laser alters the potential well and causes the electron to tunnel into free space at time t_i. **(c)** The free electron is accelerated in the +x direction by the negative optical field but reverses direction when the optical field becomes positive, returning back to the ionized atom with increased kinetic energy E_k at time t_r. **(d)** The electron recombines with the ion and radiates photons of energy $I_p + E_k$ that takes the form of a chirped pulse of radiation with sub-femtosecond structure. 42

4.3 Comparison between **(a)** emission of visible light by Second Harmonic Generation (SHG) and **(b)** emission of extreme Ultraviolet (UV) by High-Harmonic Generation (HHG). In **(b)** note the formation of train of sub-femtosecond pulses, one for each half-cycle of the exciting Infrared (IR) field, together with the spectrum consisting of a frequency comb with a tooth spacing $2\omega_0$. 42

4.4 Relative intensity of the harmonics generated in Xe gas. 43

4.5 **a**- The driven electron could scatter from the periodic Coulomb potential termed as Bloch oscillations, recombine with the associated hole (ion) and recollide with the first- and second-nearest holes (ions); **b**- The momentum-space version of a, showing intraband Bloch Oscillations in the conduction band and interband coupling between the valence and conduction band, both emitting high-frequency radiation in the forward direction; **c**- Schematic diagram of the three-step recollision model comprising tunnel ionization, free acceleration and recombination; **d**- The momentum-space version of c, where the electron tunnels from the bound state to the continuum state, accelerates in the parabolic continuum band and then recombines to the bound state (parent ion) emitting high-frequency radiation. 45

4.6 Experimental setup for the acquisition of harmonics. Top: setup with 10% of the output power using a wedge. Bottom: setup with the full power. 47

4.7 Polar plots for the 1 mm CaF_2 sample placed at focus. The radius corresponds to the normalized area beneath the curve. In red calculated by a Gaussian fit and in blue by a numerical integration within $1/e^2$ of the maximum number of counts. **W** stands for the low-power using a wedge setup while **M** stands for the high-power setup using a mirror. . 49

4.8 Smoothed spectra of all harmonics obtained with a CaF_2 sample of 1 mm. Each spectrum corresponds to the angle with the highest count rate and are centered around the fundamental. On the left all spectra were normalized, while on the right we present the count rate of each spectrum. 50

4.9 Polar plots for the 3 mm CaF_2 sample. The radius corresponds to the normalized area beneath the curve. In red, green and magenta calculated by a Gaussian fit and in blue by a numerical integration within $1/e^2$ of the maximum number of counts. **W** stands for the low-power using a wedge setup while **M** stands for the high-power setup using a mirror. . 52

4.10 Smoothed spectra of all harmonics obtained with a CaF_2 sample of 3 mm. Each spectrum corresponds to the angle with the highest count rate and are centered around the fundamental. On the left all spectra were normalized, while on the right we present the count rate of each spectrum. 52

4.11 Polar plots for the 5 mm fused silica sample. The radius corresponds to the normalized area beneath the curve. In red calculated by a Gaussian fit and in blue by a numerical integration within $1/e^2$ of the maximum number of counts. **W** stands for the low-power using a wedge setup while **M** stands for the high-power setup using a mirror. 53

4.12 Smoothed spectra of all harmonics obtained with a fused silica sample of 5 mm. Each spectrum corresponds to the angle with the highest count rate and are centered around the fundamental. On the left all spectra were normalized, while on the right we present the count rate of each spectrum. 53

4.13 Polar plots for the 3 mm LiF sample. The radius corresponds to the normalized area beneath the curve. In red calculated by a Gaussian fit and in blue by a numerical integration within 1/e^2 of the maximum number of counts. 54

4.14 Smoothed spectra of all harmonics obtained with a LiF sample of 3 mm. Each spectrum corresponds to the angle with the highest count rate and are centered around the fundamental. On the left all spectra were normalized, while on the right we present the count rate of each spectrum. 55

4.15 Polar plots for the 1 mm sapphire sample. The radius corresponds to the normalized area beneath the curve. In red calculated by a Gaussian fit and in blue by a numerical integration within 1/e^2 of the maximum number of counts. **W** stands for the low-power using a wedge setup while **M** stands for the high-power setup using a mirror. 56

4.16 Smoothed spectra of all harmonics obtained with a sapphire sample of 1 mm. Each spectrum corresponds to the angle with the highest count rate and are centered around the fundamental. On the left all spectra were normalized, while on the right we present the count rate of each spectrum. 56

4.17 Polar plots for the 2 mm sapphire sample. The radius corresponds to the normalized area beneath the curve. In red calculated by a Gaussian fit and in blue by a numerical integration within 1/e^2 of the maximum number of counts. All this data was taken in the low-power setup with the wedge. 57

4.18 Smoothed spectra of all harmonics obtained with a sapphire sample of 2 mm. Each spectrum corresponds to the angle with the highest count rate and are centered around the fundamental. On the left all spectra were normalized, while on the right we present the count rate of each spectrum. 57

4.19 Absolute value of the IFT for the THG spectra, in the insets the supposed FT. 59

4.20 On the left is the interpolation of the transmission data of the filter in the region of interest for the calibration. On the right four Supercontinuum Generation (SCG) spectra obtained in different positions of the fiber, after the correction of transmission and division by the acquisition time. 61

4.21 Final supercontinuum spectrum for integration and calibration of the harmonic's power. . . 61

A.1 Spectral broadening at 1.03 μm. The captions are the percentage of the full power (82 W) sent to the sample. The insets depict the variation of Full width at half maximum (FWHM) with the power. 78
A.2 Spectra of all harmonics obtained with a CaF_2 sample of 1 mm. Each spectrum corresponds to the angle with the highest count rate and are centered around the fundamental. On the left all spectra were normalized, while on the right we present the count rate of each spectrum. 79
A.3 Spectra of all harmonics obtained with a CaF_2 sample of 3 mm. Each spectrum corresponds to the angle with the highest count rate and are centered around the fundamental. On the left all spectra were normalized, while on the right we present the count rate of each spectrum. 79
A.4 Spectra of all harmonics obtained with a fused silica sample of 5 mm. Each spectrum corresponds to the angle with the highest count rate and are centered around the fundamental. On the left all spectra were normalized, while on the right we present the count rate of each spectrum. 79
A.5 Spectra of all harmonics obtained with a LiF sample of 3 mm. Each spectrum corresponds to the angle with the highest count rate and are centered around the fundamental. On the left all spectra were normalized, while on the right we present the count rate of each spectrum. 80
A.6 Spectra of all harmonics obtained with a sapphire sample of 1 mm. Each spectrum corresponds to the angle with the highest count rate and are centered around the fundamental. On the left all spectra were normalized, while on the right we present the count rate of each spectrum. 80
A.7 Spectra of all harmonics obtained with a sapphire sample of 2 mm. Each spectrum corresponds to the angle with the highest count rate and are centered around the fundamental. On the left all spectra were normalized, while on the right we present the count rate of each spectrum. 80

List of Tables

2.1 Specifications of the two laser systems used in this thesis. 9

3.1 Numerical values for simulation. 32

4.1 Calculated values for the Fourier analysis of the THG spectra. 58
4.2 Approximated power, photon rate and efficiency of each harmonic. 62

Listings

B.1 Code for the calculation of GVD. 81
B.2 Code for the simulation with pyNLO. 83
B.3 Contents of Crystals.py. 87

Acronyms

BO	Bloch Oscillations
CEP	Carrier-Envelope Phase
DFG	Difference-Frequency Generation
FROG	Frequency-Resolved Optical Gating
FT	Fourier Transform
FWM	Four-Wave Mixing
FWHM	Full width at half maximum
GDD	Group delay dispersion
GNLSE	Generalized Nonlinear Schrödinger Equation
GoLP	Group of Lasers and Plasmas
GVD	Group Velocity Dispersion
HHG	High-Harmonic Generation
IFT	Inverse Fourier Transform
IPFN	Instituto de Plasmas e Fusão Nuclear
IR	Infrared
IST	Instituto Superior Técnico de Lisboa
L2I	Laboratory of Intense Lasers
MIR	Mid-Infrared
MPC	Multipass cell

NIR	Near-Infrared
OD	Optical density
ODR	Orthogonal distance regression
OPA	Optical Parametric Amplification
OPCPA	Optical Parametric Chirped-Pulse Amplification
SCG	Supercontinuum Generation
SHG	Second Harmonic Generation
SPM	Self-Phase Modulation
SRS	Stimulated Raman Scattering
THG	Third Harmonic Generation
UV	Ultraviolet
YAG	Yttrium aluminium garnet

1

Introduction

Contents

1.1 Mid-Infrared laser systems 4
1.2 Supercontinuum Generation 5
1.3 High-Harmonic Generation 6

In the past two decades, there has been a growing interest and investment in the study of ultrafast optics and ultrafast science in the Mid-Infrared (MIR), $2-12\ \mu m$ spectral region. This is largely due to the fact that the fundamental vibrational absorptions of most molecules reside within this range, leaving distinctive spectral fingerprints, which are of key importance for industrial, medical, and scientific applications. During the last few years, we have witnessed the birth of the first generation of high-energy and high-efficiency laser sources in the MIR region. The introduction of such sources opened the doors to a variety of new and exciting applications, in particular in the branch of ultrafast science. Some of the most notable applications of MIR ultrafast sources are succinctly introduced below [1].

- **Supercontinuum generation**, a process where an intense laser pulse propagates through a nonlinear medium leading to an ultrabroad, continuous output spectrum. Supercontinuum light sources are generally used for purposes where one requires light with a broad optical bandwidth and a high degree of spatial coherence so that the light can be well collimated and focused. For example, optical coherence tomography, fluorescence microscopy, flow cytometry, the characterization of optical devices, the generation of multiple carrier waves in optical fiber communications systems, and the measurement of the carrier-envelope offset frequency of frequency combs [2].

- **Frequency comb** consists of an optical spectrum composed of periodic lines. Frequency combs were first introduced in the 1990s and started to attract a lot of attention since the 2005 Nobel Prize in Physics [3]. MIR mode-locked laser sources are probably the most general, reliable, naturally low-noise, and compact choice for the generation of such spectra with applications such as high-resolution/sensitivity spectroscopy, optical clocks frequency metrology, optical sensing, distance measurements, laser noise characterization, telecommunications, and fundamental physics [2].

- **Spectroscopy** with ultrafast MIR pulses has been of key importance in the fields of molecular science and solid-state physics, due to its high sensitivity and resolution over a broad spectral domain. For example, it has allowed us to observe the structural dynamics of molecules, such as vibrational mode coupling, as well as charge transfer and free-carrier dynamics in semiconductors [4–7].

- **Material processing** based on ultrashort MIR laser pulses has become quite popular in recent years, in particular in materials like silicon and germanium that are opaque in the visible and near-infrared but transparent in the MIR. In theory, ultrashort MIR laser pulses could be applied in microfabrication to create complex three-dimensional optical circuits directly inside silicon, overcoming problems that current lithography cannot overcome; and could also be used to achieve kerfless processing of silicon replacing the current use of diamond saws to separate wafers from the silicon bulk. Another use, already demonstrated [8], is the cutting and welding of polymers with such ultrashort MIR laser pulses.

- **Laser surgery and biodiagnostics** have found a powerful weapon in ultrafast MIR laser pulses. Mainly due to the presence of the vibrational absorption band of water molecules within tissues in the 3 μm region, making it so that MIR radiation is absorbed in a few microns. In a minimally invasive surgical environment picosecond-level pulses are short enough to drive tissue ablation faster and with less damage to the surrounding tissue (< 10 μm) than the most common processes (scalpels, $>$ 400 μm, and conventional medical lasers, $>$ 800 μm) [9]. Additionally, it has been proven that the damage from these pulses heals much faster, and that the remaining scars are half the size and with less probability of infection than other conventional methods.

At the end of the year 2020, Instituto Superior Técnico de Lisboa (IST) acquired one of these new laser sources. This custom-made system is now installed in the Laboratory of Intense Lasers (L2I), a facility managed by the Group of Lasers and Plasmas (GoLP) at Instituto de Plasmas e Fusão Nuclear (IPFN) and is the first ultrashort, high-energy MIR laser system in Portugal. Not only that but this device has an output at 3 μm which, even within high-energy lasers working in the MIR, is extremely rare due to the innate inefficiency of the most gain materials at this wavelength. On top of being the first of its kind in the country, there are only a handful of similar laser systems in Europe.

The scope of this thesis is centered on exploring the capabilities of the new state-of-the-art MIR laser system installed at L2I, in particular its characterization and the development of the first series of experiments, and is divided in the following main components:

- Spectral broadening at 1.03 μm and Supercontinuum Generation (SCG) at 3 μm
- Harmonic generation at 3 μm

In Chapter 2 we briefly discuss the physical principles and specifications of the laser system used in the experiments. Chapter 3 is dedicated to spectral broadening, starting with a short theoretical overview, followed by the presentation of the experimental setup, results, and discussion for input pulses at 1.03 μm and 3 μm. This chapter ends with numerical simulations to support the results obtained at 1.03 μm. The generation of harmonics is then presented in Chapter 4 in a similar structure to Chapter 3, except for the simulations where we instead present a brief overview of some of the existing methodologies for the simulation of harmonic generation. Finally, Chapter 5 is dedicated to the conclusions, including a quick review of the main results of Chapters 3 and 4, finalizing with remarks on possible future works.

1.1 Mid-Infrared laser systems

The rapid advances in material research over the past decade have allowed the development of many new MIR gain materials with excellent optical and mechanical properties for the generation of ultrashort pulses, leading to the first generation of high-efficiency, low cost, compact MIR laser systems. However,

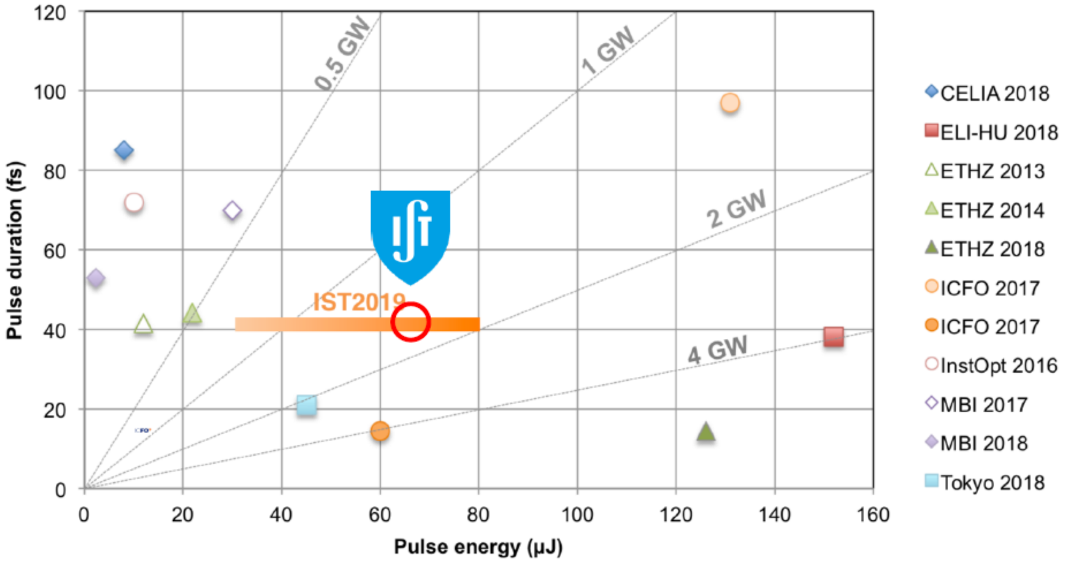

Figure 1.1: Laser systems (~ 3 µm, $<$ mJ) around the world.

the presence of the vibrational modes that we want to explore leads to great losses in most materials, significantly limiting the availability of gain media and saturable absorbers for the development of laser sources. For this reason, in the early 2000s, MIR laser sources were seldom and normally extremely complex, expensive, and inefficient [1].

Even within the MIR region, the wavelengths around 3 µm can be extremely elusive. In fact, just a few years ago there were no efficient high-energy laser sources at this wavelength. For example, quantum cascade lasers at room temperature only operated properly above 3.5 µm, conventional silica fiber lasers could only generate up to 2.5 µm and many alternatives had stability and optical damage problems [10]. Today, however, there are already some efficient laser sources that are now entering the market, but naturally, these systems are still a tiny share compared with, for example, the 2 µm lasers.

The new system at IST is precisely one of these extremely rare, state-of-the-art 3 µm laser systems. Figure 1.1 shows the pulse energy vs. pulse duration for comparable laser systems worldwide, highlighting the parameters of the IST system.

1.2 Supercontinuum Generation

SCG has been studied extensively during the last 50 years in a multitude of nonlinear media since it was first observed by Alfano *et al* [11] in 1970. In a pioneering experiment, 5 mJ picosecond pulses at 530 nm were propagated in BK7 glass, leading to an output spectrum covering the entire visible range from 400 to 700 nm. The nonlinear broadening was not a complete novelty at the time, however, what differentiated this experiment from previous works was the extent of the generated light spectrum, being 10 times greater than anything observed before. Curiously enough their work was dedicated to the first identification of nonresonant four-photon coupling, i.e., Four-Wave Mixing (FWM) so the term ”super-continuum” was only established in 1985 by Manassah *et al* [12].

In the following years, a variety of experiments were performed using different propagation media, mainly with nonlinear crystals and waveguides but also, on a smaller scale, air and noble gases. However, the input pulses were mainly in the visible or Near-Infrared (NIR). Only around the 2010s, we started to observe SCG based on MIR pulses, mainly due to the lack of efficient sources as mentioned.

1.3 High-Harmonic Generation

High-Harmonic Generation (HHG) in a gas medium is the oldest and most well-established way to generate high harmonics up to the extreme ultraviolet range. One of the earliest observations of HHG was made by Ferray *et al* [13] in 1988 by propagating 1064 nm, 30 fs laser pulses at 10 Hz into Ar, Kr, and Xe gases, achieving the 33rd, 29th and 21st harmonic, respectively. An interesting property of HHG in gases is that the maximum harmonic achievable grows, approximately, with the square of the input pulse wavelength [14], which implies that (at the same level of intensity) a lower frequency laser is actually capable of achieving much higher harmonics than a higher frequency one, and thus covering a greater spectrum. Possibly, the most famous experiments of gas-based HHG, where precisely this effect can be observed, was published in 2012 by Popmintchev *et al* [15], where they guided pulses centered at a wavelength of 3.9 μm into a waveguide filled with He and achieved harmonics greater than 5000, creating a supercontinuum spanning from the MIR to the soft X-rays.

Even though HHG has been observed for over 30 years, it took over two decades to achieve it in solid media, mainly because, in solids, the harmonics generated are strongly absorbed by the material itself and are more susceptible to self-action effects (both in time and space) [16]. The first successful result was reported by Ghimire *et al* [17] in 2011 where they obtained up to the 25th harmonic in a zinc oxide (ZnO) crystal injected with 3.25 μm laser pulses. The output takes the form of a train of short chirped pulses, one for each half-cycle of the input pulse. Each one of these short pulses has a spectrum in the form of a frequency comb in which the lines are separated by $2\omega_0$, where ω_0 is the input pulse central frequency. The main advantage of this technique is that we can generate extremely short pulses, down to attosecond duration, with an extremely large spectrum, in some cases thousands of harmonics, forming a supercontinuum. These pulses form the basis of attosecond science, in particular spectroscopy and imaging [18].

2

Laser System

Contents

2.1 Pumping 10

2.2 Optical Parametric Chirped-Pulse Amplification 10

In this chapter, we present briefly the characteristics of the laser system used in the experiments (Fig.2.1), together with a short explanation of the mechanisms behind their operation. Naturally, we cannot go into much detail to avoid revealing information under protection by the suppliers of the lasers, therefore we will only comment on what is available to the general public.

The system consists of a 1.03 µm pulsed laser source that can be used directly in the experiments or as a pump of a second device, which is based on Optical Parametric Chirped-Pulse Amplification (OPCPA), to generate 3 µm pulses. A collection of the main output parameters of the two systems is presented in Table 2.1.

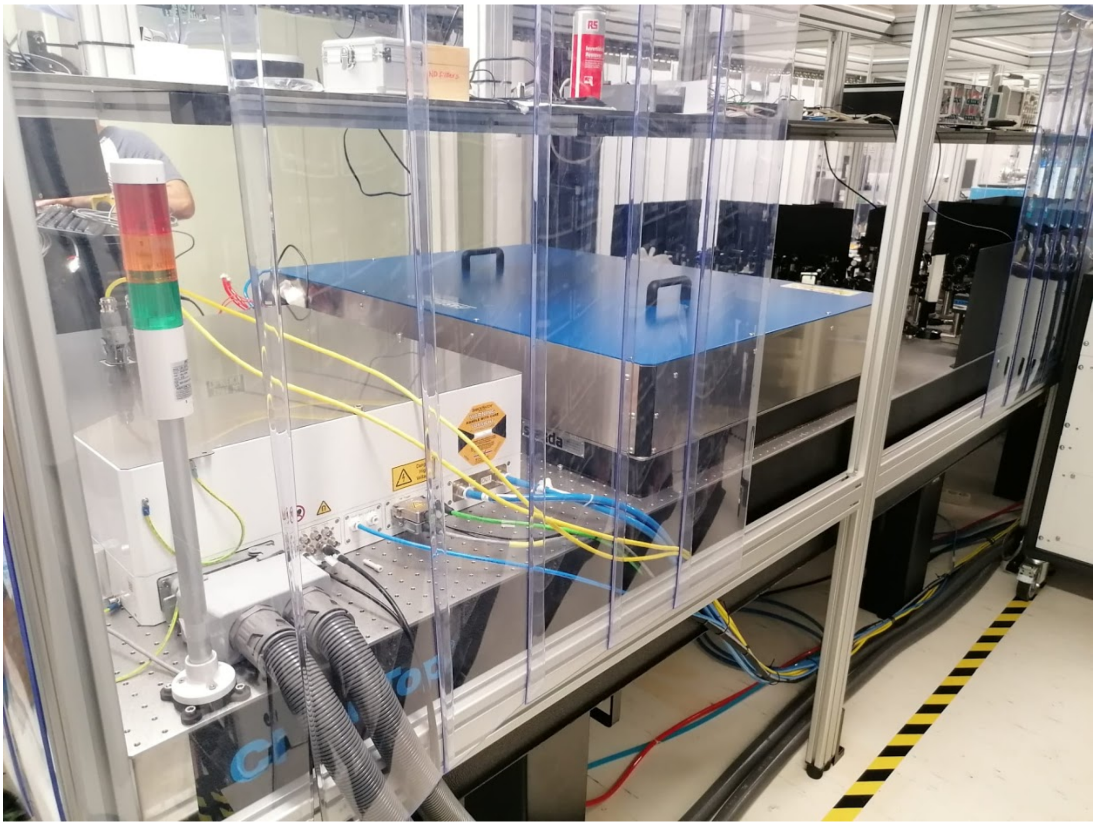

Figure 2.1: MIR laser system installed at L2I. The white device on the left corresponds to the 1.03 µm pump. while the blue device at the right performs the OPCPA to generate the 3 µm laser pulses.

Table 2.1: Specifications of the two laser systems used in this thesis.

System	Wavelength	Average Power	Repetition rate	Energy per pulse	Pulse duration
Pump by *AMPHOS*	1030 nm	100 W	100 kHz	1 mJ	1 ps
OPCPA by *FASTLITE*	3000 nm	6.5 W	100 kHz	65 µJ	40 fs

2.1 Pumping

The pump system is a *Amphos2000*, commercialized by *AMPHOS*, which is based on a diode-pump solid state Yb:YAG resonator coupled with InnoSlab amplification [19].

The system is specified to generate pulses with a length of 0.9 – 10 ps, a repetition rate of 100 kHz, and power up to 100 W. Unfortunately, due to the current pandemic of COVID-19, and consequent traveling restrictions, this system could not be fully installed and optimized, as this procedure must be performed by *AMPHOS* technical staff. Because of this, the max output power was reduced to about 82 W and the beam was slightly elliptical, with an ellipticity of ~ 0.8.

To perform OPCPA the pump is set to generate pulses with a repetition rate of 100 kHz and duration of 1 ps. The average power of the beam is then set to slightly above 75.5 W, ensuring that the OPCPA system is working in a saturation regime so that any fluctuation of the pump power does not affect the 3 μm output.

2.2 Optical Parametric Chirped-Pulse Amplification

The system for OPCPA is a custom made *Starzz* model created by *FASTLITE*, which is based in SCG followed by multiple stages of Optical Parametric Amplification (OPA), also known as Difference-Frequency Generation (DFG)[1]. Since SCG will be discussed in detail in Chapter 3 we will just review quickly the physical principles of the OPA and finish this chapter with a overview of *Starzz* system.

First, OPA is a phenomenon only observable in the nonlinear optics regime, which is many times referred to as DFG. As the name of the latter suggests this phenomenon allows to obtain a new frequency that is equal to the difference of the input frequencies. To achieve this we introduce two beams of different frequencies inside a nonlinear media, Fig.2.2. The one at a higher frequency, ω_p, is called a ”pump” while the lower frequency, ω_s, is called the ”signal”. Some of the photons from the pump will excite the material to a virtual level, which is not an energy eigenlevel of the free atom but rather represents the combined energy of one of the energy eigenstates of the atom and one or more photons of the radiation field. According to the uncertainty principle, a population can reside in a virtual level for a time interval of the order of $\hbar/\delta E$, where δE is the energy difference between the virtual level and the nearest real level [20]. This excitation will lead either to the spontaneous emission of a pump photon or to the stimulated emission of a signal photon due to the presence of the signal. In the case of stimulated emission the number of photons of frequency ω_s increases and therefore the energy of the signal beam is amplified, hence the name Optical Parametric Amplification. However, after the stimulated emission the media will be in an excited state of energy $\hbar\omega_i$, which will lead to the spontaneous emission of a photon of frequency $\omega_i = \omega_p - \omega_s$, hence the name Difference-Frequency Generation. This will result in a new beam commonly called ”idler”, which in some cases can be our desired output. For amplification purposes, the remaining pump and the idler are, normally, filtered after the OPA leaving only the amplified signal. In the case of Fig.2.3 we can observe that the pump is not filtered immediately after the DFG, this is because we have another OPA stage after and the remaining pump can be used. The main issue of simple OPA is that the media will be exposed to a considerable amount of energy in an extremely short time, which can easily damage the solid materials used during the amplification. To prevent this, one relies on OPCPA. In this case, before the OPA the pulse is temporally stretched, by introducing chirp, and temporally compressed after the OPA, by removal of said chirp [2], in both cases by using a carefully designed dispersion device. Chirp is usually understood as the time dependence of its instantaneous frequency[2], in essence, the different frequencies that constitute the pulse travel different optical paths so that some of the frequencies are ”faster” or ”slower” than the rest leading to temporal stretching or compression. In OPCPA, since the pulses are stretched, when they arrive at the OPA stage, the media only interacts with a fraction of the power of the original pulse, which avoids damage and, therefore, allows amplifying pulses with higher energy than what regular OPA would allow.

---

[1] While the physical principle is the same, in practice OPA and DFG serve different purposes. While OPA is used to amplify signals, DFG is used to generate signals in different wavelengths.

Finally, regarding the *Starzz* (Fig.2.3), the 1030 nm beam generated by the *Amphos2000* is divided into

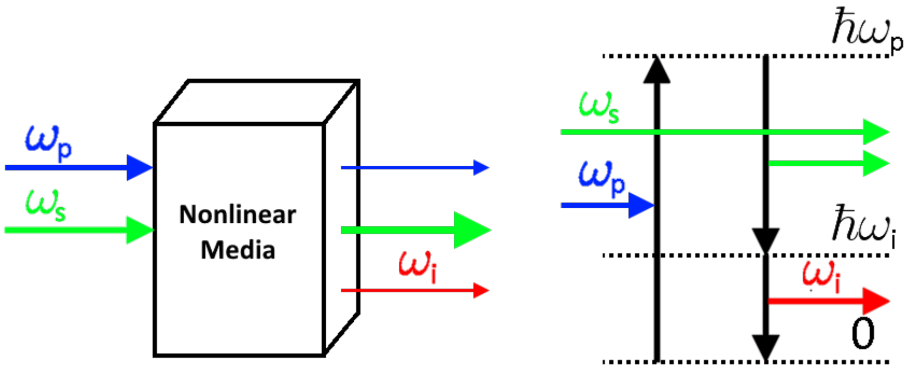

Figure 2.2: Schematics of OPA or DFG. On the left there is a macroscopic view in which the pump (blue; ω_p) and the signal (green; ω_s) interact inside a nonlinear media, resulting in energy loss by the pump, energy gain by the signal, and the emission of a third frequency commonly known as idler (red; ω_i). On the right, the band structure of this process where a pump photon excites the material to a virtual level, which leads to the emission of a signal photon by stimulated emission followed by emission of one idler photon by spontaneous emission.

multiple beams, with most being directed to the different stages of OPA to serve as a pump. Note that the internal optics are designed so that the pump and signal pulses arrive simultaneously at each amplification stage. A fraction of the 1030 nm pulse is used to perform SCG generating a broad spectrum pulse around 1550 nm that is then filtered and stretched. This pulse is then sent to the first OPA as a signal to increase its energy and then introduced in the *Dazzler*. The *Dazzler*, an acousto-optic modulator, is a *FASTLITE* tool for compression optimization and Carrier-Envelope Phase (CEP) stabilization. From there the beam enters a stage of DFG where the idler that comes from this process at 3 μm becomes the new signal that feeds two consecutive stages of OPA, for these stages note that the pump is removed immediately after. Finally, the 3 μm pulse goes through a compressor that removes its chirp leading to temporal compression. This system was designed to work in a saturation regime, by receiving short pulses of 1 ps at 100 kHz with an average power of 75.5 W and an ellipticity of 1. The final output is a pulsed 3 μm beam which consists of short 40 fs pulses delivered at 100 kHz and an average power of 6.5 W. However, since the pump at the time was below the specified requirements the average power was around 4.8 W.

---

[2] The first temporal derivative of the pulse’s phase [2].

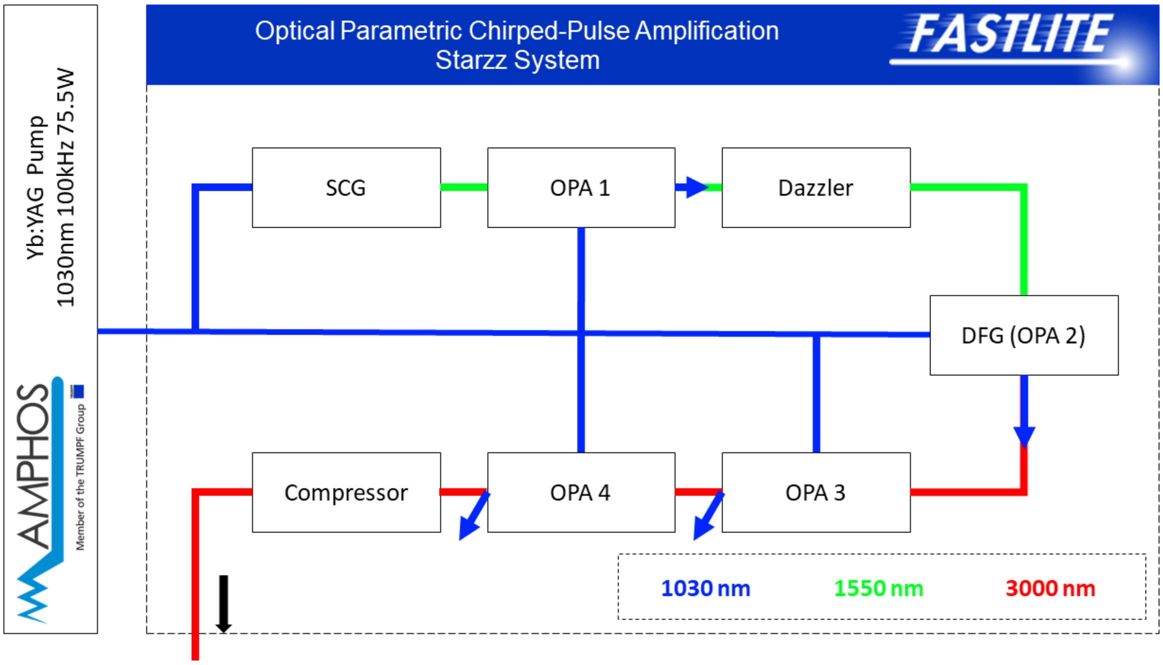
Yb:YAG Pump
1030nm 100kHz 75.5W
AMPHOS
Member of the TRUMPF Group
Optical Parametric Chirped-Pulse Amplification
Starzz System
FASTLITE
SCG
OPA 1
Dazzler
DFG (OPA 2)
Compressor
OPA 4
OPA 3
1030 nm
1550 nm
3000 nm

Figure 2.3: Schematic of the 3 μm laser system.

3

Nonlinear spectral broadening

Contents

3.1 Physical principles in solid materials 15

3.1.1 Self-Phase Modulation 15

3.1.2 Self-steepening 16

3.1.3 Self-focusing, filamentation and conical emission 18

3.1.4 Effects of dispersion on Supercontinuum Generation 19

3.1.5 Stimulated Raman Scattering 19

3.2 Experimental Work 21

3.2.1 Setup 21

3.2.2 Methods and Results 23

3.3 Numerical simulation of spectral broadening 28

3.3.1 Theoretical approach 28

3.3.2 Numerical values and results 30

In the beginning, spectral broadening was performed based solely on linear effects. However, as laser systems became more and more powerful a new range of nonlinear phenomena became available. Among these, nonlinear broadening allowed generating wider spectral widths and consequently shorter pulses. In some cases, the spectra were so large that the term supercontinuum was born. A supercontinuum, many times referred to as a white-light laser, is characterized by an ultrabroad continuous spectrum, although the term ”continuous” can be relaxed. Naturally, the generation of high-energy ultrashort pulses with an ultrabroad spectrum is of great scientific and technological interest. The applications of supercontinuum include, but are not limited to, optical coherence tomography, fluorescence microscopy, flow cytometry, characterization of optical devices, generation of multiple carrier waves in optical fiber communications systems, and the measurement of the carrier-envelope offset frequency of frequency combs [2]. Another application, that we observe in this work, is actually in the 3 μm laser system itself where the OPCPA enclosure includes a stage of SCG to generate pulses at 1.55 μm (Fig.2.3).
In this chapter we present the results of spectral broadening in the normal and anomalous dispersion regime, the latter leading to SCG. We also present a simulation of spectral broadening in the normal regime with a discussion on the implications on the nonlinear interactions inside the media.

3.1 Physical principles in solid materials

3.1.1 Self-Phase Modulation

As the name indicates, Self-Phase Modulation (SPM) is the modulation of the phase of the wave due to a self-generated phase, φ_{SPM}, caused by the intensity-induced variation of the medium's refractive index. Let us consider an optical pulse with an electric field given by

$$E(z,t) = \mathcal{A}(z,t)e^{i(\omega_0 t - k_0 z)} + c.c. = \mathcal{A}(z,t)e^{i\omega_0 (t - \frac{n}{c}z)} + c.c, \tag{3.1}$$

where $\mathcal{A}(z,t)$ is the complex field envelope, z the position, t is time, ω_0 the central frequency, $k_0 = \omega_0 n/c$ the wavenumber, n the refractive index of the medium, and c the speed of light in vacuum. Now let us propagate this pulse in a medium of refractive index:

$$n(t) = n_0 + n_2 I(t), \tag{3.2}$$

where $I(t) = |\mathcal{A}(z,t)|^2$ is the intensity, and n_0 and n_2 are the linear and nonlinear refractive indexes, respectively. The dependence of n with I is known as the optical Kerr effect, which is associated with a $\chi^{(3)}$ electric susceptibility, such that the polarization of the medium, P, possesses a linear and cubic dependence on the electric field:

$$
\begin{aligned}
P = \varepsilon_0 \chi E = \varepsilon_0 \chi^{(1)} E + \varepsilon_0 \chi^{(3)} |E|^2 E \\
\chi = \chi^{(1)} + \chi^{(3)} |E|^2.
\end{aligned}
\tag{3.3}
$$

where $\varepsilon_0 = 8.854 \times 10^{-12}$ F/m is the electric permittivity of vacuum. Due to this, materials that present this kind of behaviour are many times called Kerr or $\chi^{(3)}$ (Chi-3) materials, while materials that present a square dependence (Pockels effect) are referred to as Pockels or $\chi^{(2)}$ (Chi-2) materials. In general the term $n_2 I$ is many times smaller than n_0, since the magnitude of n_2 ranges from 10^{-20} to 10^{-6} m^2/W [14], therefore we can only observe this kind of effects when I(t) reaches extremely high values, e.g. $\sim 10^{13}$ W/m^2 for fused silica [20].

Combining equations 3.1 and 3.2 we obtain inside the complex exponential term [21, 22]

$$
\begin{aligned}
\omega_0 \left(t - \frac{n}{c} z\right) &= \omega_0 \left(t - \frac{n_0}{c} z\right) - \omega_0 \frac{n_2 I(t)}{c} z \\
&= \omega_0 \left(t - \frac{n_0}{c} z\right) + \varphi_{SPM} \\
&= \omega_0 \left(t - \frac{n_0}{c} z\right) + \int_0^t \Delta\omega \, dt,
\end{aligned}
\tag{3.4}
$$

where

$$
\varphi_{SPM} = -\omega_0 \frac{n_2 I(t)}{c} z,
\tag{3.5}
$$

and

$$
\Delta\omega = \frac{d}{dt}\left(-\omega_0 \frac{n_2 I(t)}{c} z\right) = -\frac{\omega_0 z}{c} n_2 \frac{dI(t)}{dt}.
\tag{3.6}
$$

Equation 3.6 describes the frequency shift, $\Delta\omega$, induced by the additional phase, φ_{SPM}. As we can see, in the case of e.g. a regular Gaussian pulse the front of the pulse ($dI(t)/dt > 0 \Rightarrow \Delta\omega < 0$) will be shifted to lower frequencies (red/Stokes shifted) while the the back of the pulse ($dI(t)/dt < 0 \Rightarrow \Delta\omega > 0$) will shift to higher frequencies (blue/Anti-Stokes shift). These shifts are responsible for broadening the pulse spectrum and will induce up-chirp in the pulse in the center of the pulse (Fig.3.1), meaning that the instantaneous frequency increases.

3.1.2 Self-steepening

We have just seen that the intensity dependence of the refractive index can lead to changes in the pulse spectrum. In this section, we talk about one of the temporal consequences of this dependence.

From equation 3.2 we see that the refractive index can have a temporal dependence, which is critical in the propagation of laser pulses since the intensity changes with time. Because of this the center of a Gaussian pulse, where the intensity is higher, experiences a much higher refractive index, and conse-

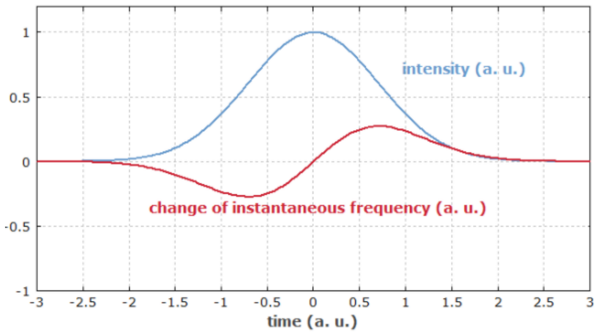

Figure 3.1: Instantaneous frequency of an initially unchirped pulse which has experienced self-phase modulation. The central part of the pulse exhibits an up-chirp. Taken from [2].

quently lower group velocity, than its wings. This would make the center of the pulse, apparently, ”move” to the back of the pulse, leading to an increase of the slope in that region (Fig.3.2). This self-induced steepening of the trailing edge of the pulse is known as self-steepening, while the resulting sharp intensity gradient is referred to as an optical shock.

One additional mechanism for self-steepening is the production of free[1] electrons [21] by the peak of the pulse, which reduce the refractive index. In this situation, only the back of the pulse will propagate in these electrons, which will make it faster than the rest of the pulse, thus increasing further the steepening.

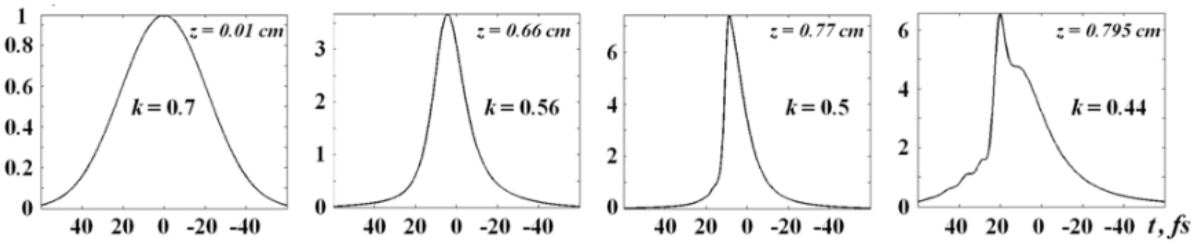

Figure 3.2: Formation of a light bullet and consequent self-steepening during propagation in fused silica. z is the propagation distance. Taken from [23].

Self-steepening does not induce spectral broadening by itself, however when combined with SPM is one of the most crucial mechanisms in SCG. As we have seen in section 3.1.1 the frequency shift is proportional to dI(t)/dt, because of self-steepening the back of the pulse will have a much sharper slope, meaning a much higher value of dI(t)/dt, leading to a much greater blue-shift and therefore a larger spectral broadening in the higher frequency range.

---

[1] Electrons whose kinetic energy is large enough that they can move through the lattice without being trapped by localized potential wells.

3.1.3 Self-focusing, filamentation and conical emission

One of the most important consequences of SPM is self-focusing [22, 24]. As we see in equation 3.2, when an optical beam crosses a material exhibiting the optical Kerr effect the refractive index will change in a pattern equal to the transverse intensity distribution of the beam. If the intensity is maximum at the center of the beam and then strictly decreases to its edges, e.g. Gaussian beam, the material will act as a positive lens focusing the beam inside the medium.

The critical power necessary to achieve self-focusing with a Gaussian beam is given by [24]

$$P_c = \frac{3.77\lambda_0^2}{8\pi n_0 n_2}, \tag{3.7}$$

where λ_0 is the central wavelength. The propagation distance until the focus plane is given by [24]

$$z_f = \frac{\sqrt{0.135}k_0 w_0^2}{\left[\left(\sqrt{\frac{P}{P_c}} - 0.852\right)^2 - 0.0219\right]^{\frac{1}{2}}}, \tag{3.8}$$

where w_0 is the waist radius of the beam.

As the beam self-focuses, the intensity in the center increases leading to the creation of free electrons. This increased electronic density will lead to self-defocusing. At some point, the intensity will be high enough to counteract the self-focusing (clamping intensity). Once this happens, the intensity will drop reducing the electronic density and therefore the self-defocusing, allowing the beam to once again self-focus and restart the cycle. This will generate a series of energetic ”hot spots” along the propagation axis many times known as filaments [21, 22, 25]. This localized increase in intensity and electronic density can increase dramatically the broadening, as such it is one of the main mechanisms behind SCG.

The formation of these filaments leads to a gradient of electronic density in the direction of propagation

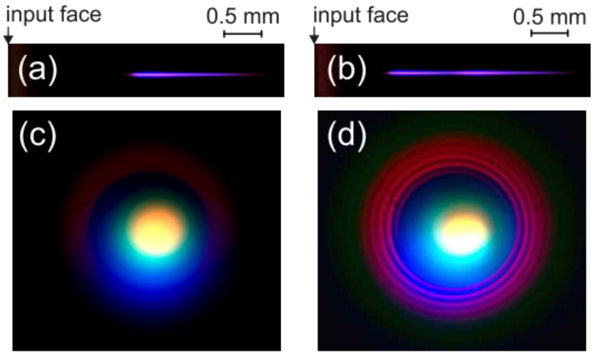

Figure 3.3: Plasma fluorescence traces in a YAG crystal induced by self-focusing of 100 fs, 800 nm input pulses with energies of **(a)** 310 nJ, **(b)** 560 nJ, that induce a single self-focusing event and refocusing of the filament, respectively. **(c)** and **(d)** show the corresponding far-field patterns of supercontinuum emission. Note the conical emission pattern surrounding the white-light (supercontinuum). Taken from [25].

but also in the transverse plane of the beam. The latter can cause frequency-dependent divergence forming rainbow rings of light around the main beam with the higher frequencies further from the axis (see e.g. Fig.3.3). This phenomenon is known as conical emission [21,22].

3.1.4 Effects of dispersion on Supercontinuum Generation

Dispersion is a linear phenomenon in which the refractive index of a medium depends on the frequency of the propagating light. For propagation purposes this phenomena is described by a mode propagation constant, β, normally defined in a Taylor expansion [26]:

$$\beta(\omega) = n(\omega)\frac{\omega}{c} = \beta_0 + \beta_1(\omega-\omega_0) + \frac{1}{2}\beta_2(\omega-\omega_0)^2 + ..., \ \beta_m = \left(\frac{d^m\beta}{d\omega_m}\right)_{\omega=\omega_0}. \tag{3.9}$$

Since $\beta_1 = 1/v_g$, where v_g is the group velocity, then $\beta_2 = d\beta_1/d\omega$ describes the variation of group velocity with the frequency. Because of this β_2 is commonly known as Group Velocity Dispersion (GVD) [26]. Dispersion is many times classified into normal ($\beta_2 > 0$; higher frequencies travel slower) and anomalous dispersion ($\beta_2 < 0$; higher frequencies travel faster).

In normal dispersion (Fig.3.4a and Fig.3.4d), since SPM induces red and blue-shift in the front and back of the pulse, respectively, the effect can lead to the formation of two sub-pulses moving in opposite directions in the pulse's frame (pulse splitting). This is followed by a considerable broadening due to self-steepening, higher in the blue-shift than in the red-shift, capable of forming a supercontinuum [25]. One must notice that this can compete with filamentation since the added electronic density makes the back of the pulse move faster and normal dispersion slower.

As for anomalous dispersion (Fig.3.4c and Fig.3.4f) the opposite occurs and the pulse self-compresses in the time domain [25, 27], a phenomenon often referred to as light bullet [23, 28]. The formation of light bullets increases the intensity and, together with filamentation, improves self-steepening, thus potentiating a larger SCG. In this regime SCG is also marked by the formation of isolated spectral wings in the visible spectral region, which seem to be associated with the superposition of light waves that were scattered by the polarization waves [29] caused by the passage of the pulse.

For wavelengths near the zero dispersion (Fig.3.4c and Fig.3.4e), the resulting broadening is much more symmetric than the previous regimes and combines some of the aspects of the two, although the temporal evolution of the pulse is much more similar to the one observed in the normal regime, even for the slightly anomalous wavelengths, since the dispersion is too low to self-compress the pulse [25].

3.1.5 Stimulated Raman Scattering

In section 2.2 we saw that OPCPA allows converting a high-energy photon (pump) into two lower energy photons: one by stimulated emission due to the presence of a signal beam; and one by spontaneous

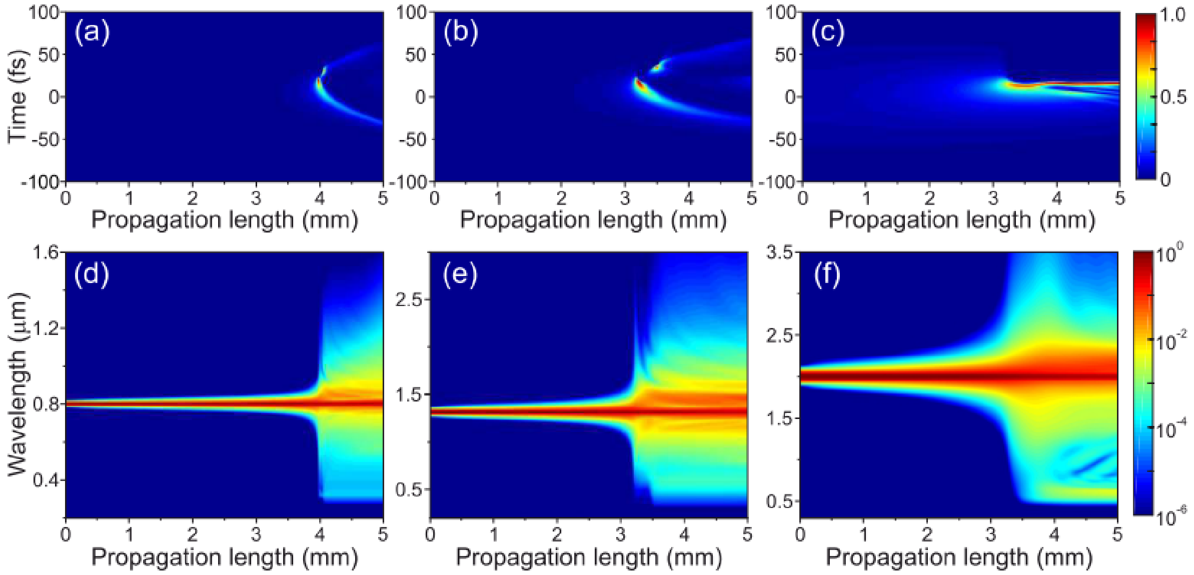

Figure 3.4: Top row: numerically simulated temporal dynamics of 100 fs laser pulses propagating in sapphire crystal with the input wavelengths of **(a)** 800 nm, **(b)** 1.3 μm, **(c)** 2.0 μm, representing the filamentation regimes of normal, zero and anomalous GVD, respectively. Bottom row shows the corresponding spectral dynamics. Notice, how the spectral broadening in the regimes of normal and zero GVD is associated with the pulse splitting, and the spectral broadening in the regime of anomalous GVD is associated with pulse self-compression. Taken from [25].

emission with the remaining energy from the pump (idler). In this mechanism, the medium itself should remain unchanged since it returns to the ground state, which is, in short, the definition of a parametric process. Stimulated Raman Scattering (SRS) (Fig.3.5) is quite similar to OPCPA, the difference lying in how the extra energy from the pump photon is released. While in OPCPA this energy goes to the idler photon, in SRS that energy is transferred to the vibrational modes of the medium [14].

This process does not generate the supercontinuum as a stand-alone. However, if other mechanisms have previously generated photons with different frequencies, then SRS can use them as signal and/or pump, broadening the pulse even more. Note that this added broadening will be into the lower frequencies since SRS can only generate photons of lower energy than the pump (Stokes shift). Although the SRS response is of extreme importance when working with optical fibers, it is negligible as long as the propagation length is shorter than the dispersion length [26], which is given in terms of the pulse width T_0 as $L_D = T_0^2/|\beta_2|$.

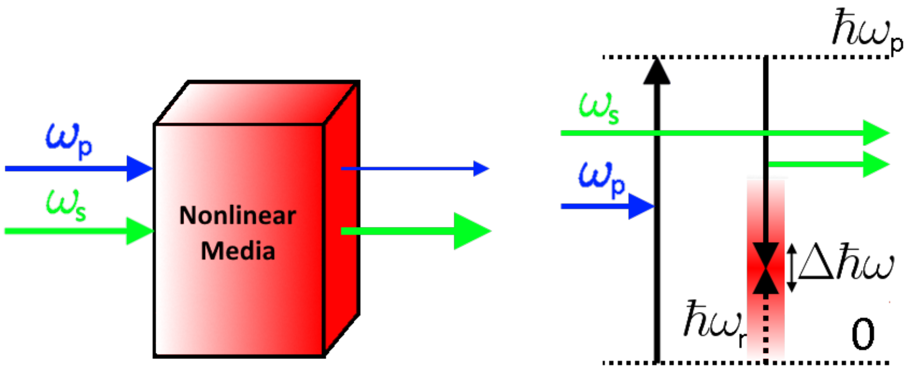

Figure 3.5: Schematic of SRS. Left: macroscopic view in which the pump (blue; ω_p) and the signal (green; ω_s) interact inside a nonlinear medium where there is an excitation of vibrational modes. Right: band structure of this process, where a pump photon excites the material to a virtual level, which leads to the emission of a signal photon by stimulated emission, while the excess energy is transferred to a vibrational mode of the medium, (black dashed; $\hbar\omega_r$). The medium has a gain curve with a certain bandwidth, (red; $\Delta\hbar\omega$), which goes to zero as $\hbar\omega_r \approx 0$.

3.2 Experimental Work

3.2.1 Setup

The data for SCG at 3 μm is the result of a "failed" attempt to acquire harmonics where the continuum masked the harmonic signal. This data was obtained with a standard spectrometer based in Si with a spectral range of 147 – 1127 nm. Unfortunately, this does not include the entirety of the supercontinuum, for that we would need to also measure the spectrum with a MIR spectrometer and possibly a Ultraviolet (UV) spectrometer, which can be rather expensive.

For the generation of harmonics, we started with a low-power setup, however as some of our more interesting samples did not produce any visible results we changed to a high-power setup, Fig.3.6. In both cases, 40 fs laser pulses centered at 3 μm with an average power of 4.8 W and repetition rate of 100 kHz are sent to a telescope composed by a 200 mm and a 100 mm focal lenses (f1 and f2, respectively) placed 300 mm apart, in order to resize and collimate the beam radius to fit the remaining components. Then the beam was redirected and focused (lens f3) on a sample window, place in a rotation mount attached to a translation stage, for the generation of harmonics, or in this case supercontinuum. The output of the sample is then collimated by a 75 mm focal lens (f4) into a dispersion prism to separate the different components of the spectrum.

To measure the supercontinuum we sent all of these components to an integrating sphere connected

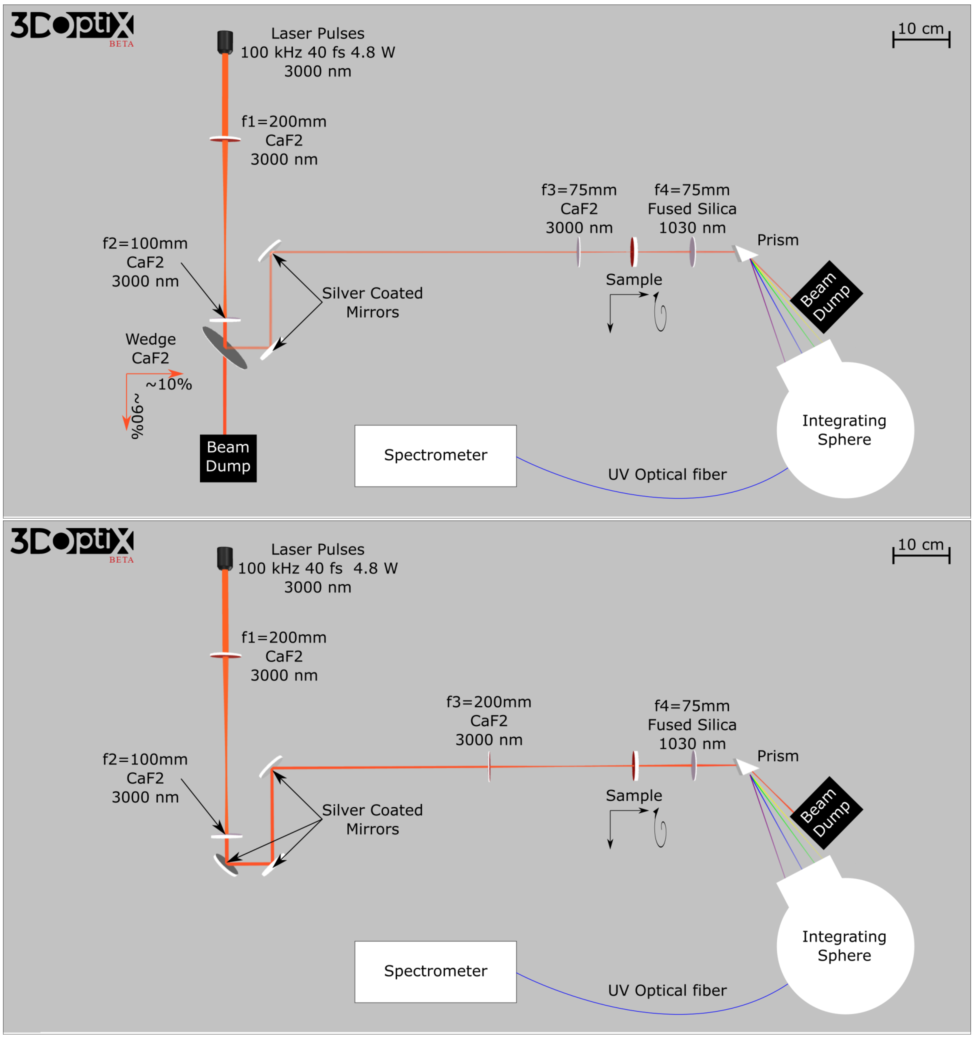
3DOptiX BETA
Laser Pulses
100 kHz 40 fs 4.8 W
3000 nm
10 cm
f1=200mm
CaF2
3000 nm
f3=75mm
CaF2
3000 nm
f4=75mm
Fused Silica
1030 nm
Prism
f2=100mm
CaF2
3000 nm
Silver Coated
Mirrors
Sample
Beam
Dump
Wedge
CaF2
~10%
~90%
Integrating
Sphere
Beam
Dump
Spectrometer
UV Optical fiber
3DOptiX BETA
Laser Pulses
100 kHz 40 fs 4.8 W
3000 nm
10 cm
f1=200mm
CaF2
3000 nm
f3=200mm
CaF2
3000 nm
f4=75mm
Fused Silica
1030 nm
Prism
f2=100mm
CaF2
3000 nm
Silver Coated
Mirrors
Sample
Beam
Dump
Integrating
Sphere
Spectrometer
UV Optical fiber

Figure 3.6: Experimental setup for the acquisition of SCG at 3 µm. Top: setup with 10% of the output power using a wedge. Bottom: setup with the full power.

by an UV optical fiber to a spectrometer (*FLEX-STD-UV-Vis-NIR*, *SARSPEC*). However, to protect the UV optical fiber, which was not made to handle high-power in the MIR, we placed a beam dump in front of the fundamental beam. The two setups displayed in Fig.3.6 differ mainly in two aspects: the amount of energy sent to the sample and the nature of the focus. In the low-power (∼ 0.48 W) setup, after the telescope, the beam is split by a calcium fluoride wedge that sends only around 10% of the beam power to the sample. The beam then goes through a tight focus to increase the intensity in the sample. On the other hand, in the high-power (4.8 W) setup, the full power is sent to the sample by a silver mirror but with a softer focus. The reason for the softening is to avoid damaging the samples.

We also tried to perform SCG at 1.03 µm resulting in a nonlinear spectral broadening but not at a scale that could be labeled as supercontinuum. The power of the laser was set to the maximum output delivering 1 ps laser pulses a 100 kHz. The beam then crosses a power control stage consisting of a half-wave plate (rotates the beam's polarization) and a polarizer, which sends 82 W to the rest of our setup. This control stage is only used during some diagnostics of the *AMPHOS* system so during our experiments nearly all the power was sent to the samples and any small portion crossing the polarizer was blocked by a beam dump. Then the beam is focused by a lens with a focal length of 400 mm. The samples for spectral-broadening were then placed slightly after the focus in order for the beam to be diverging as it enters the sample to counteract the effect of self-focus, and therefore reduce the possibility of catastrophic collapse of the pulse or damage to the samples. The broadened pulse was then sent to an integrating sphere connected by an optical fiber to a spectrometer (*FLEX-STD-UV-Vis-NIR*, *SARSPEC*). However, because the energy of the beam is too high to pass through our UV optical fiber we first use a wedge to only reflect 10% of the energy to a series of 7 absorptive filters (NENIR, THORLABS) with growing Optical density (OD) in the following sequence: OD=0.1, 0.2, 0.3, 0.4, 0.5, 0.6 and 1. The increase of the OD prevents that a single filter absorbs too much energy and gets damaged. The setup is presented in Fig.3.7.

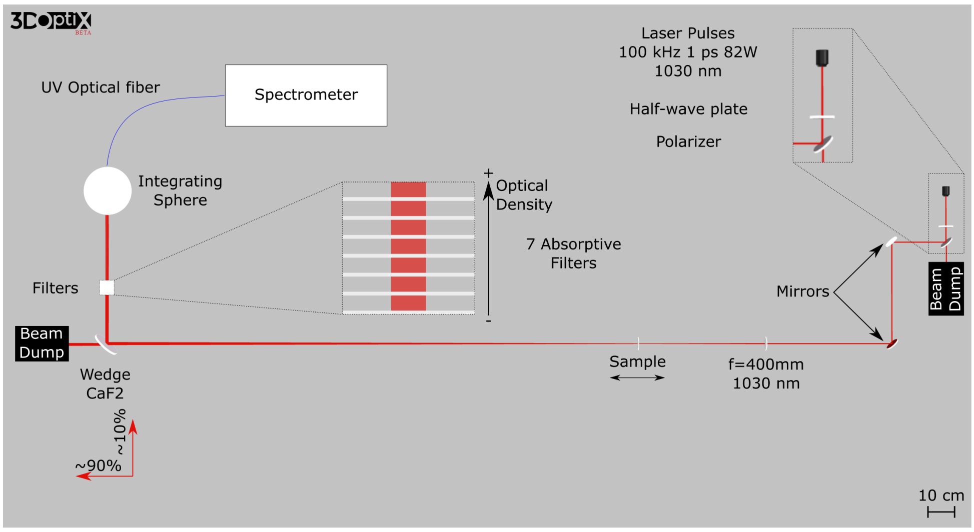
3DOptiX
BETA
Laser Pulses
100 kHz 1 ps 82W
1030 nm
Half-wave plate
Polarizer
UV Optical fiber
Spectrometer
Integrating Sphere
+
Optical Density
-
7 Absorptive Filters
Filters
Mirrors
Beam Dump
Beam Dump
Wedge CaF2
Sample
f=400mm
1030 nm
~10%
~90%
10 cm

Figure 3.7: Experimental setup for the acquisition of spectral broadening at 1.03 µm.

3.2.2 Methods and Results

3.2.2.1 Supercontinuum Generation at 3 µm

We observed SCG with a total of 6 samples: Infrared (IR) grade CaF$_2$ (3 mm thick), UV grade fused silica (5 mm), sapphire (1 mm), and three samples of undoped yttrium aluminium garnet (YAG) (1 mm, 2 mm and 4 mm). This data should be taken as a proof of concept for future experiments with this laser system. A possible explanation as for why it was not possible to achieve SCG in the 1.03 µm is related to the different dispersive regimes since the anomalous regime potentiates a larger spectral broadening,

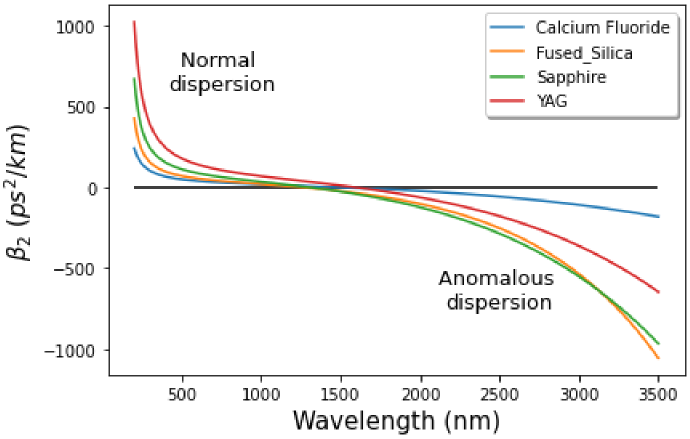

Figure 3.8: Group Velocity Dispersion for the four samples used in the spectral broadening at 1.03 µm. Calculated with the code in listing B.2.

as mentioned in section 3.1.4. In fact, all the samples used exhibit anomalous dispersion around 3 µm, whereas at 1.03 µm they exhibit normal dispersion, Fig.3.8. We notice that in Fig.3.9 we can see only the wings of the supercontinuum. This observation is in agreement with previous experimental works in the anomalous dispersion regime using MIR sources up to 2.5 µm [29–31].

In particular the spectra of CaF_2 and fused silica which present a similar shape to the ones observed in [30] with an input laser field at 2.2 µm. One must also notice that when we tried a 1 mm CaF_2 sample no supercontinuum was generated, even at high-power. The obtained spectra are depicted in Fig. 3.9.

The YAG samples generated supercontinuum in the low-power (0.48 W) setup with the wedge, and as such we never observed clean harmonics in these samples. The other samples only generated supercontinuum in the high-power (4.8 W) system using the mirror. Additionally, in Fig.3.9d we see a sharp increase in the count rate and the formation of a peak near the 1100 nm when the propagation length increases from 1 mm to 2 mm but a very small variation when increasing further to 4 mm. One possibility is that, unlike the larger samples, in the smaller sample the beam could not propagate enough to form a long filament thus reducing the SCG.

This strong dependence on the propagation distance is also reflected in our 1 mm sapphire sample (the thinnest of this set of experiments) which presents the smaller wings.

On a final note in the laboratory, we also observed the generation of conic emission, Fig.3.10, associated with filamentation.

3.2.2.2 Spectral broadening at 1.03 µm

In order to correct the effect of the filters (Fig.3.7) in yield of the spectrometer the transmission data from the manufacturer was interpolated, Fig.3.11. With this, we calculate the transmission at each point, allowing to reconstruct the expected yield without filtering. The effect of the CaF_2 wedge was neglected

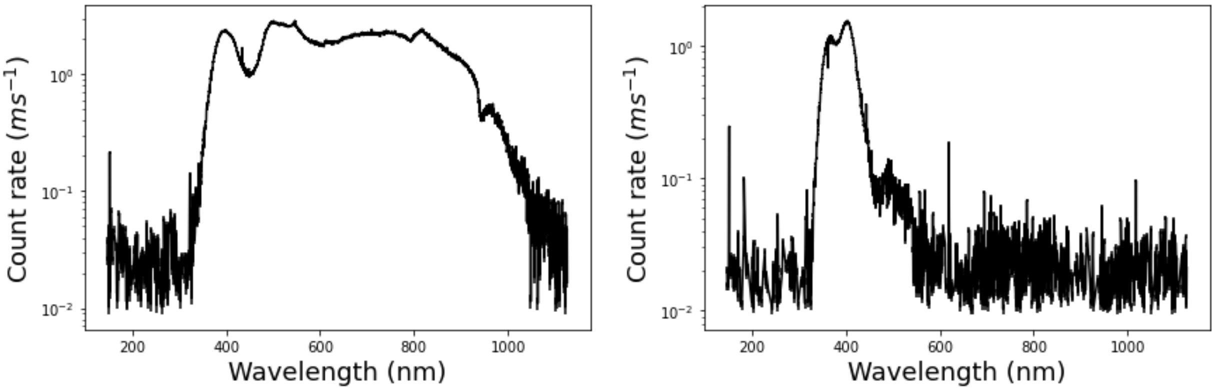

(a) CaF_2 sample, 24.5 cm after focal lens.

(b) Fused silica sample, 23.5 cm after focal lens.

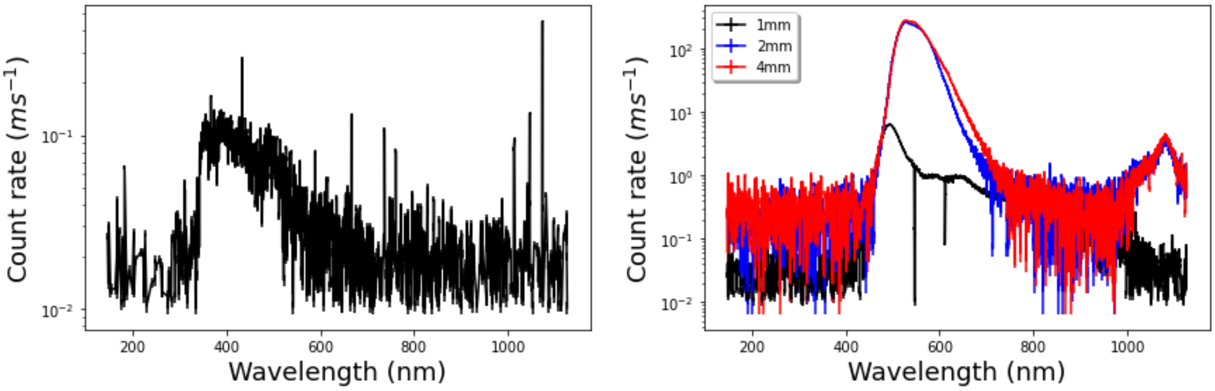

(c) Sapphire sample, 23.5 cm after focal lens.

(d) YAG samples, placed at focus.

Figure 3.9: Supercontinuum Generation at 3 µm.

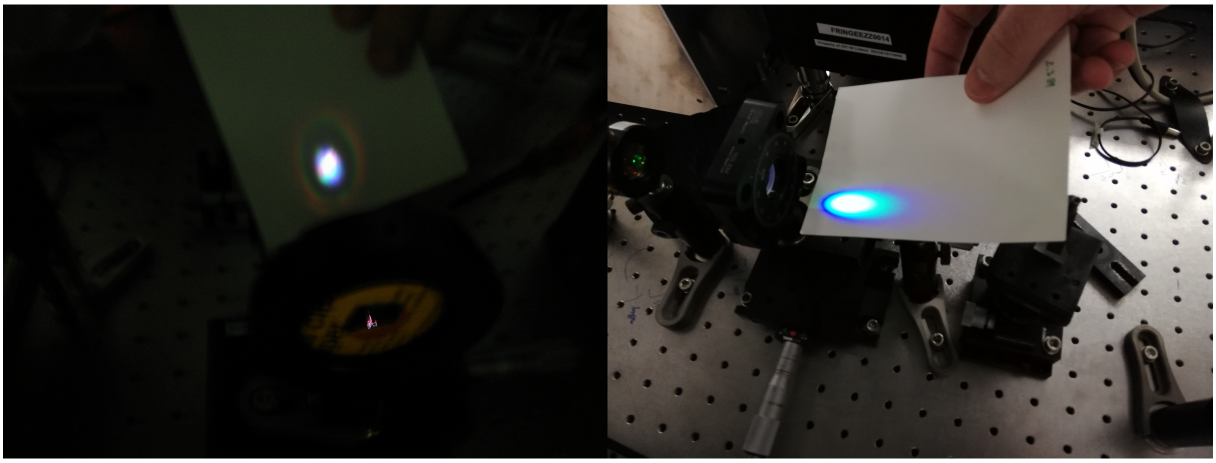

Figure 3.10: Conical emission with a 3 µm laser. In the left with a 5 mm fused silica sample and in the right with a 4mm YAG sample. Note the white-light at the center of the beam (supercontinuum).

as the transmission curve is flat in the spectral region of interest.

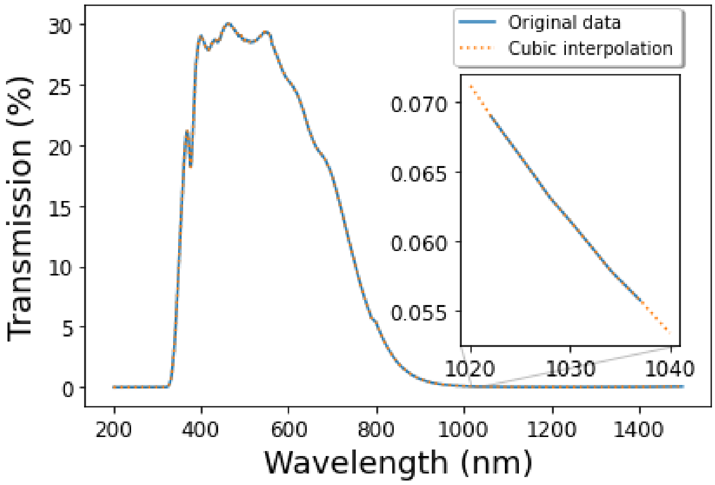

Figure 3.11: Interpolation of the multiplied data from all seven filters. In the inset the region of interest for Fig.3.12.

The overall results from the reconstructed data are depicted in Fig.3.12. The captions correspond to the percentage of the full power sent to the sample while the inset depicts the variation of the spectral full width at half maximum (FWHM) of the spectrum with the power. The FWHM was obtained from a Orthogonal distance regression (ODR) fit to a Gaussian: $a \cdot \exp[-0.5(\lambda-\mu)^2/\sigma^2]$, FWHM= $2\sqrt{2\ln 2}\sigma$. The entire data can be seen on Appendix A.

We started by placing a 5 mm thick UV grade fused silica sample 47 cm after the lens, then changed the laser output power and acquired the spectrum for each value. In this case (Fig.3.12a) we observe that for lower levels the increase of power only changes the rate of counts, but as the power is increased the pulse energy starts to spread over a wider bandwidth leading to broadening that grows with power, a clear signal of nonlinear broadening. Additionally we notice a small asymmetry in this broadening with a more accentuated growth in the lower wavelengths/higher frequencies, in all likelihood due to self-steepening.

When the fused silica sample was moved closer to the lens (45 cm apart) the observed broadening increases due to the higher intensity. Here the broadening is significantly more visible, Fig.3.12b, and the effect of self-steepening is considerably more apparent. As we moved the sample to 43.5 cm after the lens, the intensity was enough to cause laser-induced damage at 25%, so the power was lowered to 21% to check the state of the spectrum. This is quite visible Fig.3.12c with a sharp drop in the measured FWHM from 20% to 21% of power and the overall smaller broadening compared with Fig.3.12b and Fig.3.12a. It is likely that up to 15% the material had already some superficial damage from the previous experiments and at 25% the intensity was enough to damage the sample in the entirety of the beam's path. Upon closer inspection, the optical damage was not shaped as straight line, but instead as series of damage spots crossing the sample. This was likely due to filamentation.

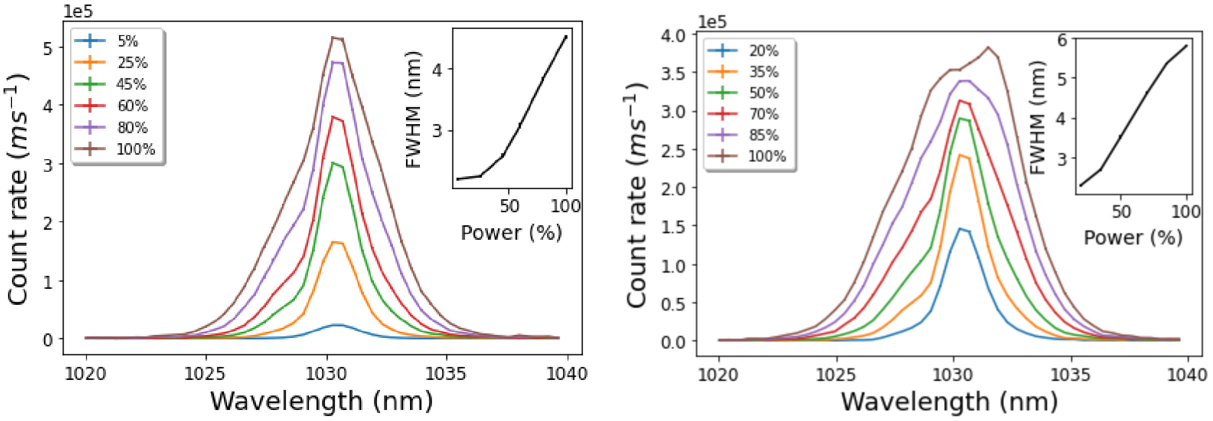

(a) Fused silica sample 47 cm away from the lens.

(b) Fused silica sample 45 cm away from the lens.

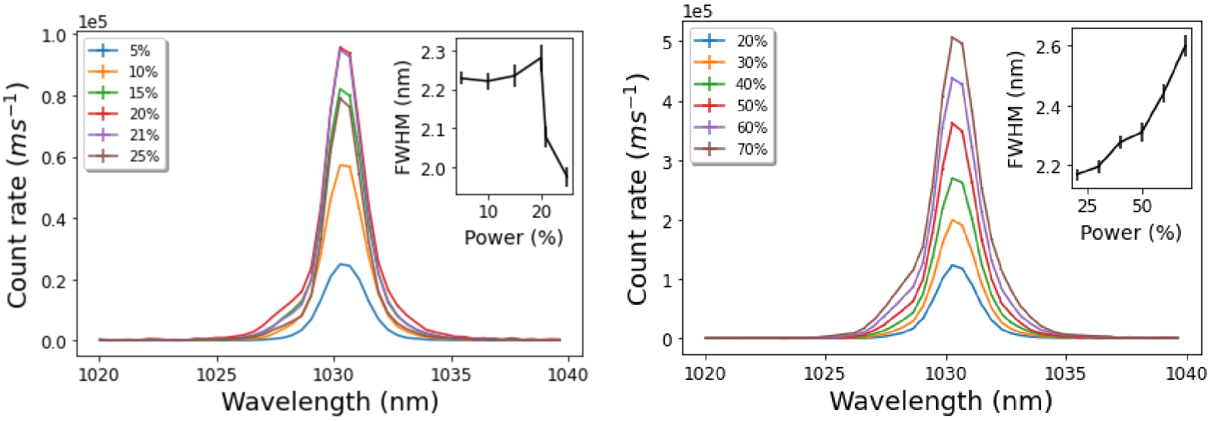

(c) Fused silica sample 43.5 cm away from the lens.

(d) CaF_2 sample.

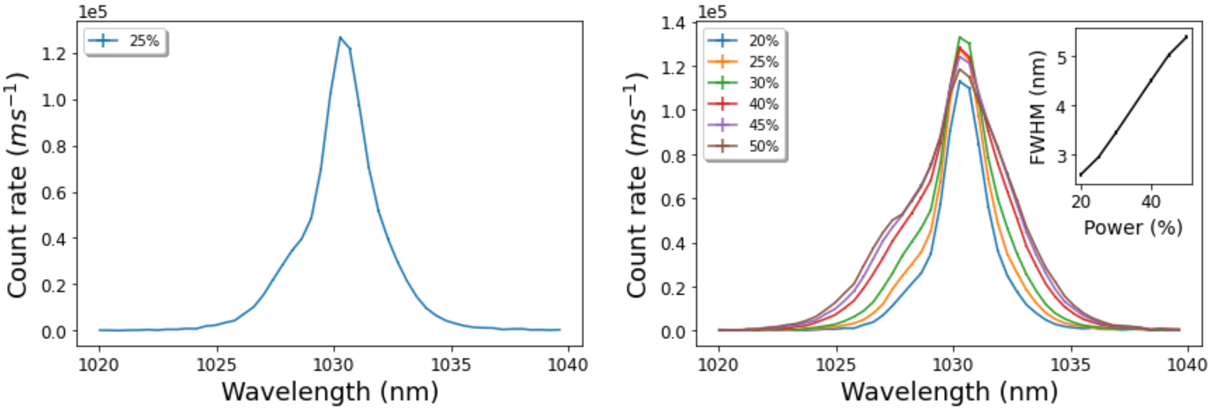

(e) Sapphire sample, FWHM= 3.2 nm.

(f) YAG sample.

Figure 3.12: Spectral broadening at 1.03 µm. The captions are the percentage of the full power (82 W) sent to the sample. The insets depict the variation of FWHM with the power.

In order to protect our samples the remaining experiments were performed 45 cm away from the lens. When we used a 1 mm thick UV grade CaF_2 window, Fig.3.12d, although we observe once again the immediate increase of the broadening with power, the FWHM is much smaller than observed in all other (non-damaged) samples. This can be associated with the propagation length being shorter when compared to the other samples, thus reducing the magnitude of effects such as SPM, self-steepening, self-focus, or filamentation that build up during propagation. In contrast, we took a single spectrum with a 15 mm thick sapphire sample at 25% power, Fig.3.12e, which resulted in a higher broadening than for CaF_2 at full power proving the importance of long propagation distances. Finally, we used a 4 mm YAG sample, Fig.3.12f, which depicted a remarkable asymmetry in the spectrum due to self steepening.

3.3 Numerical simulation of spectral broadening

3.3.1 Theoretical approach

In this section, we present the results of numerical simulations for spectral broadening at 1.03 μm, with the goal of comparing them with the experimental results from the previous section. The absence of published values for the nonlinear coefficient at 3 μm prevents us from performing simulation for that wavelength.

Historically speaking the study of spectral broadening has been centered on optical fibers and therefore there are yet no easy access/free software/codes to simulate nonlinear broadening in bulk crystals. As such since the scope of this thesis is mainly experimental these simulations were performed using an open-source Python package: PyNLO[2].In particular, we take advantage of the crystal dispersion calculators and the solver for the propagation of light through a $\chi^{(3)}$ optical fiber, in our case an ”equivalent” optical fiber that represents our samples. The validity of our model is discussed at the end of this section. The propagation is based on a Split-step Fourier Method to solve the Generalized Nonlinear Schrödinger Equation (GNLSE) as described in [32]. The GNLSE employed takes the following form:

$$\begin{aligned}\frac{\partial \mathcal{A}}{\partial z} = & -\frac{\alpha}{2} - \left(\sum_{m\geq 2} \beta_m \frac{i^{m-1}}{m!} \frac{\partial^m}{\partial t^m} \right) \mathcal{A} \\ & + i\gamma \left(1 + \frac{1}{\omega_0}\frac{\partial}{\partial t} \right) \times \left((1-f_R)\mathcal{A}|\mathcal{A}|^2 + f_R \mathcal{A} \int_0^{\infty} h_R(\tau)|\mathcal{A}(z,t-\tau)|^2 d\tau \right),\end{aligned} \tag{3.10}$$

where α is the attenuation coefficient, β_m the dispersion coefficients, γ the nonlinear coefficient, f_R the fractional contribution of the delayed Raman response to nonlinear polarization, and $h_R(t)$ is the Raman response function related to vibrations of the molecules.

---

[2] pyNLO-Nonlinear optics modeling for Python: `https://pynlo.readthedocs.io/en/latest/readme_link.html` and `https://github.com/pyNLO/PyNLO`, Version 0.1.2

The terms on the right-hand side represent respectively losses, dispersion, and nonlinear effects. In the third term, $i\gamma|\mathcal{A}|^2\mathcal{A}$ corresponds to SPM and the temporal derivative includes self-steepening and optical shock formation, while the integral describes the Raman response [32].

In the simulations presented in section 3.3.2 the attenuation coefficient is calculated as

$$\alpha = -\frac{\ln T}{L}, \tag{3.11}$$

where T is the transmission of the material at 1.03 μm and L is the length associated with that transmission. The value of α for each sample is presented in Tab.3.1a.

The dispersion coefficients are given by the relations [26, 33, 34]:

$$\begin{gathered} \beta_2(\lambda) = -\frac{\lambda^2}{2\pi c} D, \quad \beta_m(\lambda) = \frac{d\beta_{m-1}}{d\omega}, \\ D(\lambda) = -\frac{\lambda}{c}\frac{d^2 n_0}{d\lambda^2}, \end{gathered} \tag{3.12}$$

where ω is the frequency, λ the wavelength, and D the dispersion parameter. The calculation of these coefficients is performed using the calculators of the pyNLO package, where the calculation of n_0 is performed via the Sellmeier equations and coefficients for the different materials contained in an input file. The values of $(\beta_2, \beta_3, \beta_4)$, obtained with the code in appendix B, are presented in Tab.3.1b.

The nonlinear coefficient is given by the following expression [26, 34]:

$$\gamma = \frac{2\pi n_2}{\lambda_0 A_{eff}}, \tag{3.13}$$

where A_{eff} should be the fiber's effective mode area. The value of γ was adjusted to fit the experimental data. The expected area of the beam, A_{free}, both at the entrance and exit of each sample was calculated for each sample. Here we assume a perfect Gaussian beam and the absence of changes in the beam's caustic due to the sample (free propagation). These values were then compared to the A_{eff} associated with the adjusted value for γ, so that we can have an idea of how the interaction with the sample affected the caustic. A more detailed approach is presented in section 3.3.2.1.

As for Raman, a simplified model is used for the response function [35]:

$$h_R(t) = \frac{\tau_1^2 + \tau_2^2}{\tau_1 \tau_2^2} e^{-\frac{t}{\tau_2}} \sin\left(\frac{t}{\tau_1}\right). \tag{3.14}$$

Due to the lack of information of SRS for all materials the following values were used for all simulations: $f_R = 0.18$, $\tau_1 = 12.2$ fs and $\tau_2 = 32$ fs. These values correspond to a fused silica optical fiber [36].

The approach of using an equivalent fiber has already been demonstrated in the context of spectral broadening in a Multipass cell (MPC) by Daher *et al* [37]. In particular, in the case where the two mirrors of the MPC cause multiple passes in a bulk medium, the only correction concerning our model would be the an extra term of β_2 due to the Group delay dispersion (GDD) caused by the mirrors of the MPC. As the silver mirrors we use have low GDD and only perform one reflection each, unlike the ones of an MPC, our approach is still valid. However, the equation above is missing two key components of spectral broadening in solids: self-focusing and filamentation. This is because the limited energy input that fibers can handle does not normally allow for significant self-focus or filamentation, which might be in fact something to avoid inside a fiber. This is the major limitation of our simulations, although we can still use them to study the overall spectral broadening behavior.

3.3.2 Numerical values and results

3.3.2.1 Numerical values

We adjusted the value of γ to our experimental curves and calculated the associated value of A_{eff} by equation 3.13. This would give us an idea of the size of the beam inside the sample which we can compare to the expected transverse area of the beam, A_{free}, at the entrance and exit of the sample assuming that the sample does not change the beam caustic. For that, we need to know the variation of the beam radius with the position, w(z). As such we first had to calculate the beam waist w_0 and its position z_{ref} by measuring the transverse intensity of the beam with a camera. As the direct output of the *AMPHOS* laser was too wide to fit our camera we had to resize it, using a lens with a focal length of 350 mm, placed 54 cm after the output, followed by another lens, placed 17.5 cm after, and with a focal length of –200 mm. After this, the beam was sent to the camera to measure the beam radius[3] in multiple positions. The Gaussian beam radius is defined as the distance from the center of the beam where the intensity drops to $1/e^2$ of the max intensity.

The obtained data was then fitted by an ODR to the following expression for a perfect Gaussian beam:

$$w(z) = w_0\sqrt{1 + \left(\frac{\lambda(z - z_{ref})}{\pi w_0^2}\right)^2}. \tag{3.15}$$

In Fig.3.13 we present the result of this fit which allowed us to use a beam propagation software to trace the variation of both values of w, including the effect of the lenses, and thus recover the parameters of the laser output. Because the *AMPHOS* system could not be fully calibrated due to pandemic restrictions, its output exhibits a slight ellipticity and therefore we have two values for the beam radius at each propagation distance, w_x and w_y. We then proceed to calculate their variation until the sample, Fig.3.14.

---

[3] The radius was measured far away from the lenses because it was part of the preparation for a future experimental setup, which could not be placed closer due to spacial limitations.

Assuming that the beam forms an ellipse in the sample we can approximate the values of the beam's

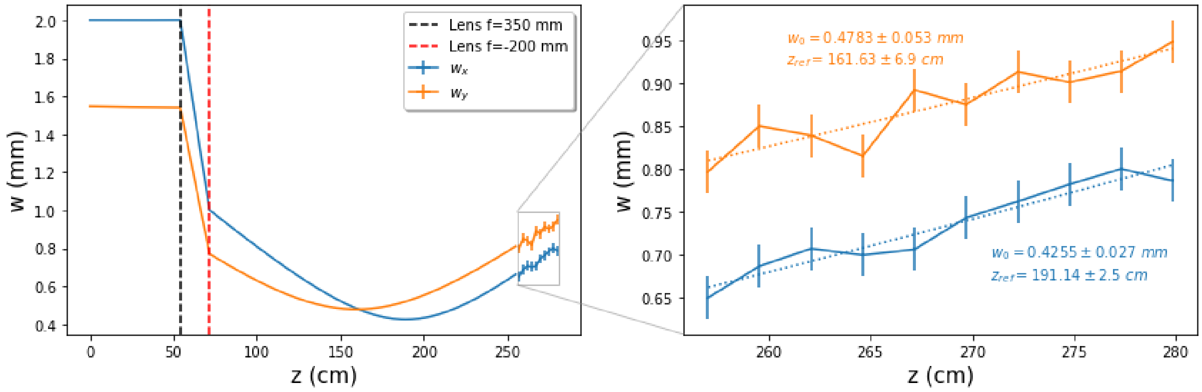

Figure 3.13: Reconstruction of the beam radius variation. On the right, we have a zoom in to the experimental data, together with the fit (dashed lines) to equation 3.15 and the resulting parameters w_0 and z_{ref}. These parameters were then used as an input to a propagation software to make the backward propagation of the beam through the lenses until the output of the *AMPHOS* laser, z = 0, which correspond to the continuous lines on the left side. The dashed lines in the left figure represent the position of the two lenses of focal length: f = 350 mm (black) and f = –200mm (red).

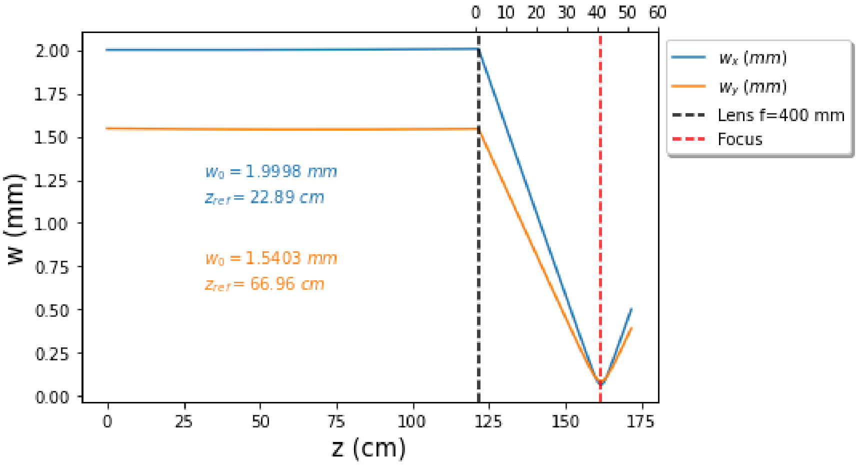

Figure 3.14: Variation of the beam radius until the sample, obtained with a propagation software. Here the values of w_0 and z_{ref} correspond to the laser's propagation parameters, obtained from the study presented in Fig.3.13. The dashed black line corresponds to the position of the f = 400 mm lens, while the red one marks the position of the focus, 400 mm away from the lens. The upper axes depicts the distance to the lens.

traversal area, assuming that the sample does not affect the caustic, by $A_{free} = \pi w_x w_y$.

The values of γ, A_{free} and A_{eff} are depicted in Tab.3.1c.

Table 3.1: Numerical values for simulation.

(a) Calculation of the attenuation coefficient α.

Sample	Transmission (%)	L (mm)	α (1/m)	Source
CaF_2	93.75	10.00	6.46	EKSMA[4]
Fused Silica	92.12	10.00	8.20	LASEROPTIK[5]
Sapphire	87.29	5.00	27.19	THORLABS[6]
YAG	86.16	3.00	49.65	LAYERTEC[7]

(b) Calculation of the dispersion coefficients.

Sample	β_2 (ps^2/km)	β_3 (10^{-2} ps^3/km)	β_4 (10^{-5} ps^4/km)	Propagation length (mm)	L_D (m)
CaF_2	18.49	2.03	-1.55	1	54.07
Fused Silica	18.97	4.12	-5.07	5	52.71
Sapphire	32.19	6.05	-6.77	15	31.06
YAG	66.68	6.74	-4.24	4	15.00

(c) Calculation of the nonlinear coefficient and transverse areas.

Sample	Distance to lens (mm)		A_{free} (mm^2)		n_2 (10^{-16} cm^2/W)	Simulations	
	Entrance	Exit	Entrance	Exit		γ (10^{-4} 1/W · km)	A_{eff} (mm^2)
CaF_2	450	451	0.168	0.174	1.71 [2]	40	0.026
Fused Silica	435	440	0.091	0.114	2.19 [2]	25	0.053
	450	455	0.168	0.199		7.96	0.168
	470	475	0.312	0.356		7.2	0.186
Sapphire	450	465	0.168	0.271	3.2 [38]	9	0.217
YAG	450	454	0.168	0.186	6.3 [2]	20.7	0.186

3.3.2.2 Results

The results of the simulations are presented in Fig.3.15, where in some cases the intensity is depicted in decibel, I_{dB}, such that:

$$I_{dB} = 10\log_{10}\left(\frac{I}{\max(I)}\right) = 10\log_{10}\left(\frac{|\mathcal{A}|^2}{\max(|\mathcal{A}|)^2}\right), \tag{3.16}$$

---

[4] https://eksmaoptics.com/optical-components/uv-and-ir-optics/calcium-fluoride-caf2-windows-530-6251/

[5] https://www.laseroptik.com/en/substrates/standard-substrates/fused-silica

[6] https://www.thorlabs.com/newgrouppage9.cfm?objectgroup_id=3982

[7] https://www.layertec.de/en/capabilities/substrates/materials/

where I is the spectrum with the highest number of counts in each one of the sub-figures of fig.3.12, and $\mathcal{A}$ is the complex envelope resulting from the propagation algorithm of pyNLO. On the left side of each figure, we compare the input spectrum (blue) with the output spectrum both through simulation (red) and experiment (green), on the top the spectra are presented in decibel while at the bottom the spectra are normalized such that the maximum is one. On the right, we present the spectral variation of the simulated pulse with the propagation distance. The plots with decibels were truncated at –20 dB, which corresponds to values 100 times smaller than the value at the peak.

Overall the simulations were able to replicate to a certain extent the observed spectra. In Table 3.13 we notice the A_{eff} in many cases is smaller than A_{free} at the entrance of the samples. This implies that the beam at some point suffered from self-focus inside these samples. The exceptions are the fused silica sample placed 450 mm after the lens, the sapphire sample, and the YAG sample. For the case of the fused silica, we have good agreement between when $A_{eff} = A_{free}^{Entrance}$, but this still points to a self-focus. In the absence of self-focus, we should obtain that $A_{free}^{Entrance} < A_{eff} < A_{free}^{Exit}$, since the beam would be diverging. So in this case the natural divergence of the beam must have counteracted the self-focus, which was our objective when placing the samples after the focus, in order to prevent optical damage. In the case of the sapphire as the $A_{free}^{Entrance} < A_{eff} < A_{free}^{Exit}$ we cannot guaranty that the beam self-focused but we cannot exclude the possibility either. For YAG we used $A_{eff} = A_{free}^{Exit}$ as a limit since it would not make sense for the beam to become larger than that. But if we used a higher value that would lead to a smaller broadening while a smaller value would lead to the formation of more peaks, which are already forming in our simulation. A possibility is that the broadening generated in these samples was strongly related to the formation of free electrons and the consequent self-steepening, which is not included in equation 3.10.

In order to test the effect of each of the terms from equation 3.10, we turned off each term separately, either by setting the α, β_m, and γ to zero or by disabling SRS and self-steepening in the pyNLO package. Unsurprisingly the absence of dispersion and/or SRS did not produce any effect on the final spectrum. These two processes only become significant, at least without being combined with other processes, when the propagation length is above the dispersion length [26]. And as we can see in Table 3.1b the propagation length is many orders of magnitude below L_D.

Disabling self-steepening also did not visibly change the spectrum, which was expected as none of the final simulated spectra presents any kind of asymmetry, cf. Fig.3.15. The self steepening described by the derivative in equation 3.10 results only from Kerr effects, but since it is not enough to explain the asymmetry observed in the experimental data, even for a lower effective area, it is possible that the self-steepening also resulted from a large electronic density.

The only visible changes were a consequence of either changing the value of α or γ. In the case in which

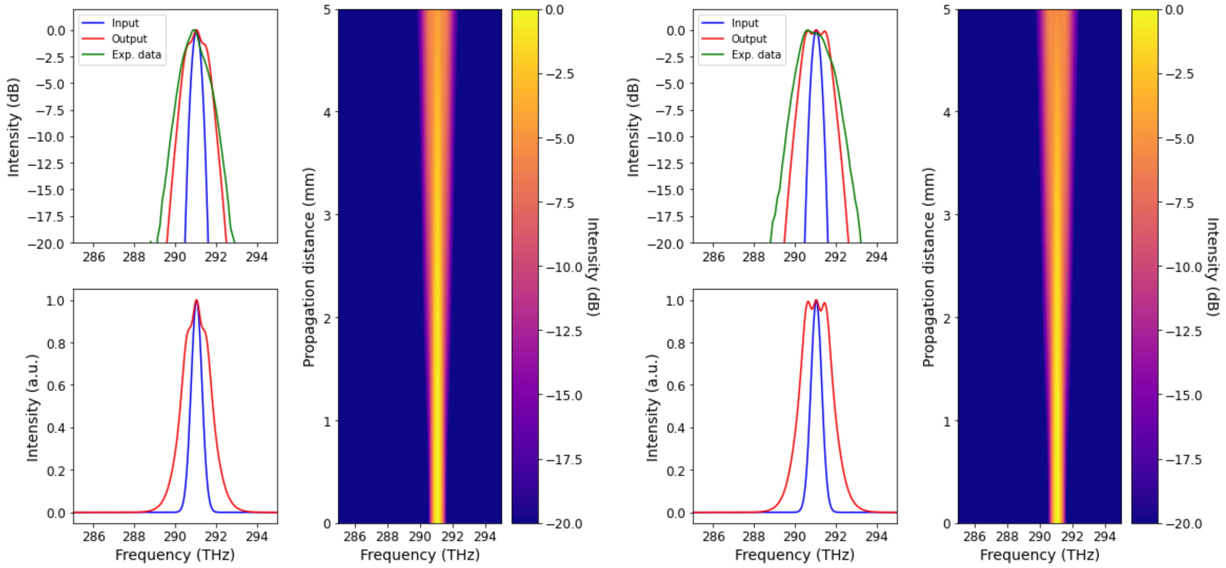

(a) Fused silica sample 47 cm away from the lens.

(b) Fused silica sample 45 cm away from the lens.

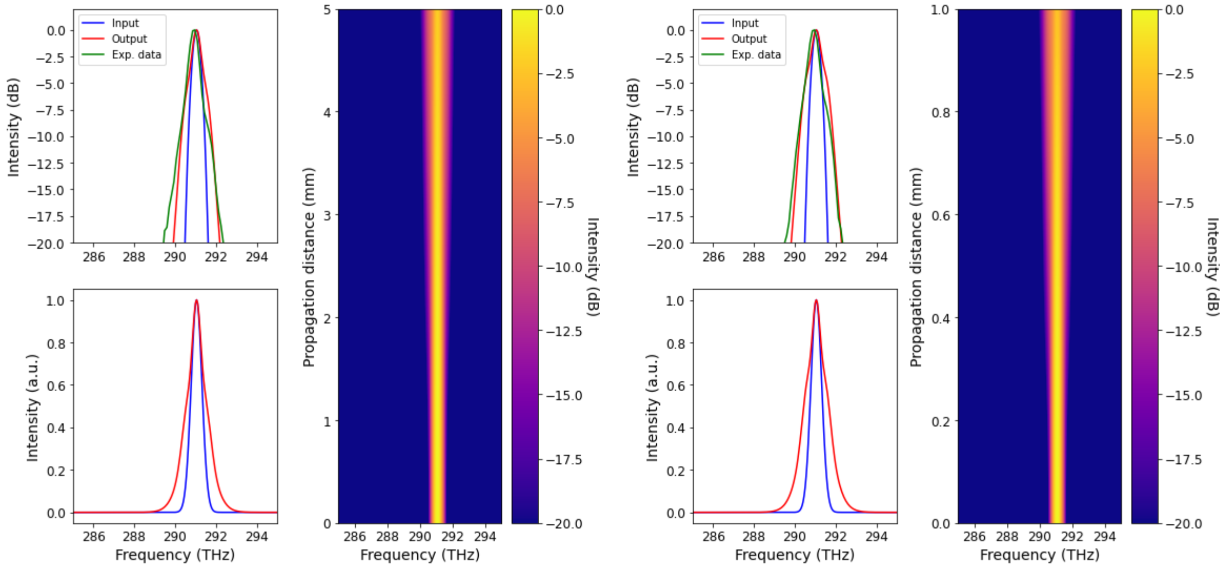

(c) Fused silica sample 43.5 cm away from the lens.

(d) CaF_2 sample

Figure 3.15: Simulation of spectral broadening at 1.03μm. Each experimental spectrum corresponds to the highest energy for each sub-figure in Fig.3.12, with the exception of Fig.3.12c where we took the 20% spectrum (before damage). On the left is the comparison of the numerical input and output pulse together with the experimental data. On the right is the numerical spectral variation with propagation. The curves were truncated at –20 dB.

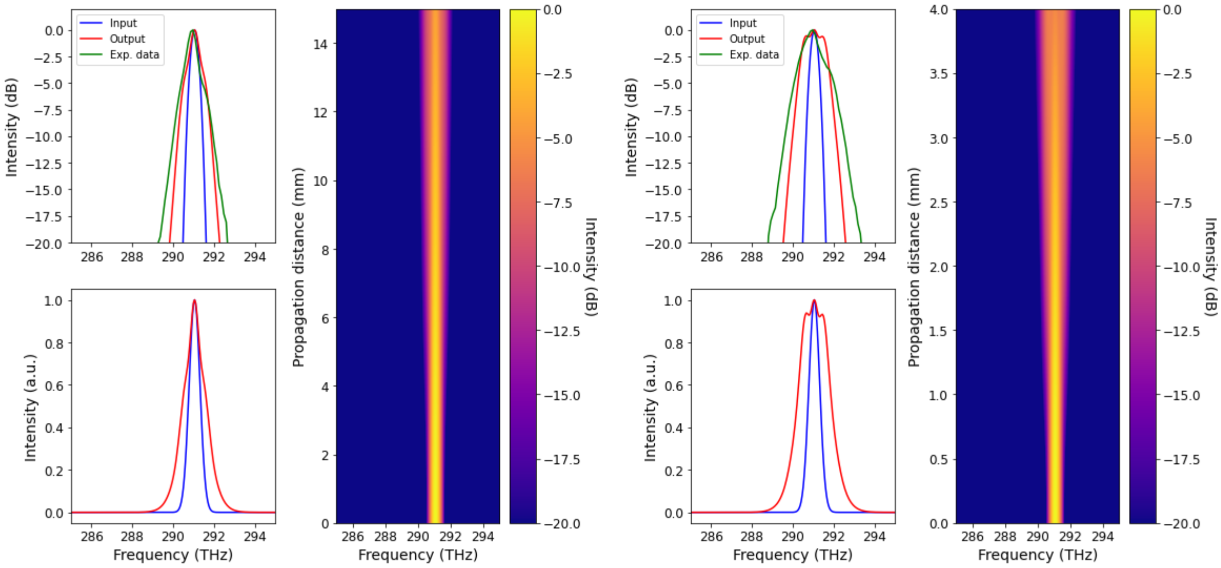

(e) Sapphire sample.

(f) YAG sample.

Figure 3.15: Simulation of spectral broadening at 1.03µm. Each experimental spectrum corresponds to the highest energy for each sub-figure in Fig.3.12, with the exception of Fig.3.12c where we took the 20% spectrum (before damage). On the left is the comparison of the numerical input and output pulse together with the experimental data. On the right is the numerical spectral variation with propagation. The curves were truncated at –20 dB. (cont.)

we disregard losses ($\alpha = 0$), the final spectra possess slightly larger broadening, however, we observed the formation of more peaks around the central frequency. The change of γ produced the most drastic spectral results, but even in these conditions self-steepening did not contribute to the spectrum. As such the main contribution for the spectral broadening is indeed the nonlinear effects. The simulations seem to indicate that the main mechanism would be SPM, but this does not explain the high asymmetry presented by the spectra.

In conclusion, the simulations imply that the observed spectral broadening results from SPM. Where in many cases the beam self-focused inside the media with the generation of free electrons that contribute to a strong self-steepening. This points to the formation of filaments inside of our samples, which in the case of fused silica is supported by the segmented optical damage that was observed.

4

High-Harmonic Generation

Contents

4.1 Physical Principles 39
  4.1.1 Perturbative Harmonic generation 39
  4.1.2 High-Harmonic Generation in gases (atomic) 41
  4.1.3 High-Harmonic Generation in solids 44
4.2 Experimental Work 46
  4.2.1 Setup 47
  4.2.2 Methods and Results 48
4.3 Simulation in literature 63

Under certain conditions, a high-intensity laser pulse propagating in a nonlinear medium can generate a new wave with a different frequency that is multiple (or harmonic) of the input one.

The most common way of producing harmonics is the multiple absorption of photons, which is a perturbative process related to the nonlinear response of the polarization inside the medium.

Another phenomenon characterized by this is High-Harmonic Generation (HHG), where the output takes the form of a train of short chirped pulses, one for each half-cycle of the input pulse. The pulses can have durations down to attoseconds and in some cases with a spectrum containing thousands of harmonics, forming a supercontinuum. These pulses form the basis of attosecond science [18].

In this chapter we present the results of harmonic generation in a multitude of materials, comparing the results with previous observations in literature. We also present a Fourier analysis of some spectra, to test the possibility of formation of multiple components of third harmonic, and a efficiency study of the harmonic generation. Finally, we present a short comment on some of the methodologies to simulate harmonic generation.

4.1 Physical Principles

4.1.1 Perturbative Harmonic generation

In section 3.1.1 we used a simplified description of the polarization, P, for the explanation of the Kerr effect in the refractive index, see Eq.3.3. A more generalized form is given by the perturbative relation [20]

$$P = \varepsilon_0 \left[\chi^{(1)}E + \chi^{(2)}E^2 + \chi^{(3)}E^3 + ...\right], \tag{4.1}$$

where $\chi^{(1)}$ is the linear susceptibility and $\chi^{(n)}$, $n > 1$ is the nth-order nonlinear susceptibility. This equation was written with scalars for simplicity and brevity but it can also be written using the vectorial nature of E and P [20]. In such case $\chi^{(1)}$ becomes a second-rank tensor, $\chi^{(2)}$ a third-rank tensor, and so on. Each of these susceptibilities leads to different physical phenomena. For example, one of the consequences of $\chi^{(2)}$ is Second Harmonic Generation (SHG), Fig. 4.1, where two photons of the input beam, at frequency ω, cause an excitation to a virtual level that leads to the spontaneous emission of a single photon at frequency 2ω in a single quantum process. In the same way, $\chi^{(3)}$ allows for three photons to participate in the excitation leading to the emission of third-order harmonics, also known as Third Harmonic Generation (THG). And so on for all the higher values of n.

Because these processes are perturbative, unlike HHG, the efficiency of the harmonics drops significantly with each order. For example, the calculated values of $\chi^{(2)}$ and $\chi^{(3)}$, using the typical characteristics of most condensed matter, are around 6.9×10^{-12} m/V and 344×10^{-24} m^2/V^2 [20].

Although the quadratic term should be much larger than the cubic one, in reality the simplified expression of equation 3.3 is enough to describe many interactions. The reason is that all even-order values of $\chi^{(n)}$ are equal to zero in a centrosymmetric medium, which includes isotropic media and 11 of the 32 crystal classes [20]. This can be understood by looking to the nth-order polarization, $P^{(n)}$,

$$P^{(n)} = \varepsilon_0 \chi^{(n)} E^n. \tag{4.2}$$

Saying that a medium is centrosymmetric is like saying that it possesses an inversion symmetry. This symmetry imposes that if the direction of the electric field reverses so must the polarization

$$\begin{aligned} -P^{(n)} &= \varepsilon_0 \chi^{(n)} (-E)^n \\ &= \varepsilon_0 \chi^{(n)} (-1)^n E^n \\ &= (-1)^n P^{(n)}. \end{aligned} \tag{4.3}$$

As one can easily see from equation 4.3, when n is even the polarization must be zero, which implies that $\chi^{(n)} = 0$. As such, as long as the medium is centrosymmetric it is impossible to observe even-order phenomena such as even harmonic generation.

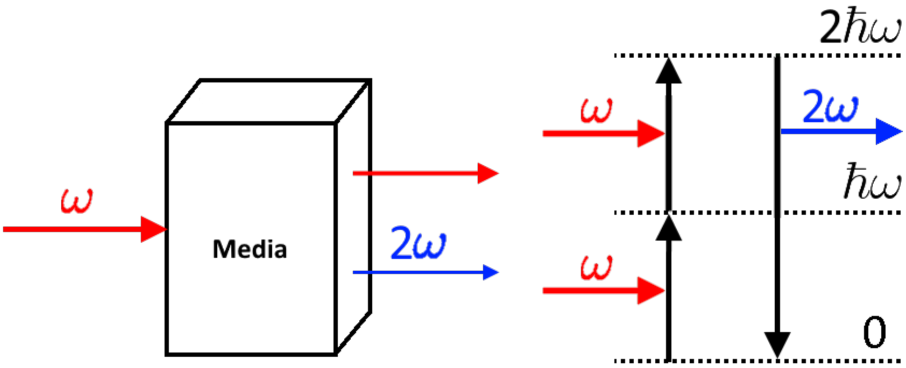

Figure 4.1: Schematic of SHG. Left: macroscopic view in which the input beam (red; ω) interact with a nonlinear media, resulting in the formation of a new beam with twice the frequency of the input known as the Second Harmonic (blue; 2ω). Right: band structure of this process where two input photons excite in quick succession the material to a virtual level which then leads to the emission of a single Second Harmonic photon by spontaneous emission.

4.1.2 High-Harmonic Generation in gases (atomic)

In the case of low-frequency lasers, the theory behind HHG in gases can be reduced to a very simple semi-classical model, first introduced by Corkum in 1993 [39], known as three-step recollisional model, Fig. 4.2.

In this model, the gas atom is taken as a potential well, with a single electron, under the influence of a monochromatic, linearly polarized electric field. This field oscillates with an amplitude E_0, frequency ω_0 (period $T = 2\pi/\omega_0$), and a photon energy $\hbar\omega_0$ much smaller than the ionization potential of the atom, I_p, so that normal absorption does not occur (low-frequency laser).

For explanation purposes, let us start from a state in which the electric field is zero and is about to be accelerated in the +x direction, $E > 0$. HHG will then arise from the following steps [14, 40]:

1. **Tunneling:** As the amplitude of the electric fields increases the potential well will tilt, due to the extra potential added. At some point, this will form a potential barrier giving the electron the chance to tunnel through and escape the atom at zero velocity. The time of escape, t_i, is therefore variable from atom to atom and from cycle to cycle since the tunneling is a probabilistic event.
2. **Acceleration:** The now free electron is accelerated away from the ionized atom. As the electric field reverses, at half-cycle, the electron will now be accelerated towards the parent ion. Upon arrival at the atom, the electron possesses kinetic energy E_k.
3. **Recombination:** If the electron collides with the parent ion, at time t_r, it recombines emitting a photon. This photon possesses an energy $\hbar\omega = I_p + E_k$.

This process is repeated at each cycle. However, since the first step only relies on the absolute value of the electric field being enough to allow tunneling, the same steps can be initiated as the electric field becomes negative and the electron is accelerated in the –x direction. Since this system is symmetric the likelihood of this case is the same as of the acceleration in +x. Therefore, in a gas, we will observe the emission of a short-pulse, in some cases down to the attosecond, at each half-cycle of the laser, forming a train of short-pulses with a period of T/2 (Fig.4.3). By applying the Fourier transform to this train we obtain a spectrum in the form of a series of delta functions (frequency comb) spaced as

$$\omega_n = \omega_0 + 2n\omega_0, \ n \in \mathbb{N} \tag{4.4}$$

(carrier offset frequency of ω_0 and a comb tooth spacing equal to $2\omega_0$). As such in the gas the symmetry only allows the generation of odd harmonics. This Fourier approach might look synthetic, physically speaking all frequencies can be generated in this process. However, due to the constriction that the new photons are generated at each peak of the fundamental in the same direction/polarization of the fundamental, only waves that are odd harmonics of the fundamental can add constructively. Let us

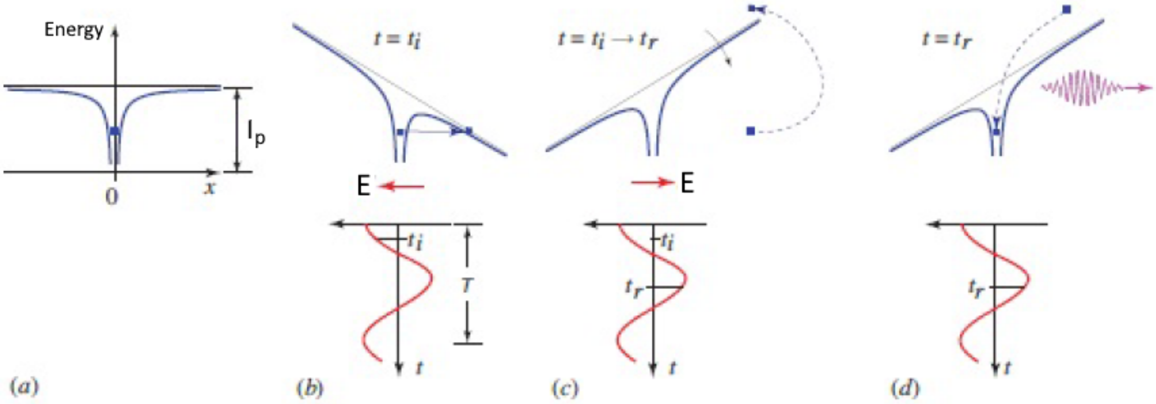
Energy
I_p
0
x
$t = t_i$
E
t_i
T
t
$t = t_i \rightarrow t_r$
E
t_i
t_r
t
$t = t_r$
t_r
t
(a)
(b)
(c)
(d)

Figure 4.2: Three-step recolisional model. **(a)** A gas atom is modeled as a single electron in the ground state of a potential well with ionization energy I_p. **(b)** An applied optical field E(t) from an exciting laser alters the potential well and causes the electron to tunnel into free space at time t_i. **(c)** The free electron is accelerated in the +x direction by the negative optical field but reverses direction when the optical field becomes positive, returning back to the ionized atom with increased kinetic energy E_k at time t_r. **(d)** The electron recombines with the ion and radiates photons of energy $I_p + E_k$ that takes the form of a chirped pulse of radiation with sub-femtosecond structure. Adapted from [14].

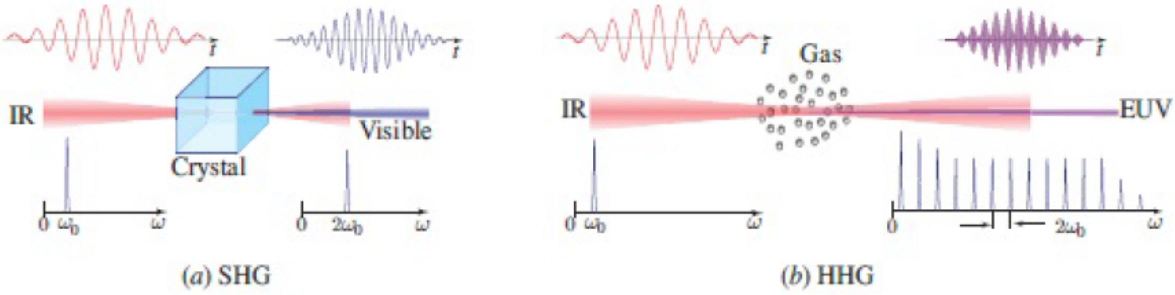
t
t
IR
Crystal
Visible
0
ω_0
ω
0
$2\omega_0$
ω
t
Gas
t
IR
EUV
0
ω_0
ω
0
$2\omega_0$
ω

(a) SHG

(b) HHG

Figure 4.3: Comparison between **(a)** emission of visible light by SHG and **(b)** emission of extreme UV by HHG. In **(b)** note the formation of train of sub-femtosecond pulses, one for each half-cycle of the exciting IR field, together with the spectrum consisting of a frequency comb with a tooth spacing $2\omega_0$. Taken from [14].

imagine an even harmonic that is generated at time $t_0 = 0$ and therefore has a maximum/minimum at that time. Since it is an even harmonic it has a period of $T_{even} = T/2n$ and so after $t_1 = T/2$ (a multiple of T_{even}) the harmonic is in the same state as in t_0. But at t_1 the fundamental is in the opposite direction, generating the same harmonic but out of phase, thus adding destructively with the harmonic generated at t_0. In the case of an odd harmonic of period $T_{odd} = T/(2n+1)$, generated at t_0, after a time t_1 the harmonic will be pointing in the same direction of the fundamental field (as $T/2 = (n+1/2)T_{odd}$) and adding constructively.

Also because the energy of each photon, generated at t_r, depends on the energy E_k of the electron and both E_k and t_r depend on at which time t_i the electron originally tunneled, the final pulse will have a different instantaneous frequency at each time, meaning that the generated pulses are chirped [14].

Equation 4.4 describes the spectrum as an infinite number of delta functions, however what is observed experimentally is the existence of a *plateu* followed by a cut-off (Fig. 4.4). This cut-off is given by [39]

$$\hbar\omega_{max} = I_p + 3.17U_p,$$
$$U_p = \frac{e^2E_0^2}{4m\omega_0^2} = \frac{e^2E_0^2\lambda_0^2}{16\pi^2mc^2}, \tag{4.5}$$

where e and m are, respectively, the charge and the mass of the electron, and U_p is the ponderomotive

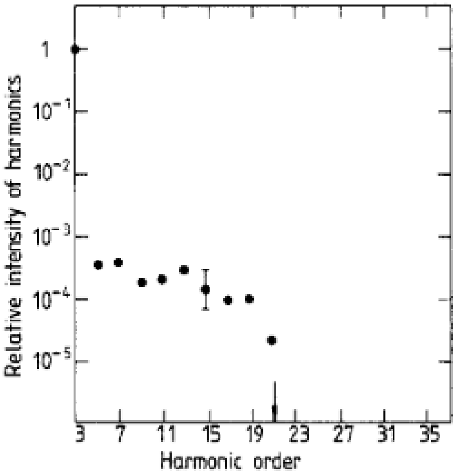

Figure 4.4: Relative intensity of the harmonics generated in Xe gas. Taken from [13].

potential, which corresponds to the mean kinetic energy acquired by the electron. From this equation, we see that the cut-off increases with the square of both the electric field and the wavelength. This model relies on three basic assumptions about the electrons that participate in HHG: (i) they return to the parent ion, (ii) they tunnel with zero velocity, and (iii) upon the return they have the appropriate kinetic energy to produce a harmonic. Lewenstein *et al* [41] performed a full quantum-mechanical analysis without assuming the initial position or velocity of the electron after tunneling. They concluded that the dominating contribution for HHG is precisely the electrons that fill these criteria. Additionally, by numerical simulation, they arrived at a correction of equation 4.5,

$$\hbar\omega_{max} = 1.32I_p + 3.17U_p, \tag{4.6}$$

However, this equation is obtained in a regime where $U_p \gg I_p$ and therefore this correction is, for most applications, negligible. As such the semi-classical model, even though quite simplistic, is capable of depicting the complicated quantum phenomena of HHG in gases, with linearly polarized electric fields, with remarkable accuracy.

4.1.3 High-Harmonic Generation in solids

In the very first observation of HHG in solids by Ghimire *et al* [17] they obtained up to the 25th harmonic in ZnO crystal, with a spectrum consisting in a *plateau* of harmonics followed by a cut-off. This was proof that they were observing high-harmonics and not perturbative harmonics; however, as they were studying the dependence of the cut-off on the magnitude of the electric field, E_0, they concluded that the cut-off grew linearly with E_0 instead of quadratically as observed in gases (Eq.4.5). They found that the HHG process was much less sensitive to polarization than the atomic case, to such an extent that the process only effectively turned off when the polarization was circular. Additionally, depending on the orientation of the crystal they were capable of generating either odd-harmonics or a combination of odd and even-harmonics as a consequence of breaking the symmetry in the system, something never observed in gases. Therefore their experiments suggested that HHG in solid media does not result from the same processes as in gases.

One of the main differences in these two regimes is the density: while in a gas the atoms are separated enough for the system to be reduced to a single potential well, in solids the atoms are far too close to each other for such an approximation. In solid-state materials the high density generally implies an overlap of neighbouring atomic orbitals, resulting in the formation of energy bands, in particular, the valence and conduction bands. The most accepted theory is that the generation of high-harmonics in solid-state results from a similar process to the three-step recollisional model [42–44] (see Fig. 4.5):

1. **Tunneling:** The electric field induces a polarization in the material allowing an electron from the highest valence band to tunnel into the lowest conduction band forming an electron-hole pair. Note that in this case the hole can not be taken as motionless as we did with the ion in gas-based HHG.
2. **Intraband-current:** The electron (hole) is then accelerated in the conduction (valence) band in the opposite direction of its pair, leading to the formation of intraband currents. For the larger amplitudes near the center of the pulse, the electrons collide with the boundary of the Brillouin zone and Bragg scatter to the next zone, where their momentum is in the opposite direction leading to

periodic motions. This is known as Bloch Oscillations (BO)[1] [45]. As a consequence, the intraband currents oscillate much more than the electric field, which leads to a strong radiation [44]. That radiation can then add constructively and form the harmonics as described previously, this is known as **intraband mechanism** [46], which has no analogous in atomic HHG.

3. **Recombination:** If the electron reencounters the hole, it can recombine, emitting a photon with energy depending on the wave vector at the time of recombination. This is known as the **interband mechanism**, which is analogous to HHG in gases. However, one cannot separate the two mechanisms as the intraband current strongly affects the polarization at the time of recombination. Additionally, unlike in gas HHG, where the electron recombines with the parent ion, in solid-state due to BO the electron can recombine with nearest holes (ions).

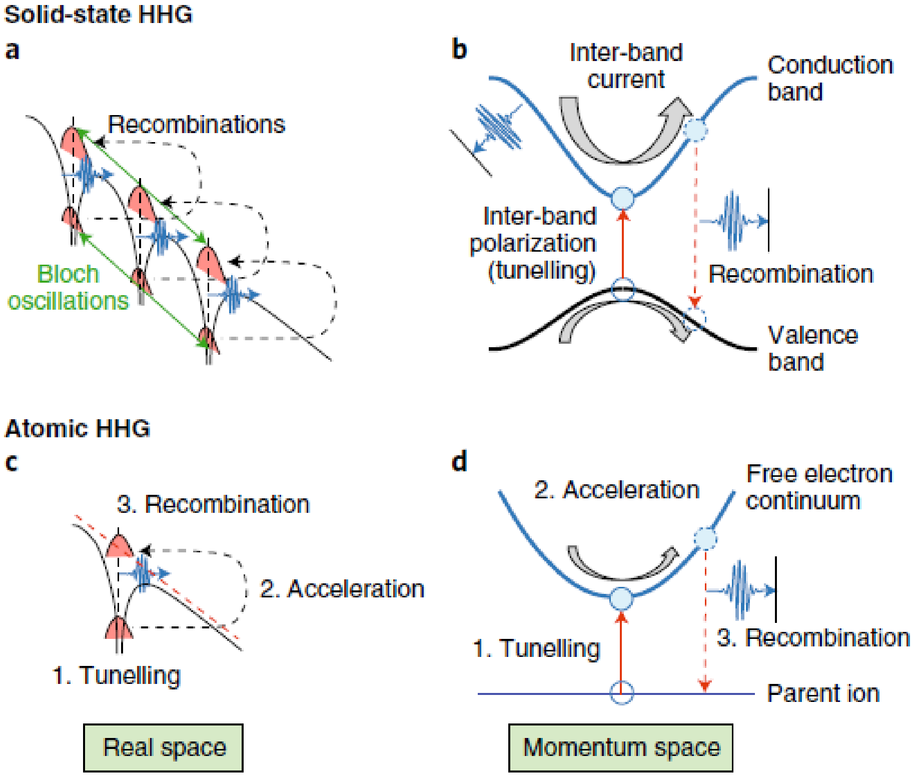
Solid-state HHG
a
Recombinations
Bloch oscillations
b
Inter-band current
Conduction band
Inter-band polarization (tunelling)
Recombination
Valence band
Atomic HHG
c
3. Recombination
2. Acceleration
1. Tunelling
d
2. Acceleration
Free electron continuum
1. Tunelling
3. Recombination
Parent ion
Real space
Momentum space

Figure 4.5: **a**- The driven electron could scatter from the periodic Coulomb potential termed as Bloch Oscillations, recombine with the associated hole (ion) and recollide with the first- and second-nearest holes (ions); **b**- The momentum-space version of a, showing intraband Bloch oscillations in the conduction band and interband coupling between the valence and conduction band, both emitting high-frequency radiation in the forward direction; **c**- Schematic diagram of the three-step recollision model comprising tunnel ionization, free acceleration and recombination; **d**- The momentum-space version of c, where the electron tunnels from the bound state to the continuum state, accelerates in the parabolic continuum band and then recombines to the bound state (parent ion) emitting high-frequency radiation. Taken from [17].

---

[1] In all correctness BO arise in the presence of a constant electric field, however, we can define an instantaneous Bloch frequency for the instantaneous electric field [44].

The question of what mechanism dominates HHG in solids remains an open discussion. According to Vampa *et al* [43] the dominant mechanism in the plateau for most of their simulations is the interband current, while intraband interferes more in the perturbative part of the spectrum. However, recently Liu *et al* [46] suggested that for fields high enough two plateaus will be formed, a first plateau formed by the recollision and a second plateau at higher frequencies induced by BO electrons.

Regardless, although this model has some similarities to HHG in gases the consequences of this double mechanism bear some striking differences. As mentioned the cut-off of the harmonics grows linearly with the applied field instead of quadratically. The response to wavelength also differs as it affects the interband and intraband harmonics differently and in a particularly complex way [43]. Solids have also been demonstrated to be quite resistant to variation to polarization demonstrating strong signals and ellipticity levels that would extinguish completely HHG in gases. This is because in solids the electron can recombine in one of the neighbours of the parent ion, while in the gases the electron must recollide with the parent ion requiring an electric field as linearly polarized as possible. Finally, if the material breaks the inversion symmetry it is possible to observe even-harmonics.

Because the absorption of solid materials for high frequencies is much higher than in gases, the maximum harmonics recorded in gases (> 5000) in much larger than the corresponding one in solids (~ 25). However, the gas-based geometries involve expensive and complex setups including amplified femtosecond lasers, vacuum pumps, means to confine the gas, and delicate optics for beam manipulations [42], making them extremely hard to assemble and replicate when compared to the solid-based ones. This makes solid-state HHG a simple, compact, and affordable alternative for the generation of attosecond pulses.

4.2 Experimental Work

Before jumping into the experimental results there are some disclaimers on the following data. The purpose of this thesis is just a proof of concept of the capabilities and potential of the new laser at L2I.

Although we might use the known structure of the materials to justify some of our observations, this is not a study of that structure. So much that the crystals used for HHG are normally custom made to guarantee phase matching and possess a thickness of the order of a few microns[2], while in our case we use standard transmission windows, none thinner than 1 mm, and sometimes not even of a pure substance but instead with some doping.

Finally, our samples either were isotropic (fused silica), had a cubic structure of class m3m (CaF_2, LiF, YAG) or trigonal of class $\bar{3}$m (Sapphire). All of these are centrosymmetric, meaning that it is much less probable to observe even harmonics [20]. In principle all m3m samples should have been cut at the $< 100 >$ plane.

---

[2] In solids many times, due to the strong absorption, the observed harmonics are formed in the last nanometers of the crystal and it is preferable to have thin crystals to avoid self-action effects.

4.2.1 Setup

The two setups for harmonic generation (Fig. 4.6) are similar to those presented for SCG at 3 μm, section 3.2.1. Except that instead of using an integrating sphere we use a UV optical fiber, mounted on a translator, to collect each harmonic individually and send them to a spectrometer (*FLEX-STD-UV-Vis-NIR*, *SARSPEC*).

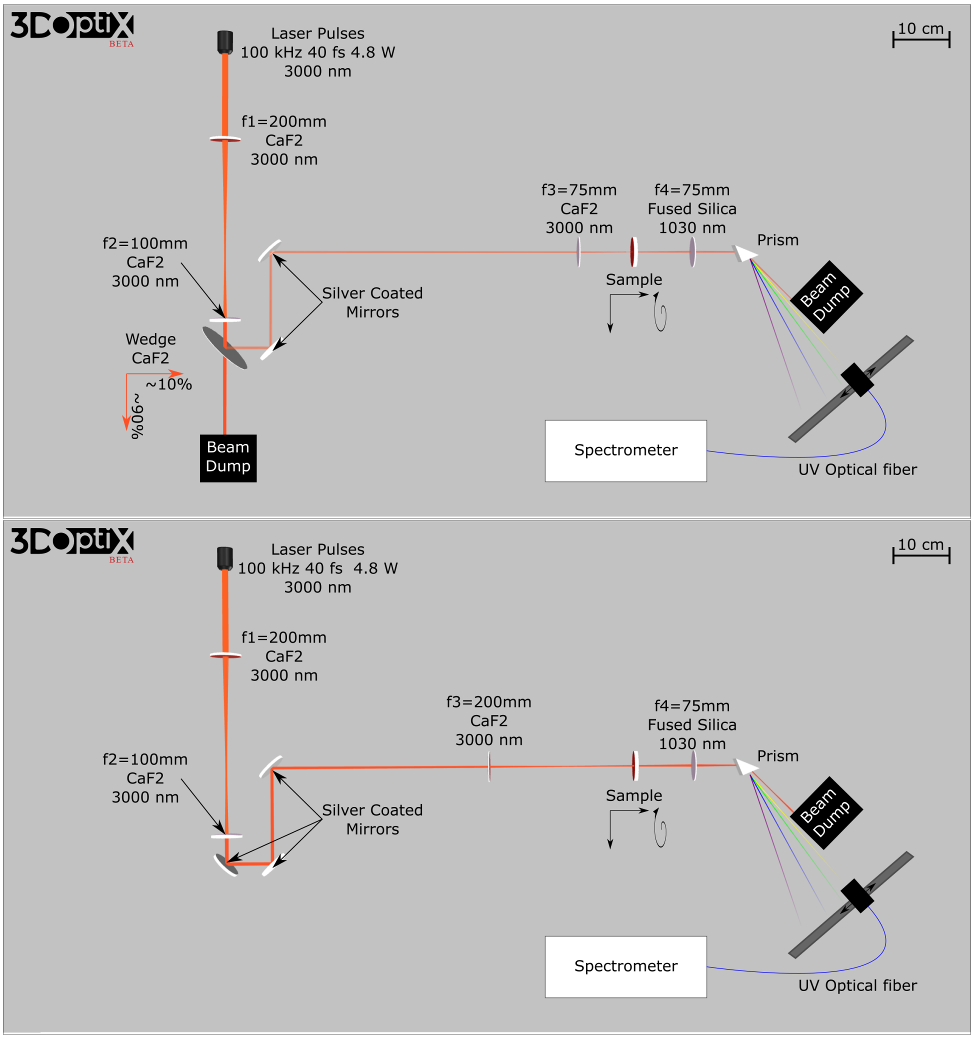
3DOptix BETA
Laser Pulses
100 kHz 40 fs 4.8 W
3000 nm
10 cm
f1=200mm
CaF2
3000 nm
f3=75mm
CaF2
3000 nm
f4=75mm
Fused Silica
1030 nm
Prism
f2=100mm
CaF2
3000 nm
Silver Coated
Mirrors
Sample
Beam
Dump
Wedge
CaF2
~10%
~90%
Beam
Dump
Spectrometer
UV Optical fiber
3DOptix BETA
Laser Pulses
100 kHz 40 fs 4.8 W
3000 nm
10 cm
f1=200mm
CaF2
3000 nm
f3=200mm
CaF2
3000 nm
f4=75mm
Fused Silica
1030 nm
Prism
f2=100mm
CaF2
3000 nm
Silver Coated
Mirrors
Sample
Beam
Dump
Spectrometer
UV Optical fiber

Figure 4.6: Experimental setup for the acquisition of harmonics. Top: setup with 10% of the output power using a wedge. Bottom: setup with the full power.

4.2.2 Methods and Results

We acquired harmonics for multiple materials. In the case of the low-power setup, the samples were placed at the focus, while in the high-power setup they were placed slightly after the focus with the aid of the translation stage, as the energy was high enough to damage the samples.

Regardless, the procedure was similar for each sample. By moving the translator, we search for any individual harmonics with the spectrometer. When we locate a harmonic we use the rotation mount to rotate the samples around their axis[3] and the spectrum is taken in intervals, in most cases, of 10° until covering the entire 360° range. The process is then repeated for each available harmonic and the sample is switched.

For each harmonic the spectrum is fitted by an ODR to a Gaussian function:

$$C(\lambda) = \frac{C_0}{\sigma\sqrt{2\pi}} \exp\left(-\frac{1}{2}\frac{(\lambda-\mu)^2}{\sigma^2}\right), \tag{4.7}$$

where $C(\lambda)$ is the number of counts as a function of the wavelength, C_0 the normalization constant, μ the expected value, and σ the variance. As C_0 is proportional to the energy of the harmonic, its variation with the orientation is studied in the form of polar plots where the radius is the value of C_0 normalized to each harmonic. To verify the accuracy of this fit, we also present the similar polar plot for area beneath the harmonic defined as $\int_{\lambda_1}^{\lambda_2} C(\lambda)\, d\lambda$, where λ_1 and λ_2 are, respectively, the lowest and the highest wavelength in which $C(\lambda_{1,2}) = \max\{C(\lambda)\}/e^2,\ \lambda_2 > \lambda_1$. In some cases we had to remove some outliers and points where the uncertainty was too high to accept the measured values.

For each sample, we present two overviews of the obtained harmonics. In both cases, we use the spectrum with the highest number of counts and the wavelengths are multiplied by the expected harmonic order and compared with the fundamental[4]. While in one case the harmonics are presented normalized to verify the spectrum shape, in the other the spectrum is divided by the spectrometer's acquisition time for that specific spectrum. The latter allows calculating the rate of counts to each harmonic, which can later be associated with the power of said harmonic.

A final note before going into the experiments themselves is a question of notation, in many graphics, we use the following notation to distinguish between the two possible setups (Fig. 4.6):

W - Stands for the low-power setup using the Wedge.

M - Stands for the high-power setup using the Mirror.

---

[3] The beam was not focused in the center of the sample to avoid the overexposure of a single spot. The orientation of the crystals should be the same at each point however the experiment becomes susceptible to any in-homogeneity in the material.

[4] Due to some coupling problems at the entrance of our spectrometer this spectrum is quite noisy and may not match perfectly the real fundamental spectrum in terms of intensity. However, it should be enough to verify the bandwidth of the input spectrum.

4.2.2.1 Calcium fluoride samples

Calcium fluoride demonstrates a low absorption and a high damage threshold, with a transmission ranging from 200 nm to 8000 nm making it an ideal material for the propagation of low-energy, high-frequency waves such as the harmonics. In our case, we use two doped samples, one of UV grade (1 mm thick) and another IR grade (3 mm).

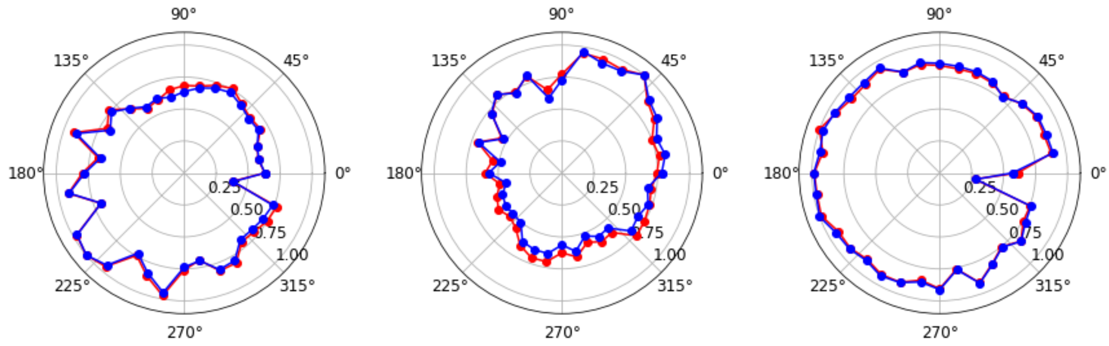

(a) W-3rd harmonic. **(b)** W-5th harmonic. **(c)** M-3rd harmonic.

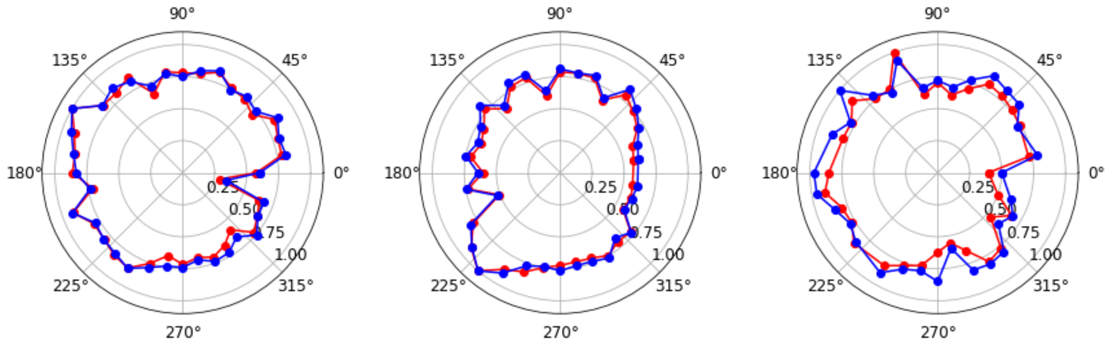

(d) M-5th harmonic. **(e)** M-7th harmonic. **(f)** W-9th harmonic.

Figure 4.7: Polar plots for the 1 mm CaF$_2$ sample placed at focus. The radius corresponds to the normalized area beneath the curve. In red calculated by a Gaussian fit and in blue by a numerical integration within 1/e^2 of the maximum number of counts. **W** stands for the low-power using a wedge setup while **M** stands for the high-power setup using a mirror.

In the case of the 1 mm sample we started by acquiring with the low-power setup. Figs. 4.7a and 4.7b show the acquired data. The polar plot does not present any kind of obvious dependence. The small variation observed can be associated with noise. After that[5], we performed the measurements of the harmonics in the high power-setup, reaching up to the 9th harmonic. The results are shown in Figs. 4.7c-4.7f. For these experiments the sample was placed 24.2 cm away from the 200 mm focusing lens.

---

[5] Bear in mind that the experiments with the low-power and high-power setup were performed at different times running all the different samples. Additionally, the samples do not possess any kind of marking that would allow to place the sample in the exact same orientation so the 0º of the low and high-power power setups do not necessarily match.

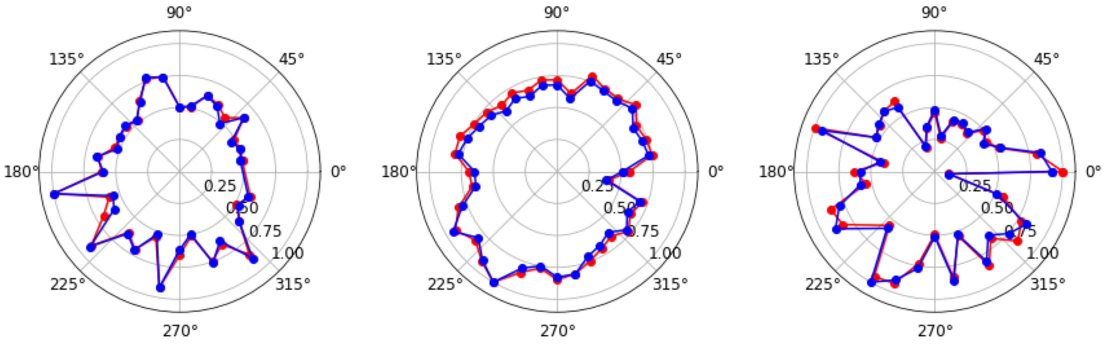

(g) W-9th harmonic closer to focus. **(h)** M-unknown near the 3rd harmonic. **(i)** M-unknown near the 5th harmonic.

Figure 4.7: Polar plots for the 1 mm CaF$_2$ sample placed at focus. The radius corresponds to the normalized area beneath the curve. In red calculated by a Gaussian fit and in blue by a numerical integration within 1/e^2 of the maximum number of counts. **W** stands for the low-power using a wedge setup while **M** stands for the high-power setup using a mirror. (cont.)

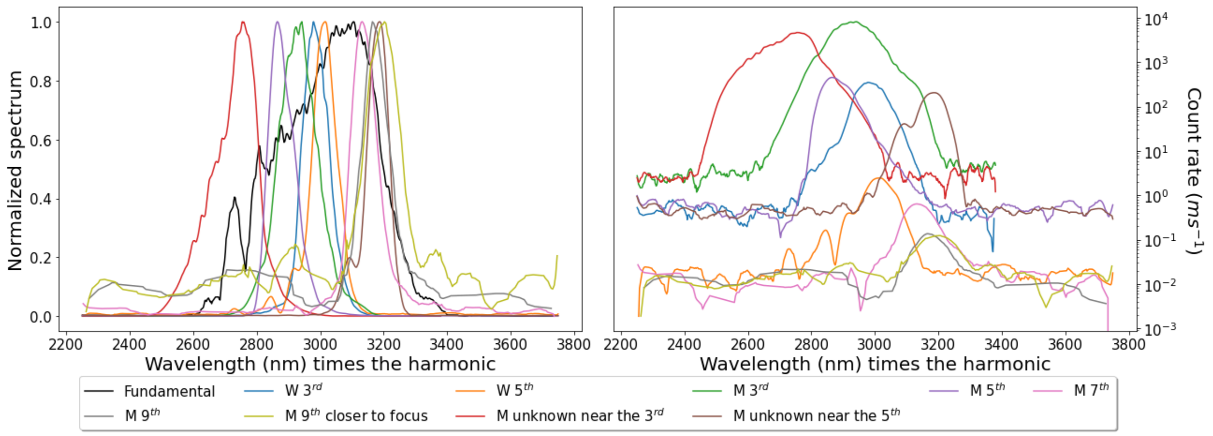

Figure 4.8: Smoothed spectra of all harmonics obtained with a CaF$_2$ sample of 1 mm. Each spectrum corresponds to the angle with the highest count rate and are centered around the fundamental. On the left all spectra were normalized, while on the right we present the count rate of each spectrum.

Once again we observed a lack of dependence on the angle. However, with the high power we observed that the 3rd and 5th harmonics were accompanied by an unknown peak (Figs. 4.7h and 4.7i), although with the same lack of angular dependence. Finally we tried to move the sample 1 mm closer to the focus having obtained the 9th harmonic before damaging the sample, Fig. 4.7g. A selection of spectra for each harmonic is presented in Fig. 4.8.

For the 3 mm sample we could only obtain harmonics in the low-power setup as the high-power led to SCG, Fig. 3.9a. We started by measuring the peak in the expected position of the 3rd harmonic, Fig. 4.9a, and noticed a small peak at lower wavelength that seemed to have an opposite behaviour with the variation of the angle. The fiber coupling was then moved to a position in which we could measure both peaks simultaneously. Using this data, we studied the angular dependence of both, Fig. 4.9b, with a double Gaussian fit with fixed values for μ. We were also able to obtain the 5th harmonic, Fig. 4.9c, which presented a four-fold dependence on the angle and with an isotropic background, similar to the one shown by the lower wavelength peak at 920 nm. A selection of spectra corresponding to the highest count rate is depicted in Fig. 4.10.

The observed four-fold dependence with isotropic contribution, in the 3 mm sample, is similar to the one expected for THG in a crystal with a m3m cubic structure and a p-polarized electric field, E_p, propagating perpendicular to the $<100>$ plane [47]:

$$I_p^{THG}(3\omega_0) \propto [c_0 + c_1 \cos(4\varphi)]^2 |E_p(\omega_0)|^6, \tag{4.8}$$

where φ is the angle between the field's polarization and one of the crystals' unit vectors, in the $<100>$ plane. This expression has a isotropic contribution, c_0, added with a anisotropic term, $c_1 \cos(4\varphi)$, as consequence of the tensorial nature of $\chi^{(3)}$. The lack of angular dependence of the 1 mm when compare to the 3 mm could be associated to the different type of doping in the samples. It is quite possible that the UV doping used in the 1 mm sample created a more isotropic medium by breaking the CaF_2 structure. This is more visible in Fig. 4.7c, which has a higher intensity and therefore less sensitive to noise, where the intensity is constant with the angle, with the exception the 0º due to a damage point in the sample.

The existence of the unexpected peaks might be related to some SCG that changed the structure of the fundamental. This is particular apparent in Fig. 4.9b where the two peaks are obviously coupled, meaning that when the harmonic is more phase-matched the fundamental loses energy resulting in a lower energy for the additional peak.

One must also notice that the overall count rate of the harmonics in the low-power setup is around one order of magnitude smaller in the 3 mm sample, Fig. 4.10, when compared with the 1 mm sample, Fig. 4.8, probably as a result of the absorption by the material.

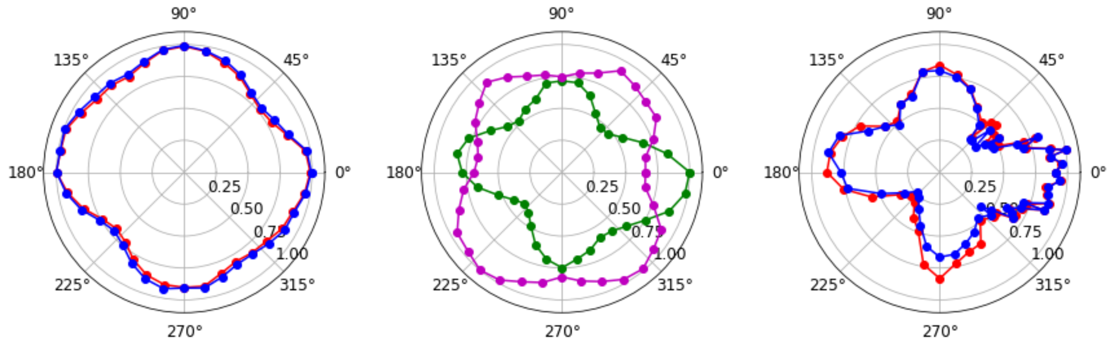

(a) W-initially measured "3rd" harmonic. **(b)** W-Variation of the two peaks. **(c)** W-5th harmonic.

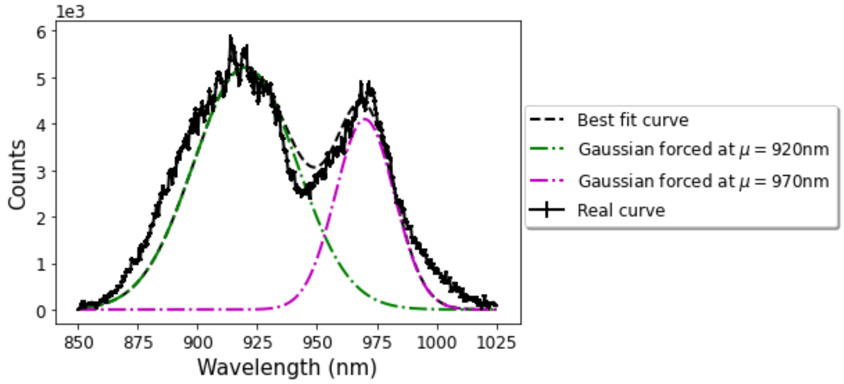

(d) Result of a double Gaussian fit in the region of the third harmonic, correspondent to the point at 0º in Fig.4.9b. Acquisition time of 100 ms.

Figure 4.9: Polar plots for the 3 mm CaF_2 sample. The radius corresponds to the normalized area beneath the curve. In red, green and magenta calculated by a Gaussian fit and in blue by a numerical integration within 1/e^2 of the maximum number of counts. **W** stands for the low-power using a wedge setup while **M** stands for the high-power setup using a mirror.

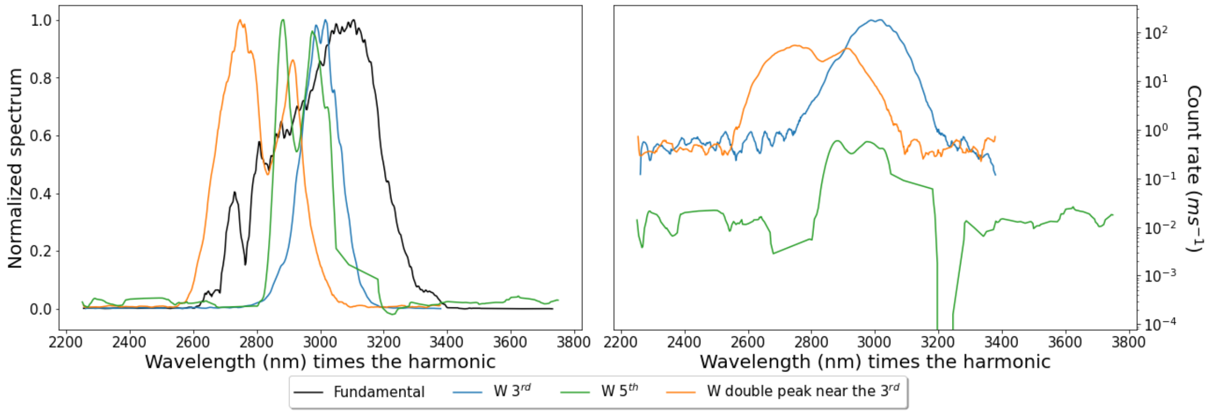

Figure 4.10: Smoothed spectra of all harmonics obtained with a CaF_2 sample of 3 mm. Each spectrum corresponds to the angle with the highest count rate and are centered around the fundamental. On the left all spectra were normalized, while on the right we present the count rate of each spectrum.

4.2.2.2 Fused Silica sample

Fused Silica is a homogeneous material with a very broad transmission range. In our case the sample is a UV grade fused silica, which has high transmission in the range of the harmonics but unfortunately exhibits a drop around 2.7 µm. The main interest of this sample is that it has no crystal structure, as such, the theory exposed in section 4.1.3 is no longer valid. Regardless, You *et al* [48] demonstrated previously the possibility of HHG in fused silica and crystal quartz.

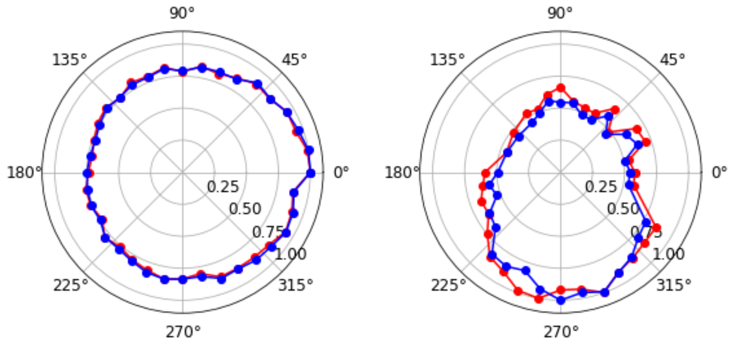

(a) W-3rd harmonic.
(b) W-5th harmonic.

Figure 4.11: Polar plots for the 5 mm fused silica sample. The radius corresponds to the normalized area beneath the curve. In red calculated by a Gaussian fit and in blue by a numerical integration within 1/e^2 of the maximum number of counts. **W** stands for the low-power using a wedge setup while **M** stands for the high-power setup using a mirror.

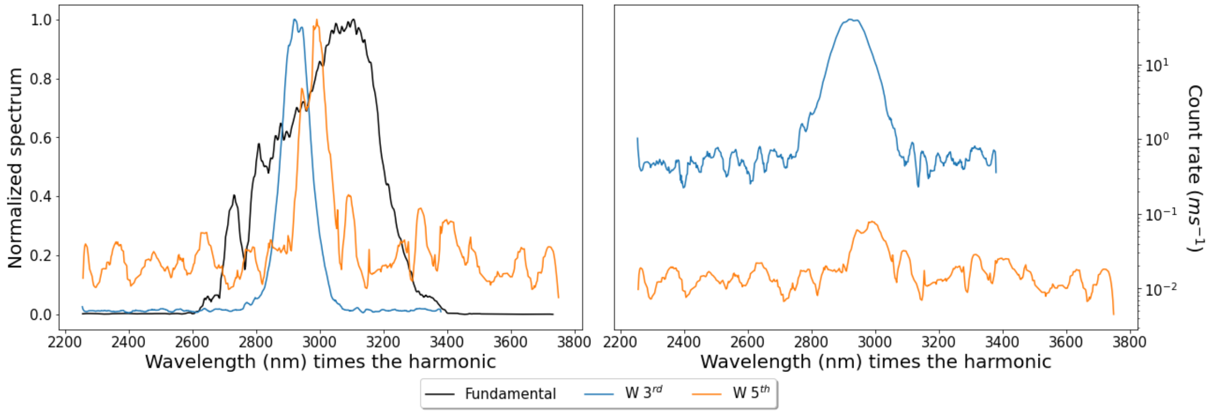

Figure 4.12: Smoothed spectra of all harmonics obtained with a fused silica sample of 5 mm. Each spectrum corresponds to the angle with the highest count rate and are centered around the fundamental. On the left all spectra were normalized, while on the right we present the count rate of each spectrum.

With this sample we observed 3rd and 5th harmonic in the low-power setup, while the high-power one resulted in SCG, Fig. 3.9b. The observed harmonics, Fig. 4.11, do not present any clear angular dependence. In particular, the 3rd harmonic, since it is less susceptible to noise, shows a very isotropic curve, Fig. 4.11a. This is within expectation since fused silica is amorphous. The corresponding spectra are presented in Fig. 4.12.

4.2.2.3 Lithium fluoride sample

Lithium fluoride is a material with a high transmission from 150 nm to 6000 nm, one might add that the transmission of Vacuum UV is excellent, possibly the highest in all of our materials. Additionally, it is also exhibits the largest bandgap, making it the least likely to suffer optical damage, although it is the most physically fragile of them all.

The 3 mm thick LiF sample only generated harmonics in the high-power setup. In this case we obtained harmonics for three positions of the sample. First we placed it 24.4 cm away from the focal lens having obtained a 3$^{\mathrm{rd}}$ and 5$^{\mathrm{th}}$ harmonic, Fig. 4.13b and 4.13d. After this, we moved the sample away from the lens at 25.1 cm where we were only able to measure the 3$^{\mathrm{rd}}$ harmonic due to the poor signal-to-noise ratio of the 5$^{\mathrm{th}}$ harmonic, Fig. 4.13a. Finally, we placed the sample at 24.3 cm from the lens measuring 3$^{\mathrm{rd}}$ and 5$^{\mathrm{th}}$ harmonics, Fig. 4.13c and 4.13e.

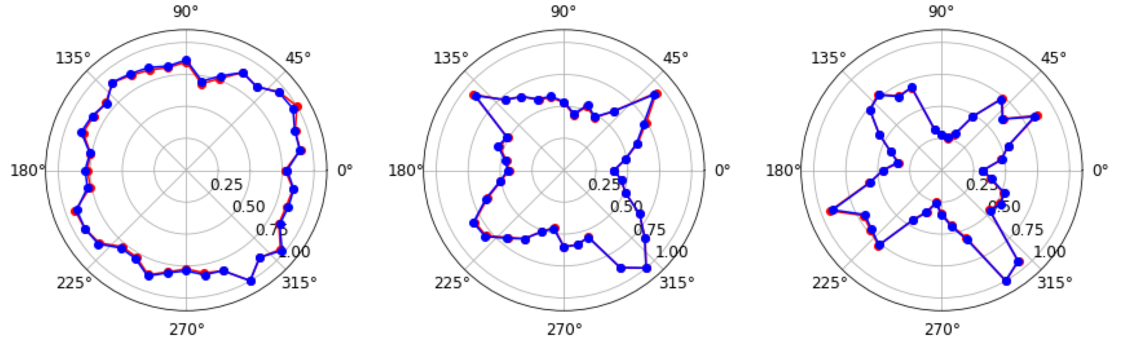

(a) M-3$^{\mathrm{rd}}$ harmonic 25.1 cm from lens. **(b)** M-3$^{\mathrm{rd}}$ harmonic 24.4 cm from lens. **(c)** M-3$^{\mathrm{rd}}$ harmonic 24.3 cm from lens.

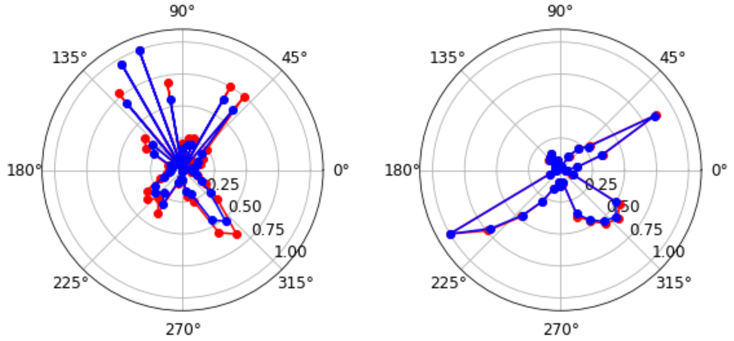

(d) M-5$^{\mathrm{th}}$ harmonic 24.4 cm from lens. **(e)** M-5$^{\mathrm{th}}$ harmonic 24.3 cm from lens.

Figure 4.13: Polar plots for the 3 mm LiF sample. The radius corresponds to the normalized area beneath the curve. In red calculated by a Gaussian fit and in blue by a numerical integration within 1/e^2 of the maximum number of counts.

As we can see in Fig. 4.13, when we place the sample away from the focus we only observe an isotropic

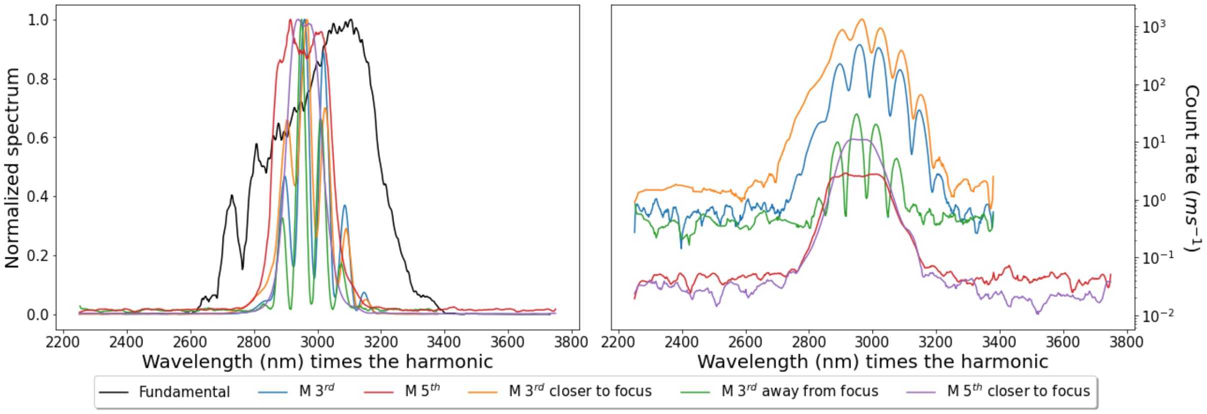

Figure 4.14: Smoothed spectra of all harmonics obtained with a LiF sample of 3 mm. Each spectrum corresponds to the angle with the highest count rate and are centered around the fundamental. On the left all spectra were normalized, while on the right we present the count rate of each spectrum.

curve, but as we get closer we recover the same four-fold curve observed in the 3 mm thick CaF_2 sample and as observed in [47]. However, the 5th harmonic does not present any kind of isotropic response, instead it seems to have a simple four-fold shape, although in Fig. 4.13e at 135° we have a zero that could be associated with a damage point in the sample.

4.2.2.4 Sapphire samples

Sapphire is a material with a high physical resistance, making it an ideal substrate for windows stronger and thinner than with standard glass. It also has a high transmission from the UV to the MIR making it particularly interesting when generating harmonics with MIR light. In this case, we used two samples, with thicknesses of 1 mm and 2 mm. Both samples were labeled as C-cut sapphire, although one of them was actually mislabeled as we will see ahead.

With the 1 mm sample we first obtained the 3rd and 5th harmonics in the low-power setup, Fig. 4.15a and 4.15b. For the high-power setup we placed the sample 24.4 cm after the lens, resulting in the observation of 3rd and 5th harmonics, Fig. 4.15c and 4.15d. In all cases, we observed a four-fold pattern, even though in the case of the 5th we observe a sharp peak, likely due to the formation of a point of damage. However, this does not correspond to the typical behaviour of THG by incidence on the sapphire's C-plane, which should be nearly insensitive to the angle [49, 50]. It is instead close to what should be expected for incidence in either A, M, or R-planes, thus it is likely that this sample was mislabeled as a C-cut. A collection of spectra is presented in Fig. 4.16.

As for the 2 mm sample we obtained 3rd and 5th harmonic for the low-power setup, Fig. 4.17a and 4.17b. In this case the harmonics are nearly insensitive to the angle where the variation in Fig. 4.17b can be explained by noise. This lack of dependence agrees to the expected result with incidence on the

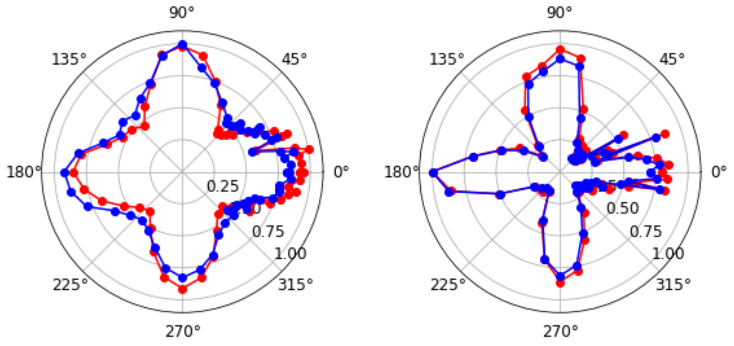

(a) W-3rd harmonic. **(b)** W-5th harmonic.

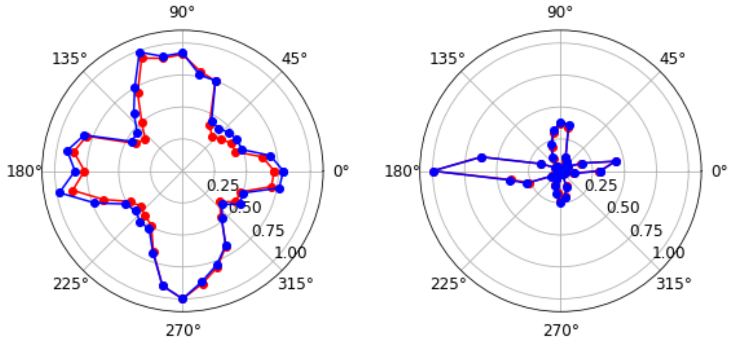

(c) M-3rd harmonic. **(d)** M-5th harmonic.

Figure 4.15: Polar plots for the 1 mm sapphire sample. The radius corresponds to the normalized area beneath the curve. In red calculated by a Gaussian fit and in blue by a numerical integration within 1/e^2 of the maximum number of counts. **W** stands for the low-power using a wedge setup while **M** stands for the high-power setup using a mirror.

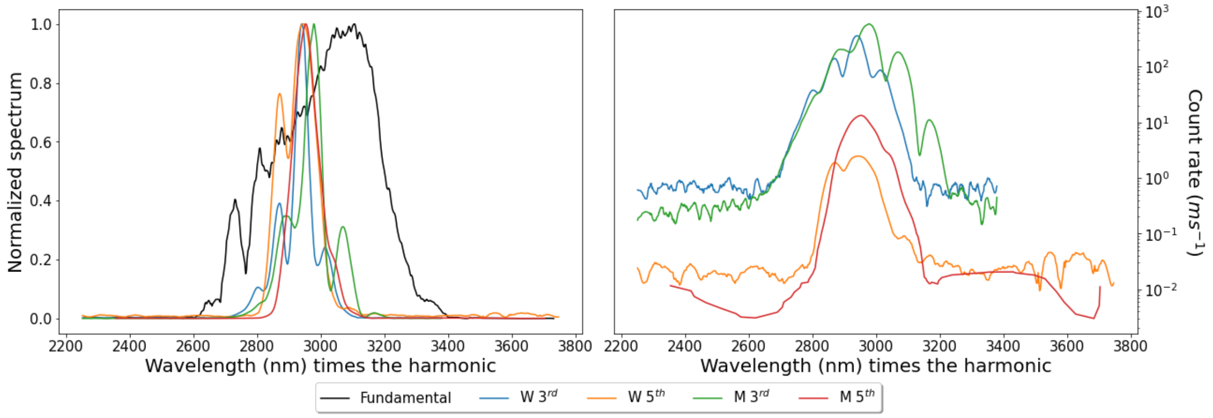

Figure 4.16: Smoothed spectra of all harmonics obtained with a sapphire sample of 1 mm. Each spectrum corresponds to the angle with the highest count rate and are centered around the fundamental. On the left all spectra were normalized, while on the right we present the count rate of each spectrum.

C-plane [49, 50]. The spectra are presented in Fig. 4.18.

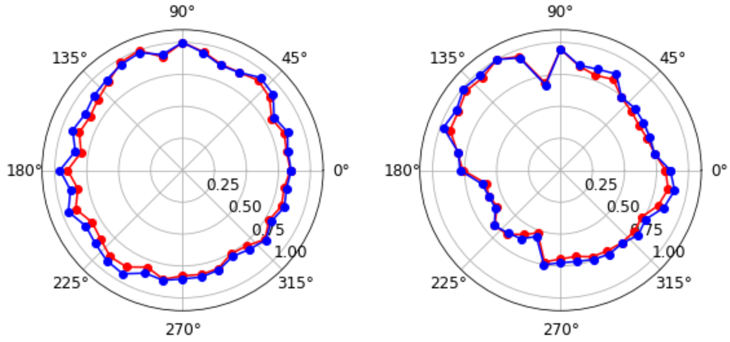

(a) W-3rd harmonic. **(b)** W-5th harmonic.

Figure 4.17: Polar plots for the 2 mm sapphire sample. The radius corresponds to the normalized area beneath the curve. In red calculated by a Gaussian fit and in blue by a numerical integration within 1/e^2 of the maximum number of counts. All this data was taken in the low-power setup with the wedge.

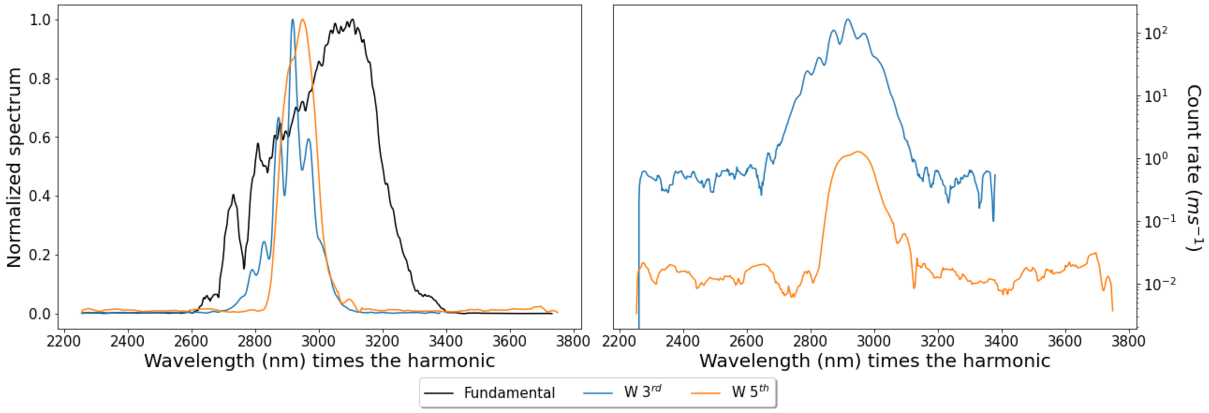

Figure 4.18: Smoothed spectra of all harmonics obtained with a sapphire sample of 2 mm. Each spectrum corresponds to the angle with the highest count rate and are centered around the fundamental. On the left all spectra were normalized, while on the right we present the count rate of each spectrum.

4.2.2.5 Fourier analysis

In Figs. 4.14, 4.16 and 4.18 (LiF and the two sapphires) we noticed than the 3rd harmonic spectra present an interference pattern. This pattern was consistent with the one observed by Garejev *et al* [51]. They observed that this interference was a result of the formation of a third harmonic with two peaks separated in time, which they called free and driven components. These two components should be formed at the sample's surface, but while the free component travels with the typical group velocity for its harmonic frequency, $v_g(3\omega_0)$, the driven component travels at the same group velocity as the fundamental pulse, $v_g(\omega_0)$. To study this phenomenon we assumed that the spectral intensity could be associated with the Fourier Transform (FT) of the temporal wave packet, $\mathrm{FT}(\omega)$, such that

$$I(\omega) = |\mathrm{FT}(\omega)|^2 \tag{4.9}$$

and approximate FT by $\mathrm{FT}(\omega) = \sqrt{I(\omega)} \propto \sqrt{C(\omega)}$, where $C(\omega)$ corresponds to the number of counts at each frequency. For the sapphires $C(\omega)$ was calculated from the highest count spectrum of 3^{rd} harmonic presented in Figs. 4.16 and 4.18. In the case of LiF we opted for the curve obtained when the sample was placed away from focus (corresponding to the "M 3^{rd} away from focus" curve in Fig. 4.14) since it demonstrated the strongest interference pattern. Additionally, while the LiF and the 2 mm sapphire samples show the exact same pattern at each angle, the 1 mm thick sapphire sample shows a smooth change of this pattern with the angle.

We then calculated the Inverse Fourier Transform (IFT) to recover the variation of the electric field with time. The absolute value of IFT is presented in Fig. 4.19, where we observe indeed the existence of two peaks separated by a time interval Δt. The central pulse corresponds to the driven component, which moves faster than the free component in all our samples. The smaller peak in the positive time is the free component while the peak in the negative time arises from the parity of the IFT.

The conditions for the formation of the two components of THG are a large phase mismatch, $\Delta k = k(3\omega_0) - 3k(\omega_0) \propto \Delta n_0 = n_0(3\omega_0) - n_0(\omega)$, and a large group velocity mismatch, $\nu_{13} = 1/v_g(\omega_0) - 1/v_g(3\omega_0)$, [51]. Assuming that all the temporal separation is caused only in the nonlinear environment, inside the sample, we can calculate Δt as:

$$\Delta t = |\nu_{13}| L, \tag{4.10}$$

where L is the length of the sample. The values of $v_g(\omega_0)$ and $v_g(3\omega_0)$ can be calculated as [2]:

$$v_g(\omega) = \frac{c}{n_g(\omega)}, \tag{4.11}$$

where n_g is the group index. The values for all samples are presented in Table 4.1.

Table 4.1: Calculated values for the Fourier analysis of the THG spectra.

Material	n_g		v_g (10^8 m/s)		Δn	ν_{13} (10^{-11} s/m)	L (mm)	Δt (fs)
	1 μm	3 μm	1 μm	3 μm				
CaF$_2$[6]	1.4355	1.4390	2.088	2.083	0.0110	1.167	1	12
							3	35
Fused silica[7]	1.4630	1.4904	2.049	2.011	0.0312	9.140	5	457
LiF[8]	1.3955	1.4103	2.148	2.126	0.0206	4.937	3	148
Sapphire[9]	1.7749	1.8047	1.689	1.661	0.0435	9.940	1	99
							2	199

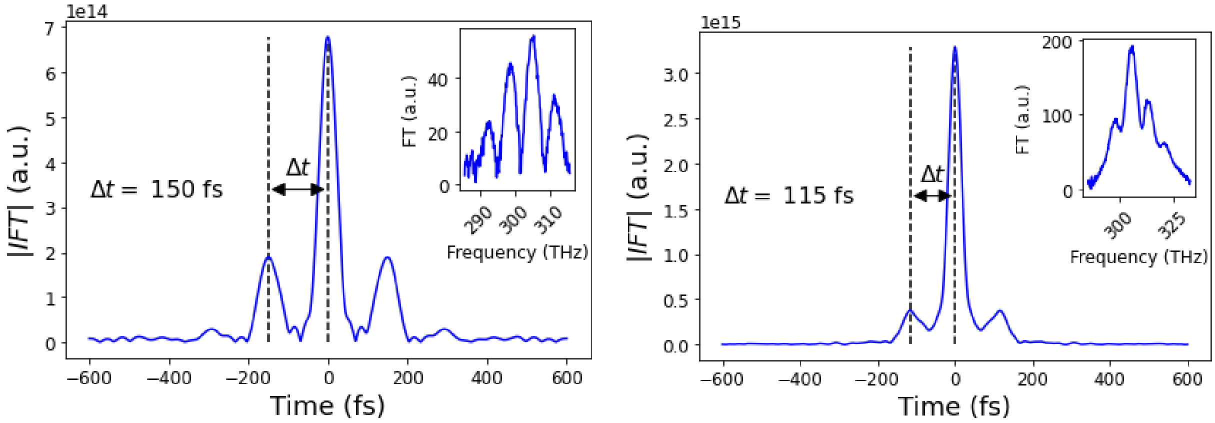

(a) LiF sample **(b)** 1 mm sapphire sample

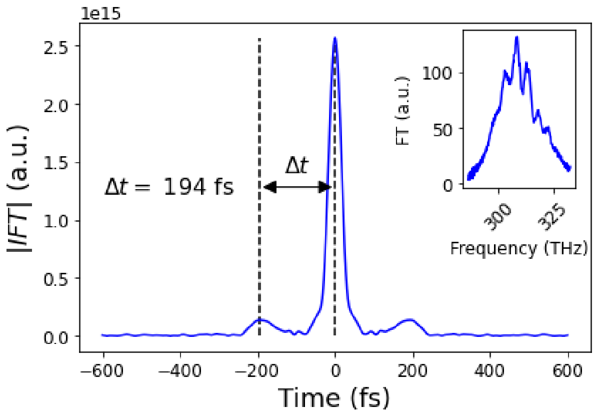

(c) 2 mm sapphire sample

Figure 4.19: Absolute value of the IFT for the THG spectra, in the insets the supposed FT.

As we can see, the experimental values of Δt are close to the theoretical prediction. For the 1 mm sapphire the difference between the two is larger, but this could be associated with the different cut and the consequent difference in the values of n and n_g, which could also explain the variation of the interference pattern with the angle. We also notice that the values of Δn and ν_{13} for the CaF_2 are smaller than in other samples, but most importantly they are smaller than those in the experiment of Garejev *et al* [51], which could explain why we did not observe the formation of the two components in these samples. The most surprising result however, is that that for fused silica the values of Δn and ν_{13} are higher than for LiF, meaning that we should observe interference in this sample. A possible explanation is that for this sample the value of Δt was so large that the peaks of the interference pattern were too

---

[6] `https://refractiveindex.info/?shelf=main&book=CaF2&page=Malitson`
[7] `https://refractiveindex.info/?shelf=glass&book=fused_silica&page=Malitson`
[8] `https://refractiveindex.info/?shelf=main&book=LiF&page=Li`
[9] `https://refractiveindex.info/?shelf=3d&book=crystals&page=sapphire`

close for our spectrometer to discern between consecutive peaks.

4.2.2.6 Final remarks

For us to have an idea of how efficient the harmonic generation is, we used the high-power setup and placed a 4 mm YAG sample in the rotation mount to generate a supercontinuum. Them the spectrum was measured by moving the optical fiber to different positions, recording the spectra in order to reconstruct the full spectrum with all the data. In order to use the same acquisition parameters for all these spectra and to avoid saturating the spectrometer, it was necessary to place a filter (N20A, THORLABS) after the beam dump. Because the power after the filter was too low to measure with the available powermeters it was necessary to use the manufacturer's transmission data to reconstruct the spectra to what they should look like in the absence of the filter, in a similar way to section 3.2.2.2. The transmission curve and respective correction are represented in Fig. 4.20, however, some points at the edges had to be removed because the transmission was so low that the noise of the measurement was enough to generate extremely high counts. After this, at each wavelength, the point with the highest number of counts was taken to form the full spectrum, Fig. 4.21. This spectrum was then numerically integrated giving a total of around 640966 Counts · nm/ms while the measured power was 3.17 ± 1 mW giving a power calibration factor, $\mathcal{C}$, of

$$\mathcal{C} = 202.2\,\frac{\text{Counts}\cdot\text{nm}}{\text{ms}\cdot\mu\text{W}}. \tag{4.12}$$

With the value of $\mathcal{C}$ we calculate the power for each harmonic, P, as well as the rate of harmonic photons, R_{HP}, such that:

$$P_H = \frac{\int_{\lambda_1}^{\lambda_2} C(\lambda),d\lambda}{t_{acq}\mathcal{C}} \qquad R_{HP} = \frac{P_H}{hc/\lambda_H}, \tag{4.13}$$

where t_{acq} is the spectrometer's acquisition time and λ_H = (3000/m) nm the m-nth harmonic's central wavelength. These values are presented in Table 4.2 together with the power conversion efficiency of each harmonic, $\eta = P_H/P_{W,M}$, where P_W = 0.48 W is the input power in the system with the wedge, and P_M = 4.8 W with the mirror.

The power conversion efficiencies are within expectation for perturbative third and fifth harmonic generation [51]. The value R_{HP} is higher in the setup with the mirror since it sends more photons to the sample. However, the behaviour of η is not so simple, while a mirror increases the power we had to make a softer focus and place the samples after the focus to avoid damage. Which reduces the light intensity and therefore explains the reduction of η in the case of the 1 mm thick sapphire sample, when we changed to the setup with the mirror. This dependence in intensity is apparent when we compare the values of R_{HP} and η for harmonics taken at a different distance of the focus, naturally with the closest ones (higher intensity) having higher values.

Overall the obtained harmonics seem to be perturbative when we take into account the angular dependence with the polarization. However, to prove this hypothesis we would need to measure the variation of the harmonic intensity with the intensity of the input field. For perturbative harmonics, the intensity of the m-nth harmonic grows with a power-law $I(m\omega_0) \propto I^m(\omega_0)$ unlike the harmonics resulting from HHG [17]. This could be achieved, for example, with a half-wave plate combined with a polarizer to change the power sent to the sample, however, we currently do not possess those components for the 3 µm range. As such we cannot exclude the possibility that the observed harmonics could have been generated through HHG, in particular for the harmonics generated in the 1 mm thick CaF_2 sample, which not only generated up to the 9th harmonic but also showed no response to variation of the orientation of the sample nor the formation of two THG components.

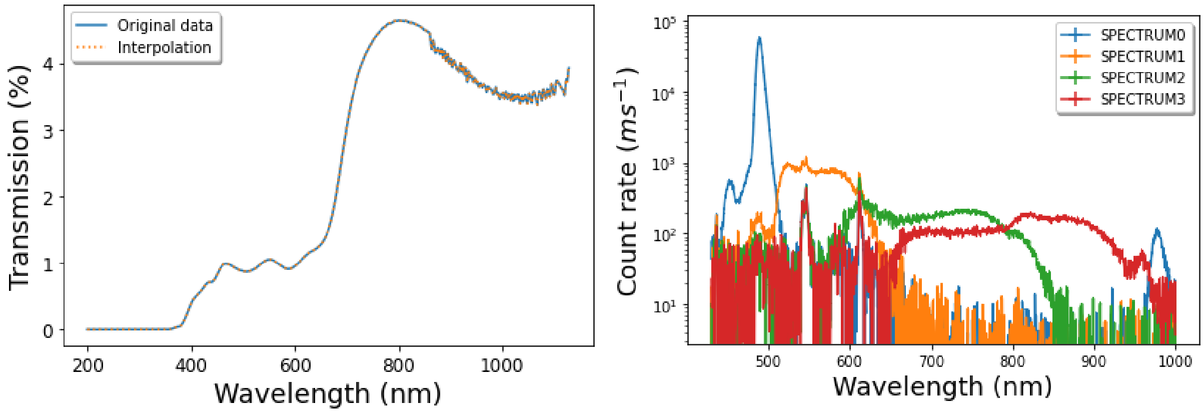

Figure 4.20: On the left is the interpolation of the transmission data of the filter in the region of interest for the calibration. On the right four SCG spectra obtained in different positions of the fiber, after the correction of transmission and division by the acquisition time.

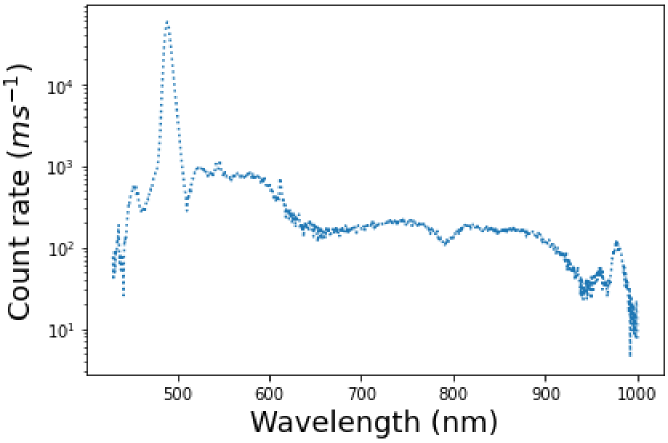

Figure 4.21: Final supercontinuum spectrum for integration and calibration of the harmonic's power.

Table 4.2: Approximated power, photon rate and efficiency of each harmonic.

Sample	Thickness	Crystal class	Harmonic	P_H (µW)	R_{HP} (s^{-1})	η
UV grade CaF_2	1 mm	m3m	W 3rd	5.67×10^{1}	2.85×10^{14}	1.18×10^{-4}
			W 5th	2.34×10^{-1}	7.06×10^{11}	4.87×10^{-7}
			M 3rd	1.92×10^{3}	9.66×10^{15}	4.00×10^{-4}
			M 5th	4.27×10^{1}	1.29×10^{14}	8.89×10^{-6}
			M 7th	4.63×10^{-2}	9.99×10^{10}	9.65×10^{-9}
			M 9th	8.98×10^{-3}	1.51×10^{10}	1.87×10^{-9}
			M 9th closer to focus	9.48×10^{-3}	1.59×10^{10}	1.97×10^{-9}
			M unknown near the 3rd	1.19×10^{3}	6.00×10^{15}	2.48×10^{-4}
			M unknown near the 5th	1.79×10^{1}	5.42×10^{13}	3.74×10^{-6}
IR grade CaF_2	3 mm	m3m	W 3rd	4.15×10^{1}	2.09×10^{14}	8.65×10^{-5}
			W 5th	8.84×10^{-2}	2.67×10^{11}	1.84×10^{-7}
UV grade fused silica	5 mm	Amorphous	W 3rd	7.26×10^{0}	3.66×10^{13}	1.51×10^{-5}
			W 5th	6.78×10^{-3}	2.05×10^{10}	1.41×10^{-8}
LiF	3 mm	m3m	M 3rd	7.79×10^{1}	3.92×10^{14}	1.62×10^{-5}
			M 5th	5.30×10^{-1}	1.60×10^{12}	1.10×10^{-7}
			M 3rd closer to focus	2.52×10^{2}	1.27×10^{15}	5.25×10^{-5}
			M 3rd away from focus	3.25×10^{0}	1.63×10^{13}	6.76×10^{-7}
			M 5th closer to focus	1.37×10^{0}	4.14×10^{12}	2.85×10^{-7}
Sapphire unkown cut (A, M, R)	1 mm	$\bar{3}$m	W 3rd	4.69×10^{1}	2.36×10^{14}	9.76×10^{-5}
			W 5th	3.09×10^{-1}	9.33×10^{11}	6.43×10^{-7}
			M 3rd	9.80×10^{1}	4.94×10^{14}	2.04×10^{-5}
			M 5th	1.32×10^{0}	3.99×10^{12}	2.75×10^{-7}
C-cut sapphire	2 mm	$\bar{3}$m	W 3rd	2.80×10^{1}	1.41×10^{14}	5.83×10^{-5}
			W 5th	1.53×10^{-1}	4.61×10^{11}	3.18×10^{-7}

4.3 Simulation in literature

In this section, we present some of the procedures found in the literature for the simulation of harmonic generation. We will abstain, however, from performing said simulations. The simulation of harmonics is rather complex, in particular in solids, so much that they are normally performed by large teams of experts in the field, sometimes taking years to obtain results and only studying a few aspects of harmonic generation. This is out of the scope of this master thesis, which is mainly experimental and centered around the capabilities of the new laser system at L2I and not harmonics explicitly.

The simulation of perturbative harmonics is many times centered around SHG and THG. The most direct method for the simulation of nonlinear effects involves solving the forward Maxwell's equation for the complete electric and magnetic fields [52, 53]. While more complete, this kind of approach tends to have a high computational cost and so many times it is preferred to use an approximation such as the slowly varying wave or slowly varying envelope to solve the nonlinear Schrödinger equation or one of its countless variations [54, 55]. A good review of many methods for simulation of nonlinear effects, in a more general case, is presented by Couairon *et al* [56].

For bulk materials, the most complete simulations normally include both perturbative harmonics and HHG including the band systems and sometimes the dependence on the orientation of the input field's polarization. Yu *et al* present a remarkably complete review of the primary numerical methods for this kind of simulation in solids [57], including methods based on the time-dependent Schrödinger equation, semiconductor Bloch equations, and dependent density-functional theory. All of these methods are of extreme complexity and require a considerable knowledge on the structure of the medium.

5

Conclusion

Contents

5.1 **Review** 67

  5.1.1 Chapter 3 67

  5.1.2 Chapter 4 67

5.2 **Future work** 68

  5.2.1 Spectral broadening 68

  5.2.2 Harmonic Generation 68

In the work reported in this thesis we explored some of the capabilities of the new laser system installed at L2I in the IST Alameda campus. In this final chapter we make a quick review of the main topics and results of this thesis, ending with a comment on the perspectives and planned future works.

5.1 Review

5.1.1 Chapter 3

In this chapter, we presented spectral broadening in the normal (1.03 μm) and anomalous (3 μm) dispersion regime, the last leading to the formation of a supercontinuum.

For the normal regime, we experimentally observe the importance of the intensity and propagation length for the broadening. The experimental data was then compared to a simplified theoretical model, based on solving a GNLSE in a nonlinear waveguide but in the absence of self-focus or filamentation. The mismatch between the experiment and this simple numerical model points to the formation of a filament in the samples, due to self-focusing, with the formation of free electrons.

In the anomalous regime, we have observed the wings of the supercontinuum that includes the visible range, which is in agreement with other experimental works [29–31]. The spectral broadening achieved is many times larger than what was achieved using the 1.03 μm pump even though the pump power is $\sim$ 17 times higher than the 3 μm laser, going from a 6 nm FWHM to the formation of wings more than 2000 nm away from the fundamental. This is a clear proof of the advantages of the new system at L2I that now allows us to observe these new and exotic physical phenomena.

5.1.2 Chapter 4

In this chapter, we performed harmonic generation from a 3 μm laser field. We present the angular dependence for a number of solid media and harmonic orders, which in an overall fashion coincide with the expected results from perturbative harmonic generation. In the particular case of a 1 mm thick UV grade CaF_2 window, we cannot exclude, without reasonable doubt, the possibility of HHG.

Additionally, we performed a Fourier analysis for some of the obtained THG spectra that presented an interference pattern. This study points to the formation of two THG components: free and driven. The results are within those predicted by theory [51], including the lack of observation of these two components in other samples.

After this, we performed a study of the efficiency of the harmonic generation, which is once again within expectations for perturbative harmonic generation, at least for the 3rd and 5th harmonic.

This chapter was concluded with some of the procedures for the simulation of harmonics generation.

5.2 Future work

5.2.1 Spectral broadening

An interesting work at 3 μm would be the study of the full supercontinuum spectra instead of only the wings. We currently possess a *MOZZA* spectrometer by *FASTLITE* with a spectral range of 1 – 5 μm which, together with the spectrometer used in our experiments (*FLEX-STD-UV-Vis-NIR*, *SARSPEC*) would allow us to cover the entire supercontinuum spectrum. During our experiments, we had some coupling problems with this system, and as such were unable to use it, but once these limitations are solved we should be able to obtain the desired data.

Another component to study would be the variation of the temporal shape of the pulses in both sets of experiments: this would allow studying the possibility of pulse-splitting or self-compression. A possible way to do this would be using a Frequency-Resolved Optical Gating (FROG) system. In fact, in parallel to this thesis, there was the development of such a system designed for $\sim$ 3 μm, as L2I was already equipped with a similar device for the $\sim$ 1 μm.

5.2.2 Harmonic Generation

The generation of harmonics, in particular HHG, normally involves custom-made thin crystals of the order of microns. So one of the next steps to obtain HHG would be to acquire such crystals. In that sense, we would also need means to more accurately control the energy sent to the samples, which could imply the acquisition of a half-wave plate and a polarizer for the 3 μm range. In particular to study the dependence on the intensity of the harmonics with the fundamental electric field to conclude, without reasonable doubt, that they are indeed high-harmonic and not perturbative.

Additionally, while our Fourier approach produced good results it might be preferable to measure directly the temporal shape of the third-harmonics. This could be accomplished, once again, with a FROG system, in this case the $\sim$ 1 μm.

Finally, all the harmonic spectra were taken while changing the sample's orientation manually. Even in the cases where we measured in intervals of 10º (the largest interval used but in some cases, we used intervals of 4º) that would result in 36 acquisitions, which amounts, for our 25 presented harmonics, to at least 900 acquisitions. So naturally, it would be preferable to automatize the system to acquire more data and with higher accuracy. The same idea can also be applied to the position of the sample that is controlled manually using the translation stage. In that regard, we are in the process of acquiring motorized equipment to automatize the entire process for future experiments, either by us or other groups within GoLP or other partnerships.

Bibliography

[1] J. Ma, Z. Qin, G. Xie, L. Qian, and D. Tang, “Review of mid-infrared mode-locked laser sources in the 2.0 μ m–3.5 μ m spectral region,” *Applied Physics Reviews*, vol. 6, no. 2, p. 021317, jun 2019. [Online]. Available: http://aip.scitation.org/doi/10.1063/1.5037274

[2] P. Rüdiger, *Encyclopedia of laser physics and technology*, 1st ed. Wiley-VCH, 2008, accessed online version on 10-2021. [Online]. Available: https://www.rp-photonics.com/encyclopedia.html

[3] “The Nobel Prize in Physics 2005.” [Online]. Available: https://www.nobelprize.org/prizes/physics/2005/summary/

[4] E. Sorokin, I. T. Sorokina, J. Mandon, G. Guelachvili, and N. Picque, “Sensitive multiplex spectroscopy in the molecular fingerprint 2.4 μm region with a Crˆ2+:ZnSe femtosecond laser,” *Optics Express*, vol. 15, no. 25, p. 16540, 2007. [Online]. Available: https://www.osapublishing.org/oe/abstract.cfm?uri=oe-15-25-16540

[5] M. L. Groot, N. P. Pawlowicz, L. J. G. W. van Wilderen, J. Breton, I. H. M. van Stokkum, and R. van Grondelle, “Initial electron donor and acceptor in isolated Photosystem II reaction centers identified with femtosecond mid-IR spectroscopy,” *Proceedings of the National Academy of Sciences*, vol. 102, no. 37, pp. 13 087–13 092, sep 2005. [Online]. Available: http://www.pnas.org/cgi/doi/10.1073/pnas.0503483102

[6] Y. S. Kim and R. M. Hochstrasser, “Applications of 2D IR Spectroscopy to Peptides, Proteins, and Hydrogen-Bond Dynamics,” *The Journal of Physical Chemistry B*, vol. 113, no. 24, pp. 8231–8251, jun 2009. [Online]. Available: https://pubs.acs.org/doi/10.1021/jp8113978

[7] T.-T. Yeh, H. Shirai, C.-M. Tu, T. Fuji, T. Kobayashi, and C.-W. Luo, “Ultrafast carrier dynamics in Ge by ultra-broadband mid-infrared probe spectroscopy,” *Scientific Reports*, vol. 7, no. 1, p. 40492, feb 2017. [Online]. Available: http://www.nature.com/articles/srep40492

[8] B. Voisiat, D. Gaponov, P. Gečys, L. Lavoute, M. Silva, A. Hideur, N. Ducros, and G. Račiukaitis, “Material processing with ultra-short pulse lasers working in 2μm wavelength range,” S. Roth,

Y. Nakata, B. Neuenschwander, and X. Xu, Eds., mar 2015, p. 935014. [Online]. Available: http://proceedings.spiedigitallibrary.org/proceeding.aspx?doi=10.1117/12.2078651

[9] S. Amini-Nik, D. Kraemer, M. L. Cowan, K. Gunaratne, P. Nadesan, B. A. Alman, and R. J. D. Miller, "Ultrafast Mid-IR Laser Scalpel: Protein Signals of the Fundamental Limits to Minimally Invasive Surgery," *PLoS ONE*, vol. 5, no. 9, p. e13053, sep 2010. [Online]. Available: https://dx.plos.org/10.1371/journal.pone.0013053

[10] M. R. Abu Hassan, F. Yu, W. J. Wadsworth, and J. C. Knight, "Cavity-based mid-IR fiber gas laser pumped by a diode laser," *Optica*, vol. 3, no. 3, p. 218, mar 2016. [Online]. Available: https://www.osapublishing.org/abstract.cfm?URI=optica-3-3-218

[11] R. R. Alfano and S. L. Shapiro, "Emission in the region 4000 to 7000 Å via four-photon coupling in glass," *Physical Review Letters*, vol. 24, no. 11, pp. 584–587, mar 1970. [Online]. Available: https://link.aps.org/doi/10.1103/PhysRevLett.24.584

[12] J. T. Manassah, R. R. Alfano, and M. Mustafa, "Spectral distribution of an ultrafast supercontinuum laser source," *Physics Letters A*, vol. 107, no. 7, pp. 305–309, feb 1985. [Online]. Available: https://linkinghub.elsevier.com/retrieve/pii/0375960185906413

[13] M. Ferray, A. L'Huillier, X. F. Li, L. A. Lompre, G. Mainfray, and C. Manus, "Multiple-harmonic conversion of 1064 nm radiation in rare gases," *Journal of Physics B: Atomic, Molecular and Optical Physics*, vol. 21, no. 3, pp. L31–L35, feb 1988. [Online]. Available: https://iopscience.iop.org/article/10.1088/0953-4075/21/3/001

[14] B. E. A. Saleh and M. C. Teich, *Fundamentals of Photonics*, 3rd ed. Wiley Blackwell, 2019.

[15] T. Popmintchev, M. C. Chen, D. Popmintchev, P. Arpin, S. Brown, S. Ališauskas, G. Andriukaitis, T. Balčiunas, O. D. Mücke, A. Pugzlys, A. Baltuška, B. Shim, S. E. Schrauth, A. Gaeta, C. Hernández-García, L. Plaja, A. Becker, A. Jaron-Becker, M. M. Murnane, and H. C. Kapteyn, "Bright coherent ultrahigh harmonics in the keV x-ray regime from mid-infrared femtosecond lasers," *Science*, vol. 336, no. 6086, pp. 1287–1291, jun 2012. [Online]. Available: https://www.sciencemag.org/lookup/doi/10.1126/science.1218497

[16] G. Vampa, Y. S. You, H. Liu, S. Ghimire, and D. A. Reis, "Observation of backward high-harmonic emission from solids," *Optics Express*, vol. 26, no. 9, p. 12210, apr 2018. [Online]. Available: https://www.osapublishing.org/abstract.cfm?URI=oe-26-9-12210

[17] S. Ghimire, A. D. DiChiara, E. Sistrunk, P. Agostini, L. F. DiMauro, and D. A. Reis, "Observation of high-order harmonic generation in a bulk crystal," *Nature Physics*, vol. 7, no. 2, pp. 138–141, feb 2011. [Online]. Available: http://www.nature.com/articles/nphys1847

[18] F. Calegari, G. Sansone, S. Stagira, C. Vozzi, and M. Nisoli, “Advances in attosecond science,” *Journal of Physics B: Atomic, Molecular and Optical Physics*, vol. 49, no. 6, p. 062001, mar 2016. [Online]. Available: http://dx.doi.org/10.1088/0953-4075/49/6/062001https://iopscience.iop.org/article/10.1088/0953-4075/49/6/062001

[19] P. Russbueldt, D. Hoffmann, M. Hofer, J. Lohring, J. Luttmann, A. Meissner, J. Weitenberg, M. Traub, T. Sartorius, D. Esser, R. Wester, P. Loosen, and R. Poprawe, “Innoslab amplifiers,” *IEEE Journal of Selected Topics in Quantum Electronics*, vol. 21, no. 1, pp. 447–463, jan 2015. [Online]. Available: http://ieeexplore.ieee.org/document/6843864/

[20] R. W. Boyd, *Nonlinear Optics*, 4th ed. Elsevier, AP Academic Press, 2020.

[21] S. L. Chin, S. A. Hosseini, W. Liu, Q. Luo, F. Théberge, N. Aközbek, A. Becker, V. P. Kandidov, O. G. Kosareva, and H. Schroeder, “The propagation of powerful femtosecond laser pulses in opticalmedia: physics, applications, and new challenges,” *Canadian Journal of Physics*, vol. 83, no. 9, pp. 863–905, sep 2005. [Online]. Available: http://www.nrcresearchpress.com/doi/10.1139/p05-048

[22] R. W. Boyd, S. G. Lukishova, and Y. R. Shen, *Self-focusing: Past and Present Fundamentals and Prospects*, ser. Topics in Applied Physics. Springer New York, 2009, vol. 114.

[23] E. O. Smetanina, V. O. Kompanets, A. E. Dormidonov, S. V. Chekalin, and V. P. Kandidov, “Light bullets from near-IR filament in fused silica,” *Laser Physics Letters*, vol. 10, no. 10, p. 105401, oct 2013. [Online]. Available: https://iopscience.iop.org/article/10.1088/1612-2011/10/10/105401

[24] J. Marburger, “Self-focusing: Theory,” *Progress in Quantum Electronics*, vol. 4, pp. 35–110, apr 1975. [Online]. Available: https://linkinghub.elsevier.com/retrieve/pii/0079672775900038

[25] A. Dubietis, G. Tamošauskas, R. Šuminas, V. Jukna, and A. Couairon, “Ultrafast supercontinuum generation in bulk condensed media (Invited Review),” *arXiv*, jun 2017. [Online]. Available: http://arxiv.org/abs/1706.04356

[26] G. P. Agrawal, *Nonlinear Fiber Optics*, 6th ed. Academic Press, an imprint of Elsevier, 2019.

[27] M. Hemmer, M. Baudisch, A. Thai, A. Couairon, and J. Biegert, “Self-compression to sub-3-cycle duration of mid-infrared optical pulses in dielectrics,” *Optics Express*, vol. 21, no. 23, p. 28095, nov 2013. [Online]. Available: https://www.osapublishing.org/oe/abstract.cfm?uri=oe-21-23-28095

[28] S. V. Chekalin, V. O. Kompanets, E. O. Smetanina, and V. P. Kandidov, “Light bullets and supercontinuum spectrum during femtosecond pulse filamentation under conditions of anomalous group-velocity dispersion in fused silicalicati,” *Quantum Electronics*, vol. 43, no. 4,

pp. 326–331, apr 2013. [Online]. Available: http://stacks.iop.org/1063-7818/43/i=4/a=326?key=crossref.4661b2f19a17f208a582e0b86e640788

[29] M. Durand, K. Lim, V. Jukna, E. McKee, M. Baudelet, A. Houard, M. Richardson, A. Mysyrowicz, and A. Couairon, "Blueshifted continuum peaks from filamentation in the anomalous dispersion regime," *Physical Review A*, vol. 87, no. 4, p. 043820, apr 2013. [Online]. Available: https://link.aps.org/doi/10.1103/PhysRevA.87.043820

[30] J. A. Dharmadhikari, R. A. Deshpande, A. Nath, K. Dota, D. Mathur, and A. K. Dharmadhikari, "Effect of group velocity dispersion on supercontinuum generation and filamentation in transparent solids," *Applied Physics B*, vol. 117, no. 1, pp. 471–479, oct 2014. [Online]. Available: http://link.springer.com/10.1007/s00340-014-5857-3

[31] E. O. Smetanina, V. O. Kompanets, S. V. Chekalin, A. E. Dormidonov, and V. P. Kandidov, "Anti-Stokes wing of femtosecond laser filament supercontinuum in fused silica," *Optics Letters*, vol. 38, no. 1, p. 16, jan 2013. [Online]. Available: https://www.osapublishing.org/abstract.cfm?URI=ol-38-1-16

[32] J. Hult, "A fourth-order Runge–Kutta in the interaction picture method for simulating supercontinuum generation in optical fibers," *Journal of Lightwave Technology*, vol. 25, no. 12, pp. 3770–3775, dec 2007. [Online]. Available: http://ieeexplore.ieee.org/document/4397001/

[33] A. Martínez-Rios, B. Ilan, I. Torres-Gómez, D. Monzon-Hernandez, and D. E. Ceballos-Herrera, "Calculation of higher order dispersion coefficients in photonic crystal fibers," in *22nd Congress of the International Commission for Optics: Light for the Development of the World*, R. Rodríguez-Vera and R. Díaz-Uribe, Eds., vol. 8011, no. 2, aug 2011, p. 80110A. [Online]. Available: http://proceedings.spiedigitallibrary.org/proceeding.aspx?doi=10.1117/12.901625

[34] J. H. Kim, M.-K. Chen, C.-E. Yang, J. Lee, S. S. Yin, P. Ruffin, E. Edwards, C. Brantley, and C. Luo, "Broadband IR supercontinuum generation using single crystal sapphire fibers," *Optics Express*, vol. 16, no. 6, p. 4085, mar 2008. [Online]. Available: https://www.osapublishing.org/oe/abstract.cfm?uri=oe-16-6-4085

[35] K. Blow and D. Wood, "Theoretical description of transient stimulated Raman scattering in optical fibers," *IEEE Journal of Quantum Electronics*, vol. 25, no. 12, pp. 2665–2673, 1989. [Online]. Available: http://ieeexplore.ieee.org/document/40655/

[36] D. Hollenbeck and C. D. Cantrell, "Multiple-vibrational-mode model for fiber-optic Raman gain spectrum and response function," *Journal of the Optical Society of America B*, vol. 19, no. 12, p. 2886, dec 2002. [Online]. Available: https://www.osapublishing.org/abstract.cfm?URI=josab-19-12-2886

[37] N. Daher, F. Guichard, S. W. Jolly, X. Délen, F. Quéré, M. Hanna, and P. Georges, “Multipass cells: 1D numerical model and investigation of spatio-spectral couplings at high nonlinearity,” *Journal of the Optical Society of America B*, vol. 37, no. 4, p. 993, apr 2020. [Online]. Available: https://www.osapublishing.org/abstract.cfm?URI=josab-37-4-993

[38] O. Uteza, B. Bussière, F. Canova, J.-P. Chambaret, P. Delaporte, T. Itina, and M. Sentis, “Damage threshold of sapphire in short and long pulse regime,” in *International Conference on Lasers, Applications, and Technologies 2007: Laser-assisted Micro- and Nanotechnologies*, V. Y. Panchenko, O. A. Louchev, and S. Malyshev, Eds., vol. 6732, jun 2007, p. 67321P. [Online]. Available: http://proceedings.spiedigitallibrary.org/proceeding.aspx?doi=10.1117/12.752215

[39] P. B. Corkum, “Plasma perspective on strong field multiphoton ionization,” *Physical Review Letters*, vol. 71, no. 13, pp. 1994–1997, sep 1993. [Online]. Available: https://link.aps.org/doi/10.1103/PhysRevLett.71.1994

[40] K. C. Kulander, K. J. Schafer, and J. L. Krause, “Dynamics of short-pulse excitation, ionization and harmonic conversion,” in *Super-Intense Laser-Atom Physics*, ser. NATO ASI Series, B. Piraux, A. L’Huillier, and K. Rzążewski, Eds. Plenum Press, 1993, pp. 95–110. [Online]. Available: https://link.springer.com/chapter/10.1007%2F978-1-4615-7963-2_10

[41] M. Lewenstein, P. Balcou, M. Y. Ivanov, A. L’Huillier, and P. B. Corkum, “Theory of high-harmonic generation by low-frequency laser fields,” *Physical Review A*, vol. 49, no. 3, pp. 2117–2132, mar 1994. [Online]. Available: https://link.aps.org/doi/10.1103/PhysRevA.49.2117

[42] S. Ghimire and D. A. Reis, “High-harmonic generation from solids,” *Nature Physics*, vol. 15, no. 1, pp. 10–16, jan 2019. [Online]. Available: http://www.nature.com/articles/s41567-018-0315-5

[43] G. Vampa, C. R. McDonald, G. Orlando, D. D. Klug, P. B. Corkum, and T. Brabec, “Theoretical analysis of high-harmonic generation in solids,” *Physical Review Letters*, vol. 113, no. 7, p. 073901, aug 2014. [Online]. Available: https://link.aps.org/doi/10.1103/PhysRevLett.113.073901

[44] A. F. Kemper, B. Moritz, J. K. Freericks, and T. P. Devereaux, “Theoretical description of high-order harmonic generation in solids,” *New Journal of Physics*, vol. 15, no. 2, p. 023003, feb 2013. [Online]. Available: https://iopscience.iop.org/article/10.1088/1367-2630/15/2/023003

[45] K. Leo, “Interband optical investigation of Bloch oscillations in semiconductor superlattices,” *Semiconductor Science and Technology*, vol. 13, no. 3, pp. 249–263, mar 1998. [Online]. Available: https://iopscience.iop.org/article/10.1088/0268-1242/13/3/003

[46] L. Liu, J. Zhao, J.-M. Yuan, and Z.-X. Zhao, "Role of Bloch oscillation in high-order harmonic generation from periodic structure," *Chinese Physics B*, vol. 28, no. 11, p. 114205, nov 2019. [Online]. Available: https://iopscience.iop.org/article/10.1088/1674-1056/ab47f7

[47] G. Petrocelli, E. Pichini, F. Scudieri, and S. Martellucci, "Anisotropic effects in the third-harmonic-generation process in cubic crystals," *Journal of the Optical Society of America B*, vol. 10, no. 5, p. 918, may 1993. [Online]. Available: https://www.osapublishing.org/abstract.cfm?URI=josab-10-5-918

[48] Y. S. You, Y. Yin, Y. Wu, A. Chew, X. Ren, F. Zhuang, S. Gholam-Mirzaei, M. Chini, Z. Chang, and S. Ghimire, "High-harmonic generation in amorphous solids," *Nature Communications*, vol. 8, no. 1, p. 724, dec 2017. [Online]. Available: http://www.nature.com/articles/s41467-017-00989-4

[49] J. Jiao, B. J. Chun, Y. Gao, and Y.-J. Kim, "Third harmonic generation at sapphire wafers with different cut axis," in *2017 Conference on Lasers and Electro-Optics Pacific Rim (CLEO-PR)*, vol. 2017-Janua. IEEE, jul 2017, pp. 1–3. [Online]. Available: http://ieeexplore.ieee.org/document/8118660/

[50] G. Yi, H. Lee, J. Jiannan, B. J. Chun, S. Han, H. Kim, Y. W. Kim, D. Kim, S.-W. Kim, and Y.-J. Kim, "Nonlinear third harmonic generation at crystalline sapphires," *Optics Express*, vol. 25, no. 21, p. 26002, oct 2017. [Online]. Available: https://www.osapublishing.org/abstract.cfm?URI=oe-25-21-26002

[51] N. Garejev, I. Gražulevičiūtė, D. Majus, G. Tamošauskas, V. Jukna, A. Couairon, and A. Dubietis, "Third- and fifth-harmonic generation in transparent solids with few-optical-cycle midinfrared pulses," *Physical Review A*, vol. 89, no. 3, p. 033846, mar 2014. [Online]. Available: https://link.aps.org/doi/10.1103/PhysRevA.89.033846

[52] J. Darginavičius, D. Majus, V. Jukna, N. Garejev, G. Valiulis, A. Couairon, and A. Dubietis, "Ultrabroadband supercontinuum and third-harmonic generation in bulk solids with two optical-cycle carrier-envelope phase-stable pulses at 2 μm," *Optics Express*, vol. 21, no. 21, p. 25210, oct 2013. [Online]. Available: https://www.osapublishing.org/oe/abstract.cfm?uri=oe-21-21-25210

[53] J. C. A. Tyrrell *, P. Kinsler, and G. H. C. New, "Pseudospectral spatial-domain: a new method for nonlinear pulse propagation in the few-cycle regime with arbitrary dispersion," *Journal of Modern Optics*, vol. 52, no. 7, pp. 973–986, may 2005. [Online]. Available: http://www.tandfonline.com/doi/abs/10.1080/09500340512331334086

[54] G. Genty, P. Kinsler, B. Kibler, and J. M. Dudley, "Nonlinear envelope equation modeling of sub-cycle dynamics and harmonic generation in nonlinear waveguides," *Optics Express*, vol. 15, no. 9, p. 5382, 2007. [Online]. Available: https://www.osapublishing.org/oe/abstract.cfm?uri=oe-15-9-5382

[55] B. Kibler, R. Fischer, G. Genty, D. Neshev, and J. Dudley, “Simultaneous fs pulse spectral broadening and third harmonic generation in highly nonlinear fibre: experiments and simulations,” *Applied Physics B*, vol. 91, no. 2, pp. 349–352, may 2008. [Online]. Available: http://link.springer.com/10.1007/s00340-008-3012-8

[56] A. Couairon, E. Brambilla, T. Corti, D. Majus, O. de J. Ramírez-Góngora, and M. Kolesik, “Practitioner’s guide to laser pulse propagation models and simulation,” *The European Physical Journal Special Topics*, vol. 199, no. 1, pp. 5–76, nov 2011. [Online]. Available: http://link.springer.com/10.1140/epjst/e2011-01503-3

[57] C. Yu, S. Jiang, and R. Lu, “High order harmonic generation in solids: a review on recent numerical methods,” *Advances in Physics: X*, vol. 4, no. 1, p. 1562982, jan 2019. [Online]. Available: https://www.tandfonline.com/doi/full/10.1080/23746149.2018.1562982

A

Full spectra

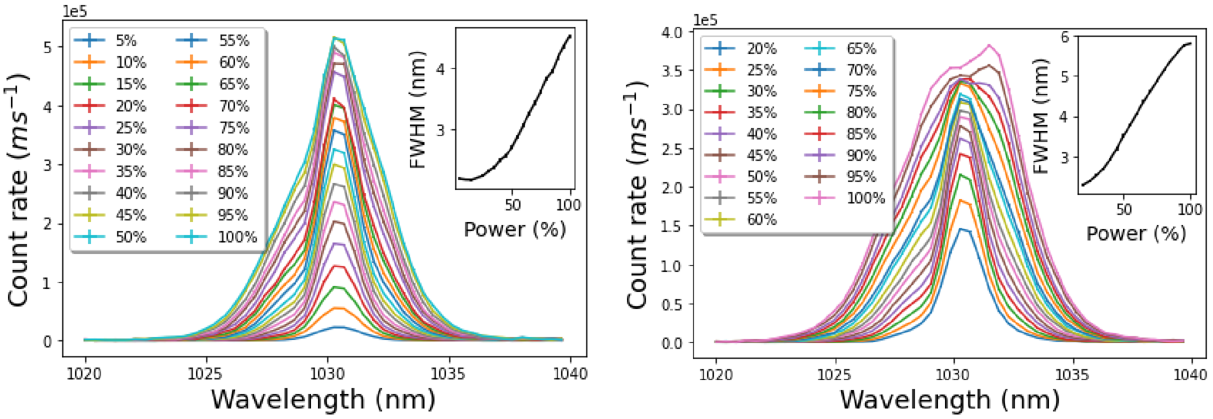

(a) Fused silica sample 47 cm away from the lens.

(b) Fused silica sample 45 cm away from the lens.

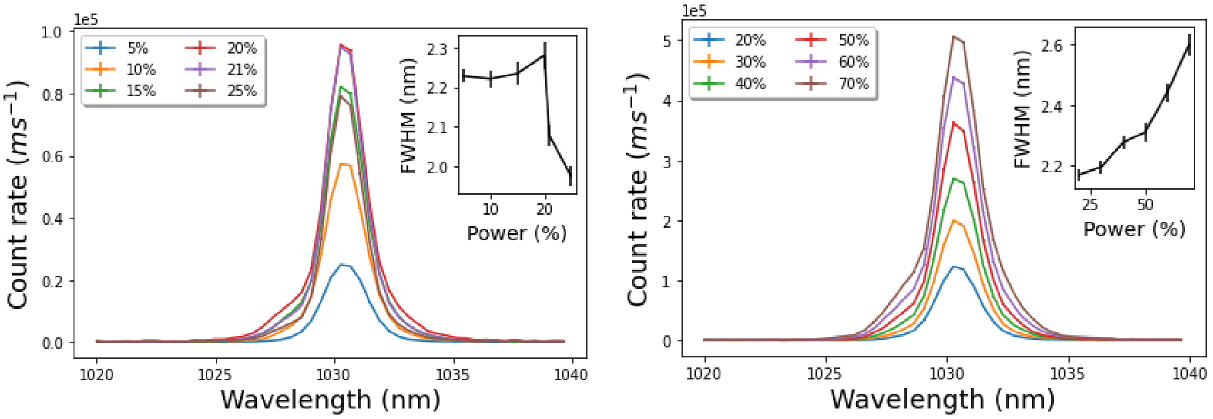

(c) Fused silica sample 43.5 cm away from the lens.

(d) CaF_2 sample.

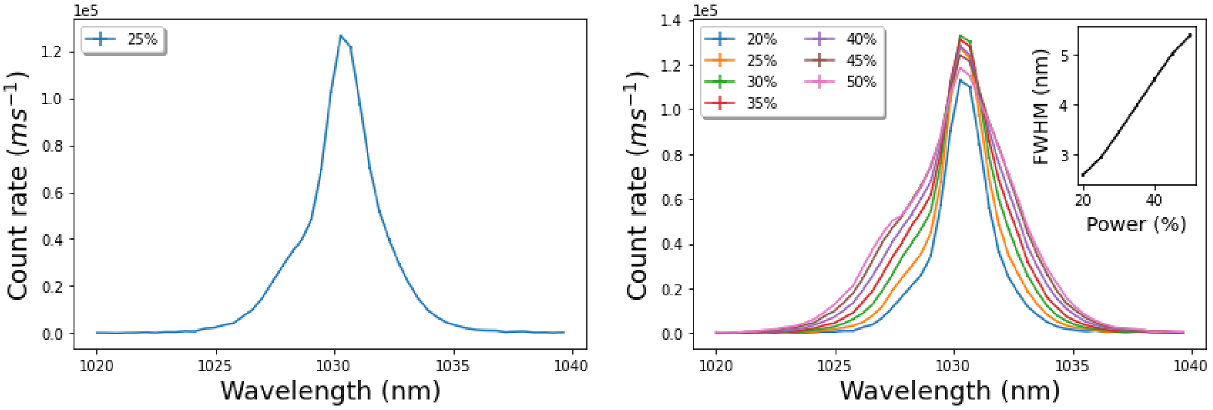

(e) Sapphire sample, FWHM= 3.2 nm.

(f) YAG sample.

Figure A.1: Spectral broadening at 1.03 μm. The captions are the percentage of the full power (82 W) sent to the sample. The insets depict the variation of FWHM with the power.

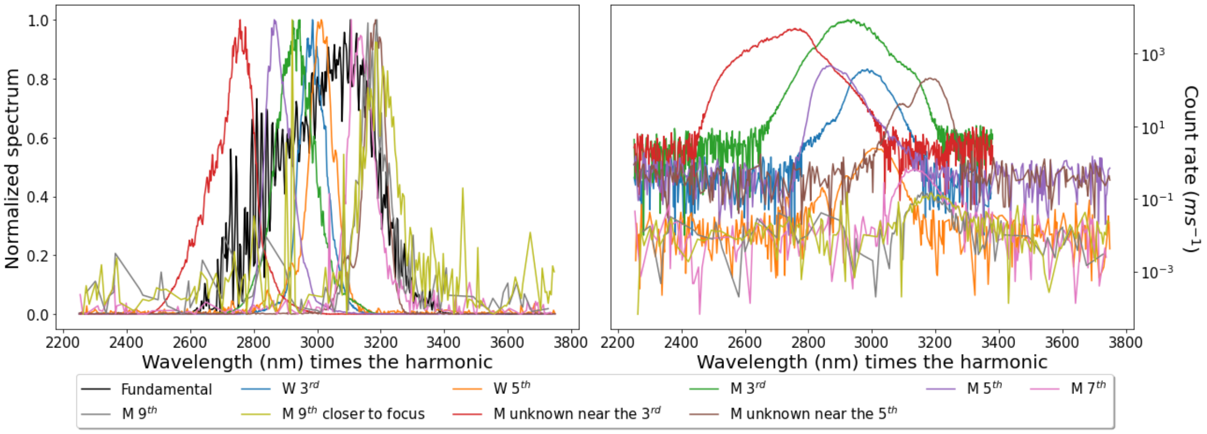

Figure A.2: Spectra of all harmonics obtained with a CaF_2 sample of 1 mm. Each spectrum corresponds to the angle with the highest count rate and are centered around the fundamental. On the left all spectra were normalized, while on the right we present the count rate of each spectrum.

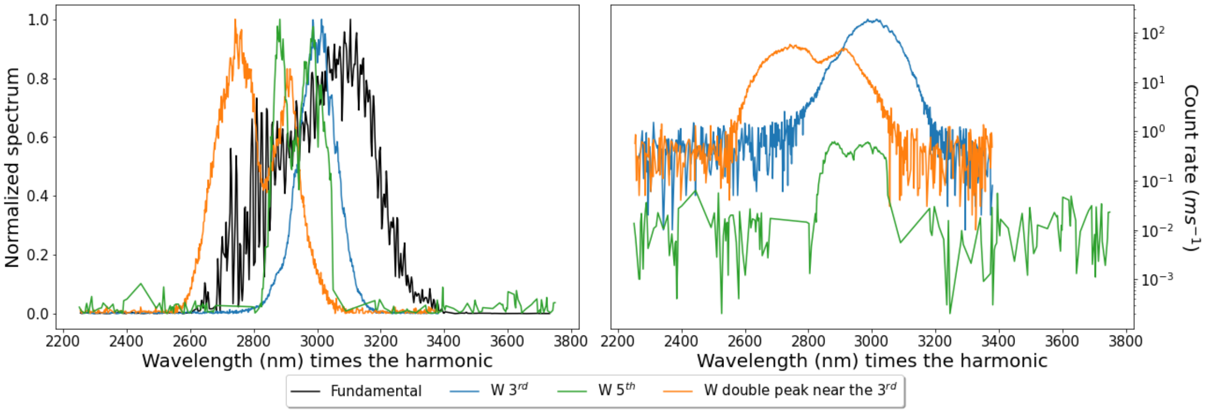

Figure A.3: Spectra of all harmonics obtained with a CaF_2 sample of 3 mm. Each spectrum corresponds to the angle with the highest count rate and are centered around the fundamental. On the left all spectra were normalized, while on the right we present the count rate of each spectrum.

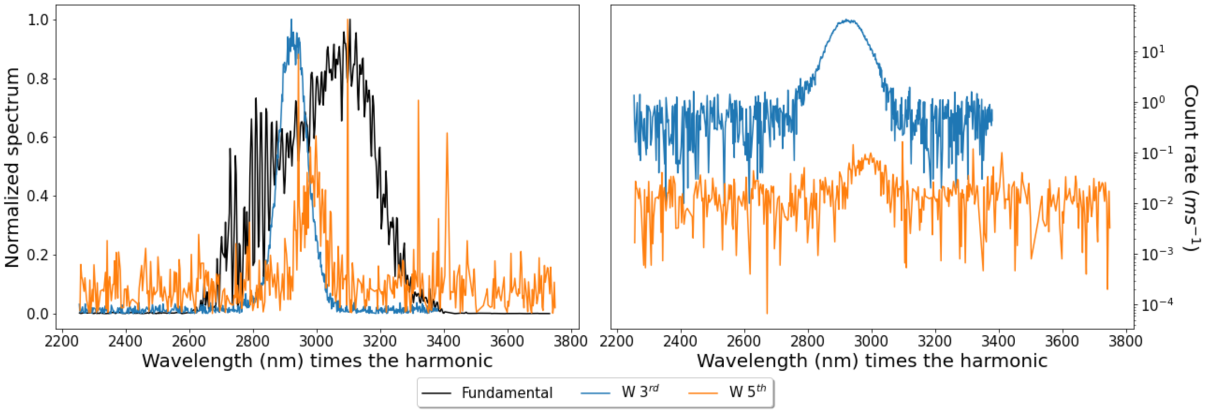

Figure A.4: Spectra of all harmonics obtained with a fused silica sample of 5 mm. Each spectrum corresponds to the angle with the highest count rate and are centered around the fundamental. On the left all spectra were normalized, while on the right we present the count rate of each spectrum.

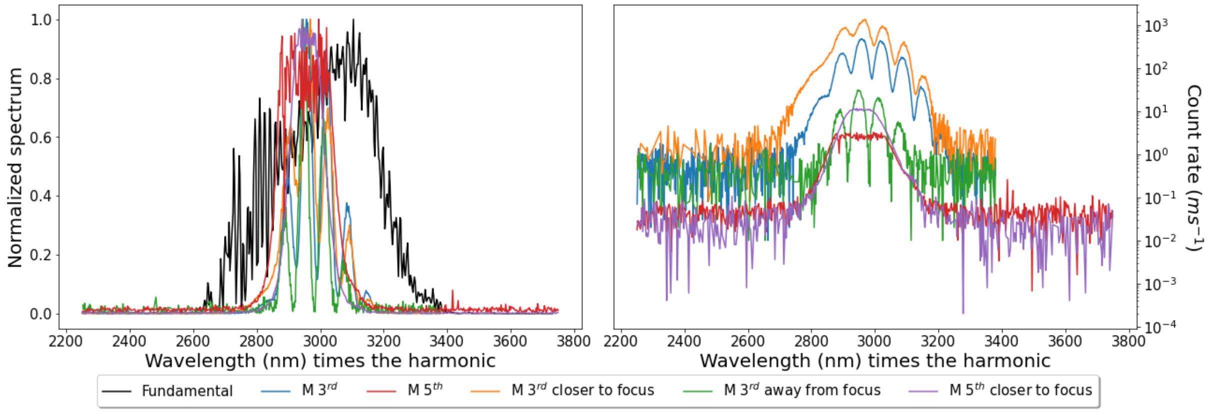

Figure A.5: Spectra of all harmonics obtained with a LiF sample of 3 mm. Each spectrum corresponds to the angle with the highest count rate and are centered around the fundamental. On the left all spectra were normalized, while on the right we present the count rate of each spectrum.

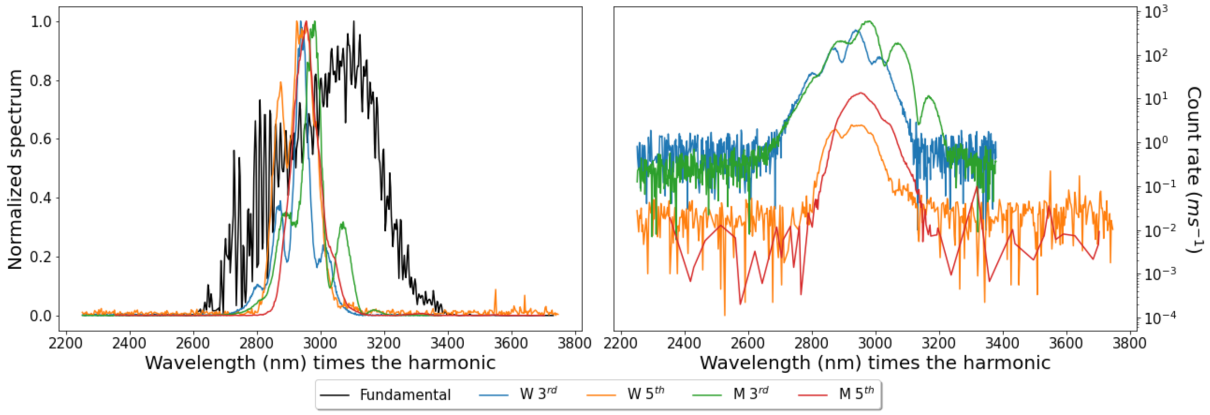

Figure A.6: Spectra of all harmonics obtained with a sapphire sample of 1 mm. Each spectrum corresponds to the angle with the highest count rate and are centered around the fundamental. On the left all spectra were normalized, while on the right we present the count rate of each spectrum.

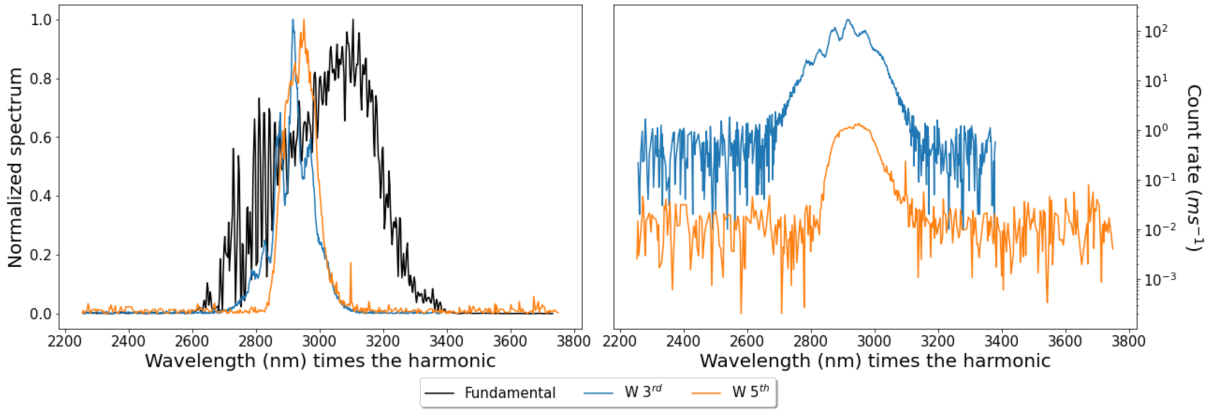

Figure A.7: Spectra of all harmonics obtained with a sapphire sample of 2 mm. Each spectrum corresponds to the angle with the highest count rate and are centered around the fundamental. On the left all spectra were normalized, while on the right we present the count rate of each spectrum.

B

Simulations and calculations with pyNLO

Listing B.1: Code for the calculation of GVD.

```python
import pynlo
import Crystals
import pylab
import matplotlib.pyplot as plt
import numpy as np
import scipy.constants as constants
speed_of_light=constants.c #Speed of light in vacuum (m/s)

def calculate_beta2(crystal,wl_nm): #Calculates the second order dispersion coefficient in ps^2/km
    return (--crystal.calculate_D_ps_nm_km(crystal(),wl_nm)*wl_nm**2/(2*np.pi
        *speed_of_light)*1e3)
    """ATTENTION: The double negative is just to call to attention that
    the pynlo lybrary calculates D but in a defenition with the opposite sign of most books/articles"""

crystal_list=[Crystals.CaF2,
Crystals.Fused_Silica,
Crystals.Sapphire,
Crystals.YAG]

Material={
    Crystals.CaF2:'Calcium Fluoride',
    Crystals.Fused_Silica:'Fused_Silica',
    Crystals.Sapphire:'Sapphire',
    Crystals.YAG:'YAG'
}


fig = plt.figure(figsize=(10,4))
ax  = fig.add_subplot(111)
ax.set_position([0,0,0.5,0.8])
pylab.xlabel('Wavelength (nm)', fontsize=15)
pylab.ylabel(r'$\beta_2\ (ps^2/km)$', fontsize=15)

for crystal in crystal_list:
    x=[]
    y=[]
    for wl in range(200,3500):
        x.append(wl)
        y.append(calculate_beta2(crystal,wl))
    plt.plot(x,y,label=Material[crystal])
ax.legend(loc='upper right', shadow=True,fontsize=10)
plt.hlines(y=0,xmin=200,xmax=3500,color='k')
plt.text(750,600,'Normal \ndispersion',fontsize=13,horizontalalignment='center')
plt.text(2500,-750,'Anomalous \ndispersion',fontsize=13,horizontalalignment='center')
plt.show()
```

Listing B.2: Code for the simulation with pyNLO.

```python
import numpy as np
import pynlo
import Crystals

def calculate_betas(crystal,wl_nm):
    '''Returns an array with the dispersion coefficients of second, third, and fourth-order, in units of [ ps^2/km , ps^3/km , ps^4/km ], for a given crystal
    (pynlo.media.crystals.CrystalContainer.Crystal class object) and wavelength in nm.
    '''
    return pynlo.media.fibers.calculators.DTabulationToBetas(lambda0=wl_nm, DData=np.array(
    [[l,-1e3*crystal.calculate_D_ps_nm_km(self=crystal(),wavelengths_nm=l)] for l in range(wl_nm-10,wl_nm+11,1)]
), polyOrder=2, DDataIsFile=False)
    """ATTENTION: The current version of the pynlo lybrary calculates the dispersion parameter (D) in a defenition with the opposite sign ence the minus sign.
    crystal.calculate_D_ps_nm_km: Calculates the D based on nefracive index given by the Sellmeir function in the crystal class object.
    pynlo.media.fibers.calculators.DTabulationToBetas: Read in a tabulation of D vs Wavelength. Returns betas in array [beta2, beta3,[U+FFFD], beta_polyOrder]
    """
#### Simulation
FWHM    = 1              # pulse duration (ps)
pulseWL = 1030           # pulse central wavelength (nm)
freq    = 100e3          # repetition rate of the pulses (Hz)
                         # does not affect the simulation itself it is just to calculate internally the average power in case of need
Full_EPP     = 82/freq # Energy per pulse at 100% (J)
Window  = 20   # simulation window (ps)
Steps   = 100     # simulation steps
Points  = 2**13  # simulation points
fibWL   = pulseWL # Center WL of fiber (nm)
```

```


beta2, beta3, beta4 = calculate_betas(Crystals.Sapphire,pulseWL) # (ps^2/km),(ps^3/km),(ps^4/km)
Length  = 15    # length in mm
EPP     = 0.25*Full_EPP #Energy per Pulse as a percentage of Full_EPP
Gamma   = 0.9E-03 # Gamma (1/(W km)
Raman   = True  # Enable Raman effect?
Steep   = True  # Enable self steepening?
alpha = 27.19443951 # attenuation coefficient in 1/m


# Create the pulse
pulse = pynlo.light.DerivedPulses.GaussianPulse(power = 1, # Power will be scaled by set_epp
                                            T0_ps                   = FWHM,
                                            center_wavelength_nm    = pulseWL,
                                            time_window_ps          = Window,
                                            NPTS            = Points,
                                            frep_MHz        = freq*1e-6,
                                            power_is_avg    = False)
# Set the pulse energy
pulse.set_epp(EPP)

# Create the fiber
fiber1 = pynlo.media.fibers.fiber.FiberInstance()
fiber1.generate_fiber(Length * 1e-3, center_wl_nm=fibWL, betas=(beta2, beta3, beta4),
                              gamma_W_m=Gamma * 1e-3, gvd_units='ps^n/km', gain=-alpha)

# Propagation
evol = pynlo.interactions.FourWaveMixing.SSFM.SSFM(local_error=0.005, USE_SIMPLE_RAMAN=True,
                 disable_Raman              = np.logical_not(Raman),
                 disable_self_steepening    = np.logical_not(Steep))

```

```python
z, AW, AT, pulse_out = evol.propagate(pulse_in=pulse, fiber=fiber1, n_steps=Steps)
# From: https://pynlo.readthedocs.io/en/latest/pynlo.html#pynlo-interactions-fourwavemixing
# z (array of float[U+FFFD]an array of positions along the fiber (in meters)
# AW (2D array of complex128[U+FFFD]A 2D numpy array corresponding to the intensities in each frequency bin for each step in the z-direction of the fiber.
# AT (2D array of complex128[U+FFFD]A 2D numpy array corresponding to the intensities in each time bin for each step in the z-direction of the fiber.
# pulse_out (PulseBase object[U+FFFD]the pulse after it has propagated through the fiber. This object is suitable for propagation through the next fiber!

#### Ploting the results
import matplotlib.pyplot as plt
import matplotlib as mpl

def dB(num): #Decibel convertion. ONLY FOR THE WAVEPACKET!!!
    return 10 * np.log10((np.abs(num)/np.max(np.abs(num)))**2)

fsize=14 #Font size of many of the labels
color_plot_threshold=20 # Threshold for the decibels in the color plot
FX_limit_low,FX_limit_high=[285,295] #Lower and upper bounds of the spectrum in the frequencies (THz)
FY_limit_low,FY_limit_high=[-20,2] #Lower and upper bounds of the spectral intensity (dB)

#Set the figure and subfigures
fig = plt.figure(figsize=(8,9))
ax0 = plt.subplot2grid((2,2), (0, 0), rowspan=1)
ax1 = plt.subplot2grid((2,2), (1, 0), rowspan=1, sharex=ax0)
ax2 = plt.subplot2grid((2,2), (0, 1), rowspan=3)

plt.subplots_adjust(wspace=0.3)

for i,axis in enumerate([ax0,ax1,ax2]):
    axis.tick_params(labelsize=12)

# Line plots

ax0.plot(pulse.F_THz,    dB(pulse.AW),  color = 'b', label="Input")
ax1.plot(pulse.F_THz,    np.abs(pulse.AW)/np.max(np.abs(pulse.AW)),  color = 'b', label="Input")

ax0.plot(pulse_out.F_THz,    dB(pulse_out.AW),  color = 'r', label="Output")
ax1.plot(pulse_out.F_THz,    np.abs(pulse_out.AW)/np.max(np.abs(pulse_out.AW)),  color = 'r', label="Output")

ax0.set_ylabel('Intensity (dB)', fontsize=fsize)
ax1.set_ylabel('Intensity (a.u.)', fontsize=fsize)

ax0.set_ylim(FY_limit_low,FY_limit_high)
ax0.set_xlim(FX_limit_low,FX_limit_high)
ax1.set_xlim(FX_limit_low,FX_limit_high)

ax1.set_xlabel('Frequency (THz)', fontsize=fsize)

#Color plots
F = pulse.F_THz     # Frequency grid of the pulse (THz)
zW = dB(np.transpose(AW)[:, (F > 0)] ) # Intensity grid for the color plot
extent = (np.min(F[F > 0]), np.max(F[F > 0]), 0, Length)
ax2.imshow(zW, extent=extent,
           vmin=np.max(zW) - color_plot_threshold, vmax=np.max(zW),
           aspect='auto', origin='lower', cmap="plasma")

ax2.set_ylabel('Propagation distance (mm)', fontsize=fsize, labelpad=5)
ax2.set_xlabel('Frequency (THz)', fontsize=fsize)
ax2.set_xlim(FX_limit_low,FX_limit_high)
plt.draw() #Python calculates the ticks of ax1 so they become callabel
ax2.set_xticks(ax1.get_xticks()[1:-1])
ax2.set_xticklabels(ax1.get_xticklabels()[1:-1])

#Color bar
norm = mpl.colors.Normalize(vmin=np.max(zW) - color_plot_threshold, vmax=np.
    max(zW)) #
cbar2=fig.colorbar(mpl.cm.ScalarMappable(norm=norm, cmap="plasma"), ax=ax2, label='Intensity (dB)')
cbar2.ax.tick_params(labelsize=12)
cbar2.set_label(label='Intensity (dB)',fontsize=fsize,rotation=-90)
cbar2.ax.get_yaxis().labelpad = 15

#Legend
handles,labels = ax0.get_legend_handles_labels()
legend0 = ax0.legend(handles,labels,loc='upper left')

plt.show()
```

Listing B.3: Contents of Crystals.py.

```
# -*- coding: utf-8 -*-
"""
Sellmeier coefficients and equations for multiple crystals
This file works with the pyNLO module.

    https://github.com/pyNLO/PyNLO
    https://pynlo.readthedocs.io/en/latest/index.html
"""
from __future__ import absolute_import
from __future__ import division
from __future__ import print_function

import numpy as np
from pynlo.media.crystals.CrystalContainer import Crystal

class Sapphire(Crystal):
    def __init__(self, **params):
        Crystal. __init__(self, params)

        """Sellmeir coefficients from:
        M. J. Dodge, "Refractive Index" in Handbook of Laser Science and Technology, Volume IV,
        Optical Materials: Part 2, CRC Press, Boca Raton, 1986, p. 30
        also depicted in https://refractiveindex.info/?shelf=3d&book=crystals&page=sapphire"""
        """C's measured in micron square"""
        self.B0   = 1
        self.B1   = 1.4313493
        self.C1   = 0.0726631**2
        self.B2   = 0.65054713
        self.C2   = 0.1193242**2
        self.B3   = 5.3414021
        self.C3   = 18.028251**2

    def n(self, wl_nm, axis = None):
        wl_um_s = (wl_nm * 1.0e-3)**2
        return np.sqrt(self.B0+
                       self.B1*wl_um_s/(wl_um_s-self.C1)+
                       self.B2*wl_um_s/(wl_um_s-self.C2)+
                       self.B3*wl_um_s/(wl_um_s-self.C3)
        )

class YAG(Crystal):
    def __init__(self, **params):
         Crystal. __init__(self, params)

        """Sellmeir coefficients from:
        D. E. Zelmon, D. L. Small and R. Page. Refractive-index measurements of undoped yttrium
        aluminum garnet from 0.4 to 5.[U+FFFD]mAppl. Opt. 37, 4933-4935 (1998)
        also depicted in https://refractiveindex.info/?shelf=main&book=Y3Al5O12&page=Zelmon"""
        """C's measured in micron square"""
        self.B0   = 1
        self.B1   = 2.28200
        self.C1   = 0.01185
        self.B2   = 3.27644
        self.C2   = 282.734

    def n(self, wl_nm, axis = None):
        wl_um_s = (wl_nm * 1.0e-3)**2
        return np.sqrt(self.B0+
                       self.B1*wl_um_s/(wl_um_s-self.C1)+
                       self.B2*wl_um_s/(wl_um_s-self.C2)
        )

class CaF2(Crystal):
    def __init__(self, **params):
         Crystal. __init__(self, params)

        """Sellmeir coefficients from:
        I. H. Malitson. A redetermination of some optical properties of calcium fluoride,
        Appl. Opt. 2, 1103-1107 (1963) also depicted in
        https://refractiveindex.info/?shelf=main&book=CaF2&page=Malitson"""
        """C's measured in micron square"""
        self.B0    = 1
        self.B1    = 0.5675888
        self.C1    = 0.050263605**2
        self.B2    = 0.4710914
        self.C2    = 0.1003909**2
        self.B3    = 3.8484723
        self.C3    = 34.649040**2

    def n(self, wl_nm, axis = None):
        wl_um_s = (wl_nm * 1.0e-3)**2
        return np.sqrt(self.B0+
                       self.B1*wl_um_s/(wl_um_s-self.C1)+
                       self.B2*wl_um_s/(wl_um_s-self.C2)+
                       self.B3*wl_um_s/(wl_um_s-self.C3)
        )

class Fused_Silica(Crystal):
    def __init__(self, **params):
         Crystal. __init__(self, params)

        """Sellmeir coefficients from:
         I. H. Malitson. Interspecimen comparison of the refractive index of fused silica,
```

```python
         J. Opt. Soc. Am. 55, 1205-1208 (19) also depicted in
        https://refractiveindex.info/?shelf=glass&book=fused_silica&page=Malitson"""
        """C's measured in micron square"""
        self.B0   = 1
        self.B1   = 0.6961663
        self.C1   = 0.0684043**2
        self.B2   = 0.4079426
        self.C2   = 0.1162414**2
        self.B3   = 0.8974794
        self.C3   = 9.896161**2

    def n(self, wl_nm, axis = None):
        wl_um_s = (wl_nm * 1.0e-3)**2
        return np.sqrt(self.B0+
                       self.B1*wl_um_s/(wl_um_s-self.C1)+
                       self.B2*wl_um_s/(wl_um_s-self.C2)+
                       self.B3*wl_um_s/(wl_um_s-self.C3)
        )
```